# The Hong Kong Polytechnic University
# Department of Applied Physics

# OPTICAL PROPERTIES AND MODULATED LUMINESCENCE OF METAL ION DOPED PHOSPHORS

**ZHANG Yang**

A thesis submitted in partial fulfillment of the requirements
for the degree of Doctor of Philosophy

**December 2011**

# CERTIFICATE OF ORIGINALITY

I hereby declare that this thesis is my own work and that, to the best of my knowledge and belief, it reproduces no material previously published or written, nor material that has been accepted for the award of any other degree or diploma, except where due acknowledgement has been made in the text.

____________________________________________ (Signed)

____________________ZHANG Yang______________ (Name of student)

# Abstract

Metal ions (including rare-earth and transition metal ions) doped phosphors have draw much attention due to their applications in light-emitting displays, lasers, optoelectronic devices and biomedicine. Among them, rare-earth doped upconversion phosphors are unique and attractive for fundamental research and great potential applications. The ability to manipulate the spectral properties of phosphors is highly desirable for understanding physical processes of energy transition and widespread applications. It is of considerable interest to find new approaches to rationally modulate the luminescence of phosphors.

To date, modification of luminescence in phosphors excited by a given excitation source can normally be achieved through a conventional chemical approach, i.e., changing the composition of host materials and/or doping ions, thus limiting our understanding of the detailed process of luminescence and applications. Until now, there are no reports of an established approach to modulate upconversion emission in an *in-situ* and real-time way. The unique crystal structure of ferroelectric materials provides us an opportunity to couple variables including electric field and temperature to crystal symmetry in a single compound. In this thesis, optical properties of rare-earth-doped ferroelectrics are investigated, and the influences of factors such as temperature and site substitution on the phosphors are observed. We also present a new approach to enhance and modulate upconversion emission through applying a relatively low bias voltage to the rare-earth-doped $BaTiO_3$ (BTO) thin films.

We investigated the luminescence properties of rare-earth-doped perovskite type hosts. Upconversion PL of $Er^{3+}$-doped BTO with perovskite $ABO_3$ structure was studies in terms of $Er^{3+}$ substitutions for Ba (A-) and Ti (B-site) with different $Er^{3+}$ doping concentrations. Photoluminescence (PL) quenching with an increasing $Er^{3+}$ doping concentration was investigated based on the structural change and energy transfer of cross-relaxation process in BTO: Er, i.e. $^2H_{11/2} + {}^4I_{15/2} \rightarrow {}^4I_{9/2} + {}^4I_{13/2}$. Temperature dependence of the PL in BTO: Er was revealed, which was associated with phase transitions of BTO host. The results imply that the emission from substituted $Er^{3+}$ ions may be used as structural probes for the ferroelectric titanates.

Significant tuning and enhancement of upconversion PL represent a great challenge. In contrast conventional chemical and plasmonic approaches, we firstly showed an enhancement and modulation of upconversion emission by applying low bias voltage to the rare-earth-doped BTO thin films on different substrates. The emission intensity at 523 nm of $ITO/BTO:Yb/Er/SrRuO_3/SrTiO_3$ heterostructure under the bias voltage at 10 V is almost 2.7 times as that of the unbiased one. Moreover, the PL intensity of the BTO:Yb/Er can be modulated with ac electric field. This work provides a real-time and dynamic way to control PL under an electric field.

The phenomena of electroluminescence (EL) have attracted an ever-increasing demand for applications throughout the illumination and display industries. In this thesis, we reported on the fabrication and characteristic of strain-induced piezoelectric potential stimulated luminescence from ZnS:Mn film on $Pb(Mg_{1/3}Nb_{2/3})O_3$-$x$$PbTiO_3$ (PMN-PT) substrate. The light emission of the ZnS:Mn arises from the piezoelectric potential, resulting from the converse piezoelectric effect of PMN-PT substrate. In contrast to conventional electroluminescence devices including LEDs, such novel light source can be controlled by high-frequency electric-field up to MHz. Moreover, a high-frequency ultrasonic transducer was also realized. The observed phenomena can be used to develop a dual-modal source combing light and ultrasonic signal.

In conclusion, we have utilized the unique characteristics of ferroelectrics and piezoelectrics to rationally modulate the light emission from metal ions-doped phosphors. These findings will aid further investigation of fundamental research and the widespread applications of the phosphors.

# List of Publications

1. **Y. Zhang**, J. H. Hao, C. L. Mak, and X. H. Wei, "Effects of site substitutions and concentration on upconversion luminescence of $Er^{3+}$-doped perovskite titanate", *Opt. Express* 9, 1824, 2011.
2. J. H. Hao, **Y. Zhang**, and X. H. Wei, "Electric-induced enhancement and modulation of upconversion photoluminescence in epitaxial $BaTiO_3$:Yb/Er thin films", *Angew. Chem. Int. Ed.* 50, 6876, 2011.
3. **Y. Zhang**, X. H. Wei, and J. H. Hao, "Enhanced photoluminescence of rare-earth doped perovskite titanate thin films grown on semiconductor wafer", *16th International conference on Luminescence (ICL'11) Ann Arbor, Michigan, USA*, July, 2011.
4. **Y. Zhang**, G. Y. Gao, H. L. W. Chan, J. Y. Dai, Y. Wang, and J. H. Hao, "Dual-mode light and ultrasound source from ZnS:Mn/PMN-PT thin-film structure controlled by electric-field", *Adv. Mater.* 24, 1729, 2012.
5. **Y. Zhang** and J. H. Hao, "Enhanced photoluminescence of rare-earth doped perovskite titanate thin films grown on semiconductor wafer", (to be submitted).

# Acknowledgments

I am, and will forever be indebted to my chief-supervisor, Dr. J. H. Hao for all his help and invaluable guidance throughout the period of my research. I thank him for his enthusiasm, advice, and effort, which have inspired me to achieve my doctorial study and make this thesis a reality.

I would like to thank my co-supervisor Dr. C. L. Mak for helpful guidance and discussions on my research and thesis. I wish to show my appreciation to Prof. H. L. W. Chan for her helpful suggestions on my research.

I would like to acknowledge the academic members in our department: Prof. S. P. Lau, Prof. S. F. Yu, Dr. J. Y. Dai, Dr. X. M. Zhang, Dr. F. Yan, and Dr. Albert Choy for their insightful suggestions during my research.

I would also like to thank Dr. X. H. Wei, Dr. G. Y. Gao. They gave me many helps during my study and research. I also have learned a lot from them. I also want to thank Mr. M. N. Yeung and Dr. W. Lu for their valuable advices and supporting to this thesis.

Many thanks also convey to my former and present colleagues in our department for their assistance and discussions in the research work. They include, Dr. Z. L. Wang, Dr. W. Huang, Mr. Z. P. Wu, Ms. L. H. Li, Mr. H. T. Wong, Mr. Z.

B. Yang, Mr. F. Tong, Ms. W. J. Jie, Dr. S. J. Zeng, Mr. G. W. Ding, Mr. J. H. Li, and Mr. P. Lin.

Finally, this thesis is dedicated to my family for their unwavering support and unconditional love throughout my life.

# Table of Contents

# List of Figures

# List of Tables

# Chapter 1 Introduction

Luminescent materials, also called phosphors, are mostly solid inorganic materials composed of a transparent host (or a matrix) and an activator, i.e. intentionally doped impurities [Yen, 2007]. The past several decades have witnessed rapid growth in research and development of phosphors. Phosphors have stimulated the fields of interests of physics, chemistry, electronics, nanoscience and biotechnology, with widespread applications involved in all aspects of human life (Figure 1.1). Studies on phosphors have covered almost all branches of luminescence, including photoluminescence (PL), electroluminescence (EL), cathodoluminescence (CL), and thermoluminescence (TL).

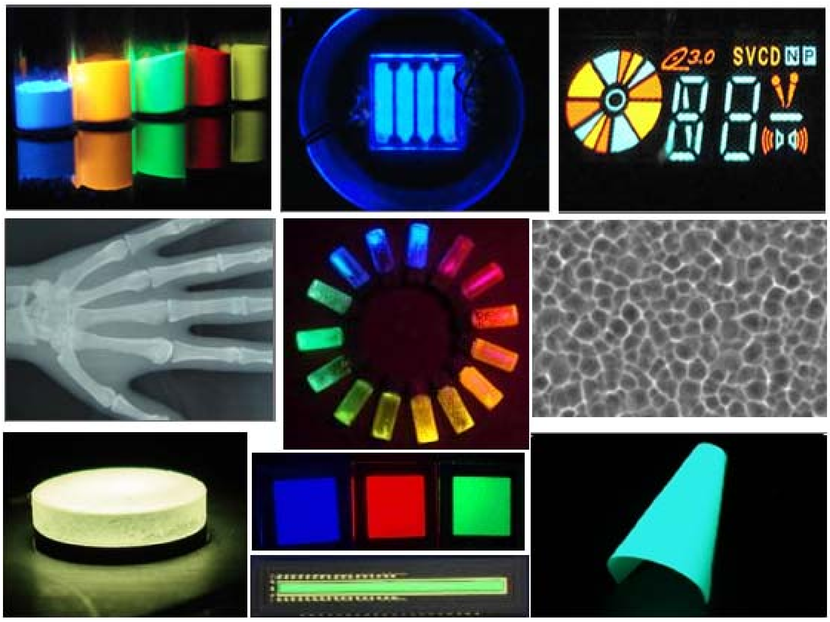

Figure 1.1. Widespread applications of phosphors.

The term “*luminescence*” was introduced into literature by Wiedemann [Wiedemann, 1888]. The word *luminescence* is defined as a phenomenon in which nonequilibrium radiation is excited by some kind of external energy and relaxes as light emission. Luminescence is emission of light over and above the thermal radiation background, thus a form of cold body radiation differed from incandescence. Luminescence can be classified into several types from the point of view of the excitation energy. Photoluminescence is excited by electromagnetic radiation, electroluminescence by electric field, cathodoluminescence by energetic electrons, mechanoluminescence by mechanical stimuli, and so on [Blasse, 1994]. This thesis mainly focuses on PL and EL based on rare-earth and transition metal ions doped phosphors. In most cases, the emission arises from the impurity ions, which are called activator ion. When the activator ions show weak absorption cross-section, other kinds of impurities are co-doped, which absorb the excitation energy and subsequently transfer the energy to the activators. The second dopant ions are defined as sensitizers. We have schematically drawn a phosphor in order to illustrate the definition as shown in Figure 1.2. The system consists of a host lattice, activators and sensitizers.

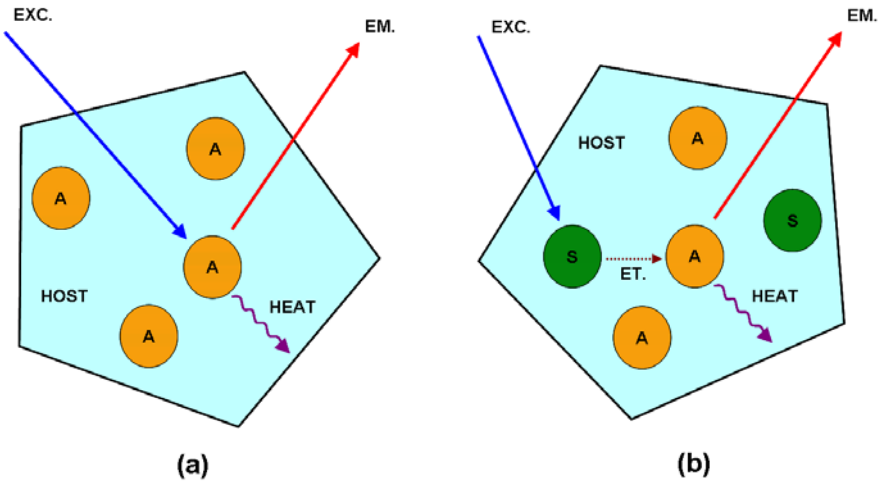

Figure 1.2. Schematic diagram of phosphors. (a) Activator in the host lattice. (b) Energy transfer from a sensitizer to an activator. A: activator; S: sensitizer; EXC: excitation; EM: emission; ET: energy transfer. [Blasse, 1994].

## 1.1 Photoluminescence (PL)

Photoluminescence (PL) is an important kind of luminescence. The most familiar PL process is fluorescence, in which the luminescent materials undergo some internal energy transitions before re-emitting the energy from the absorption event. So, the emitted fluorescence photons are typically of lower energy than those absorbed. This redshift in emission spectrum is called the Stokes shift. These PL process often are shown schematically in a diagram called a Jablonski diagram (Figure 1.3). The feature of PL depends on the intentionally incorporated impurities and the host materials. Various kinds of metallic impurities intentionally doped in crystals and semiconductor host materials as the activators. The impurities, also called dopant ions, are rare-earth or transition metal ions characterized by unfilled shells in the interior of the ion. Different electric configurations contribute to distinct optical properties of phosphors doped with rare-earth and transition metal ions.

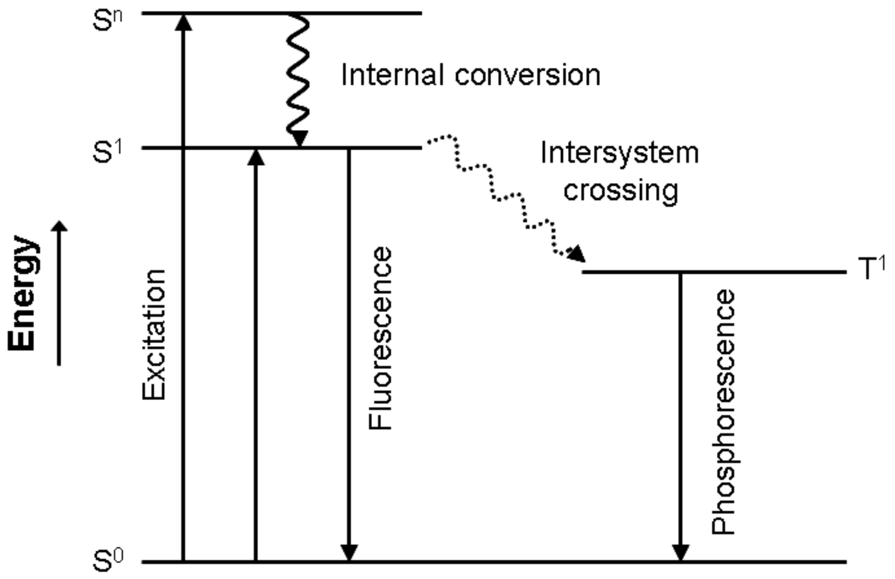

Figure 1.3. Jablonski diagram of a fluorescence event. Singlet states are labelled S and triplet states T; Superscripts 0, 1, n denote the ground state and excited states.

### 1.1.1 Basics of Lanthanide Ions

The lanthanide series comprise the 15 metallic chemical elements, from lanthanum through lutetium. The lanthanides plus scandium and yttrium are also known as the rare-earth elements. The unique luminescence properties of lanthanides have led to broad application and fascinated scientists for more than two centuries. Back to the late of 18th century, some renowned scientists such as Sir William Crookes, LeCoq de Boisbaudran, Eugène Demarçay or, later, Georges Urbain had utilized luminescence form lanthanides as an analytical tool to investigate the purity of the crystallizations and to identify potential new elements [Hänninen, 2011]. The term lanthanide was introduced by Victor Goldschmidt in 1925 [Hakala, 1952]. Scientist had pay attention to the forbidden spectral properties of lanthanides. It was confused that lanthanides exhibited sharp spectra lines which originated from intra-4f transitions. These transitions were known to be forbidden by the Laporte selection rule. In 1937 J. H. Van Vleck published an article titled “The Puzzle of Rare-Earth Spectra in Solids” [Vleck, 1937]. He confronted and analyzed this puzzle. It was in 1962, simultaneously and independently, Judd and Ofelt had proposed a general theoretical framework for calculating the intensities of transitions observed of rare-earth doped in solutions and solids [Judd, 1962; Ofelt, 1962]. The formulations proposed by Judd and Ofelt came to be known as the Judd-Ofelt theory. Where the applications of solid lanthanide based phosphors can be well cooperated with the progress of the opto-electronic industry.

### 1.1.2 Electronic Configuration of Lanthanide Ions

The lanthanide ions are characterized by an incompletely filled 4f shell and shielded from the surrounding by the filled $5s^2$ and $5p^6$ orbitals (Figure 1.4). Therefore, the host lattice has small influence on the optical transition within the $4f^n$ configuration (but essential). This feature is district from transition metal ions, whose 3d electrons located in an outer orbit, are heavily influenced by the environmental or crystal field.

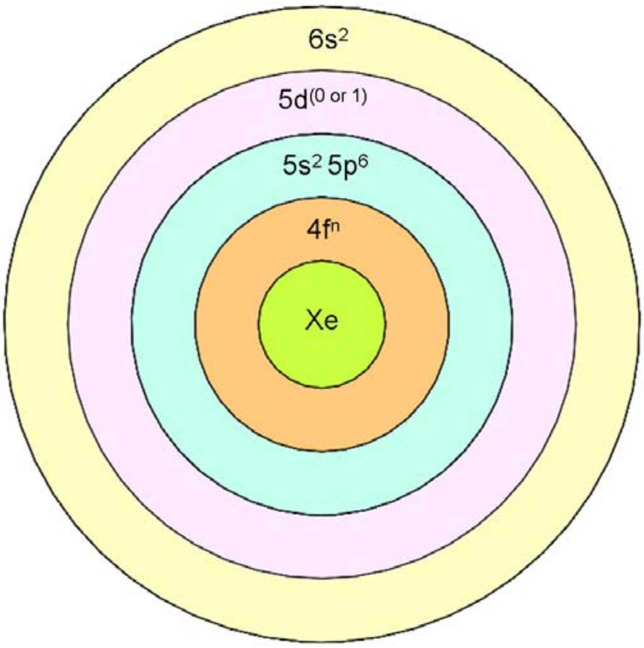

Figure 1.4. Rare-earth ion atomic structure. n: 2 to 14.

The electronic configurations of trivalent rare-earth ions in the ground states are shown in the Table 1.1. The lanthanide ions from $Ce^{3+}$ to $Lu^{3+}$ have one to fourteen 4f electrons located in their inner shell configuration. As shown in the Table 1.1, $Sc^{3+}$, $Y^{3+}$, $La^{3+}$ and $Lu^{3+}$ ions have no 4f electrons, so they have no electronic energy levels that can induce excitation and luminescence processes in or near the visible region. In contrast, the ions from $Ce^{3+}$ to $Yb^{3+}$, which have partially filled 4f orbitals, have electronic energy levels characteristic of each ion. These lanthanide ions have been extensively used as luminescent ions in phosphors and shown a variety of luminescence properties.

Table 1.1 Electronic configurations of rare-earth ions in the ground state [Cotton, 1988].

| Atomic Number | Symbol | Name | Electronic Configuration | |
|---|---|---|---|---|
| | | | Atom | $RE^{3+}$ |
| 21 | Sc | Scandium | $[Ar]3d^14s^2$ | [Ar] |
| 39 | Y | Yttrium | $[Kr]\ 4d^15s^2$ | [Kr] |
| 57 | La | Lanthanum | $[Xe]4f^05d^16s^2$ | [Xe] |
| 58 | Ce | Cerium | $[Xe]4f^15d^16s^2$ | $[Xe]4f^1$ |
| 59 | Pr | Praseodymium | $[Xe]4f^36s^2$ | $[Xe]4f^2$ |
| 60 | Nd | Neodymium | $[Xe]4f^46s^2$ | $[Xe]4f^3$ |
| 61 | Pm | Promethium | $[Xe]4f^56s^2$ | $[Xe]4f^4$ |
| 62 | Sm | Samarium | $[Xe]4f^66s^2$ | $[Xe]4f^5$ |
| 63 | Eu | Europium | $[Xe]4f^76s^2$ | $[Xe]4f^6$ |
| 64 | Gd | Gadolinium | $[Xe]4f^75d^16s^2$ | $[Xe]4f^7$ |
| 65 | Tb | Terbium | $[Xe]4f^96s^2$ | $[Xe]4f^8$ |
| 66 | Dy | Dysprosium | $[Xe]4f^{10}6s^2$ | $[Xe]4f^9$ |
| 67 | Ho | Holmium | $[Xe]4f^{11}6s^2$ | $[Xe]4f^{10}$ |
| 68 | Er | Erbium | $[Xe]4f^{12}6s^2$ | $[Xe]4f^{11}$ |
| 69 | Tm | Thulium | $[Xe]4f^{13}6s^2$ | $[Xe]4f^{12}$ |
| 70 | Yb | Ytterbium | $[Xe]4f^{14}6s^2$ | $[Xe]4f^{13}$ |
| 71 | Lu | Lutetium | $[Xe]4f^{14}5d^16s^2$ | $[Xe]4f^{14}$ |

Research on the absorption spectra of all lanthanide ions in lanthanum chloride was performed by the group of Dieke. The results were represented in an energy level diagram in which the energy levels for all lanthanides are given, and this energy level diagram is known as the “Dieke diagram”. The complete 4f energy level diagram is depicted in Figure 1.5.

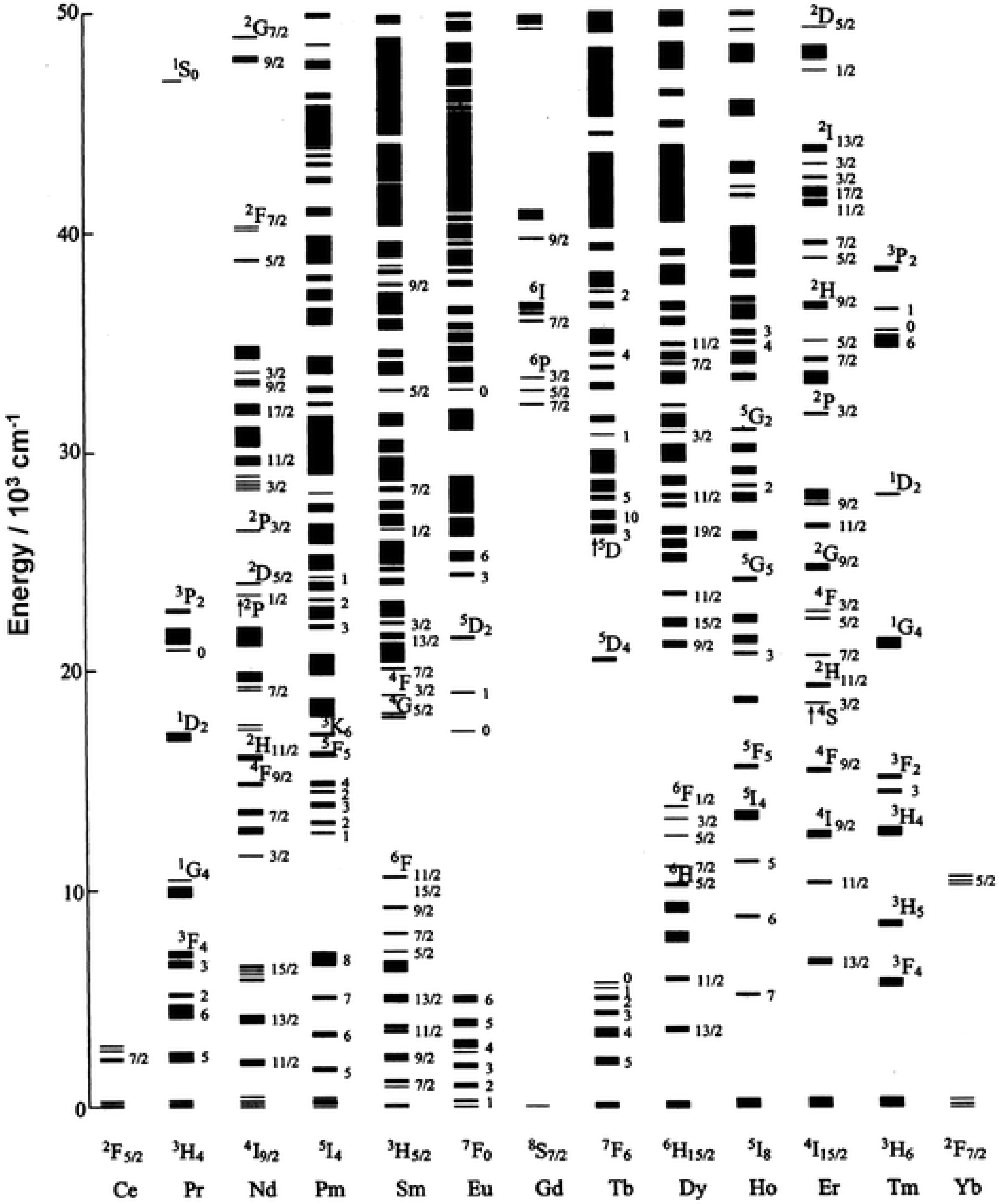

Figure 1.5. Energy levels of the 4f configurations of trivalent lanthanide ions [Carnall, 1989].

### 1.1.3 Upconversion

Upconversion refers to nonlinear optical processes characterized by sequential absorption of two or more photons leads to the emission of light at a shorter wavelength than the pump wavelength, i.e. anti-Stokes type emission [Haase, 2011]. Upconversion luminescence is different from multi-photon excitation. Multi-photon excitation requires femtosecond frequency excitation pulses with strong excitation intensity. In contrast to multi-photon excitation, upconversion can be efficiently excited even by continuous wave irradiation with low excitation densities. To date, almost all reports on upconversion phosphors are based on rare-earth and transition metal doped systems. The effect of upconversion was first discovered in 1959 [Bloembergen, 1959]. Since then, upconversion luminescence was studied intensively. The upconversion for the couple $Yb^{3+}/Er^{3+}$ in $CaWO_4$ was reported in 1966 by Auzel [Auzel, 1966]. It was suggested by Auzel that energy transfers between rare-earth ions could take place. Güdel et al. first reported the synthesis and characterization of upconversion nanoparticles in 2003 [Heer, 2003]. Nanoscale upconversion phosphors are of particular interest for bioimaging and medical applications [Zijlmans, 1999; Chatterjee, 2008; Wang, 2011]. Until now, upconversion phosphors have been proposed for various applications, such as display, light sources, solar cells, laser materials and biological labelling [Wang, 2010a; Zhang, 2011a; Trupke, 2002; Barnes, 2011; Lim, 2006]. Upconversion luminescence has been studied exclusively in rare-earth and transition metal doped phosphors. Upconversion processes can be divided into three classes: excited state absorption (ESA), energy transfer upconversion (ETU), and photon avalanche (PA). All three mechanisms are based on the sequential absorption of two or more photons by metastable, long lived energy states as shown in Figure 1.6.

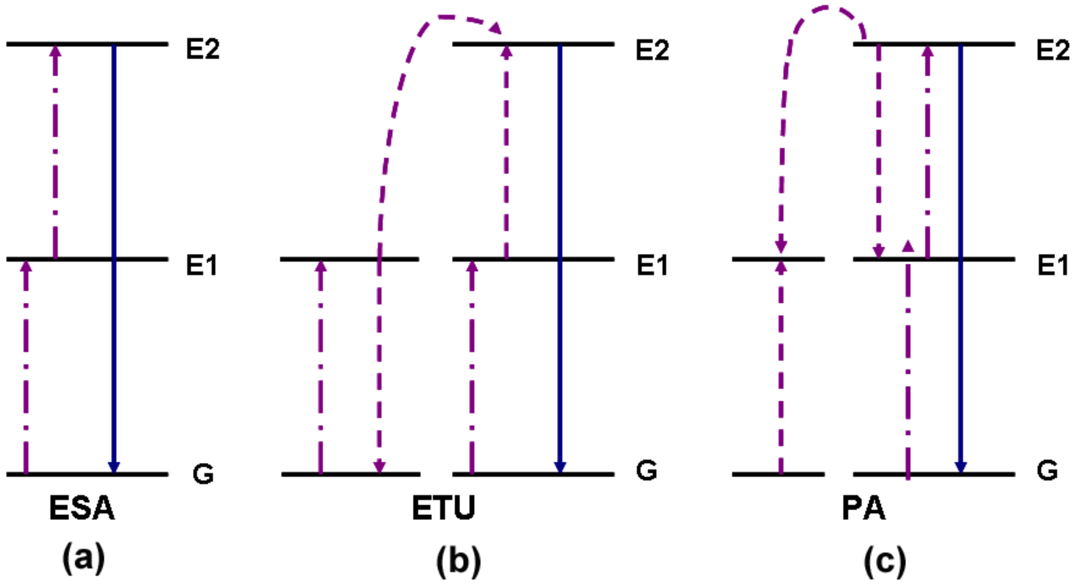

Figure 1.6. Upconversion processes for lanthanide doped phosphors: (a) excited state absorption (ESA), (b) energy transfer upconversion (ETU), (c) photon avalanche (PA). The dashed/dotted, dashed, and full arrows represent photon excitation, energy transfer, and emission processes, respectively [Wang, 2009].

In the case of ESA, if the excitation energy is resonant with the that from ground state G to excited metastable and long lived state E1, the emitting ions will sequentially absorb at least two photons of suitable energy to promote the ions to higher excited state E2 results in the E2 → G upconversion transitions (Figure 1.6a). In an ETU process, an emitting ion absorbs one pump photon and populates the metastable state E1, subsequent energy transfer from neighboring ions promotes the emitting ion to upper emitting state E2, while the other ion relaxes back to ground state G. The key difference between ETU and ESA is that ETU occurs between two neighboring ions, both in excited states, leading to upconversion emission. The photon avalanche effect draws great attention recently. Chivian et al. discovered high energy photon could give rise to upconversion above a given intensity threshold [Chivian, 1979]. PA process presents some unusual characteristics in that non-resonant GSA leads to strong upconversion emission shown in Figure 1.6c. The PA process starts with weak non-resonant GSA due to such reasons as phonon sideband or defect absorption, then populated to the metastable E1 level by nonradiative decay. Cross-relaxation energy transfer occurs between the excited ion and a neighboring ground state ion, resulting in both ions occupying the intermediate level E1. The PA effect is attributed to an enhanced population of the excited state resulting from the cross-relaxation process. The two ions readily populate E2 level to further initiate cross-relaxation, producing strong upconversion emission as an avalanche process.

### 1.1.4 Activators and Sensitizers

The upconversion luminescent phosphors, which can convert near-infrared to UV or visible emission via multiple absorption or energy transfer are of particular interest. Trivalent lanthanides ions, such as $Er^{3+}$, $Tm^{3+}$, $Ho^{3+}$, and $Pr^{3+}$ are most common activator ions for upconversion process due to their abundance of energy levels.

### $Er^{3+}$

The $Er^{3+}$ ion has drawn broad attention as the active ion for reasons, their characteristic emission at 1.55 $\mu$m, matches the attenuation minimum of silica optical fibers. While, these materials meet the requests for new upconversion phosphors, compact solid laser sources and photonics devices that pumped with CW near-infrared (NIR) diode lasers [Patra, 2003; Barnes, 2011; Auzel, 2004]. The efficiency of upconversion process for $Er^{3+}$ is particularly high. Such ladder-like arranged energy level structure of $Er^{3+}$ is depicted in Figure 1.7. The energy gap between the $^4I_{11/2}$ and $^4I_{15/2}$ states (~10350 $cm^{-1}$) and between the $^4I_{11/2}$ and $^4F_{7/2}$ states (~10370 $cm^{-1}$) is almost the same. Thus, under ~980 nm excitation, upconversion emission can occur in these levels of $Er^{3+}$. In addition, $Er^{3+}$ ion in the $^4I_{11/2}$ state can relax to the $^4I_{13/2}$ state, then can be excited to the $^4F_{9/2}$ state. The energy difference between $^4F_{9/2}$ and $^4I_{13/2}$ states is also in the same region, so this transition also can induced by ~980 nm excitation. As shown in Figure 1.7, the red and green fluorescent emission correspond to the intra-4f electronic transitions $^4F_{9/2} \rightarrow {}^4I_{15/2}$ and $^2H_{11/2}/^4S_{3/2} \rightarrow {}^4I_{15/2}$ of the $Er^{3+}$ ions, respectively. Radiative relaxation of $^4I_{13/2} \rightarrow {}^4I_{15/2}$ provides gain around 1.55 $\mu$m, the wavelength for telecommunications.

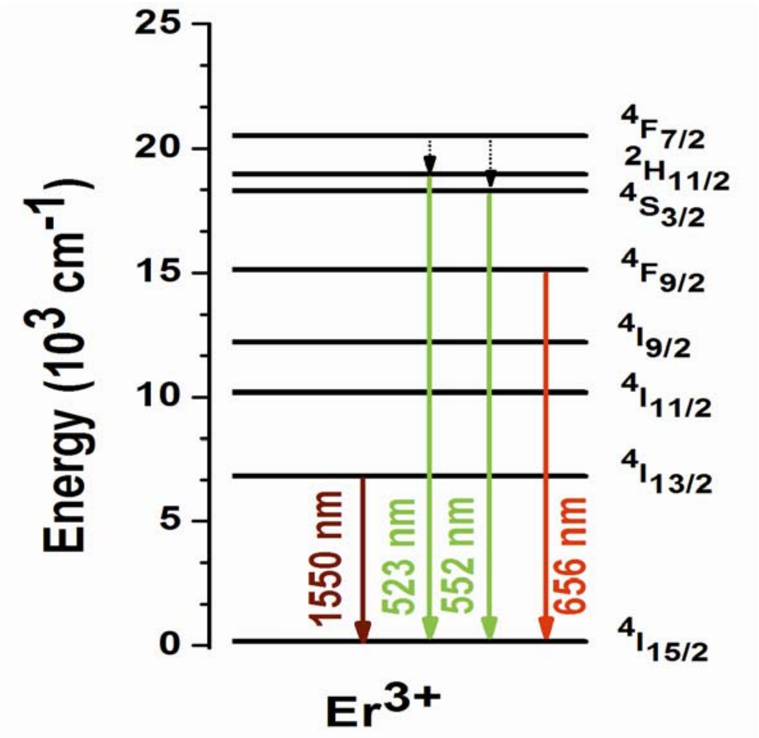

Figure 1.7. The energy level diagram of Er$^{3+}$.

**Tm$^{3+}$**

Trivalent Tm doped systems can emit violet (452 nm) or blue (476 nm) light. The ability that achieves so short wavelength emission is of significance for certain chemical and biological applications. The violet and blue luminescence of Tm$^{3+}$ contribute to the $^1D_2 \rightarrow {}^3F_4$ and $^1G_4 \rightarrow {}^3H_6$, respectively. The intensive violet and blue luminescence of Tm$^{3+}$ has been reported in infrared-to-visible upconversion phosphors sensitized by Yb$^{3+}$ such as NaYF$_4$:Yb/Tm [Zhang, 2011c]. Recently, white light sources have attracted intensive research interest for a variety of applications. The blue component of the upconversion luminescence from the Tm$^{3+}$ ion can be used to form single white light phosphors. Besides the blue luminescence, the emissions of $Tm^{3+}$ are also measured in the red region (640-710 nm), which can be assigned to the $^1G_4 \rightarrow {}^3F_4$, $^3F_2 \rightarrow {}^3H_6$, and $^3F_3 \rightarrow {}^3H_6$ transitions. In the near-infrared region, the emission around 807 nm due to the $^3H_4 \rightarrow {}^3H_6$ transition has been studied for in vivo imaging application [Wong, 2010]. The light absorption coefficient of biological tissues is minimum in near-infrared region (750-1000nm).

**$Eu^{3+}$**

A number of luminescent bands of $Eu^{3+}$ ions locate at 596, 616, 658 and 705 nm, which correspond to the $^5D_0 \rightarrow {}^7F_1$, $^5D_0 \rightarrow {}^7F_2$, $^5D_0 \rightarrow {}^7F_3$ and $^5D_0 \rightarrow {}^7F_4$ transitions. The emission around 596 nm is due to the magnetic dipole transition $^5D_0 \rightarrow {}^7F_1$, which is insensitive to the site symmetry. The emission in the vicinity of 616 nm is due to the electric dipole transition $^5D_0 \rightarrow {}^7F_2$, induced by the lack of inversion symmetry at the $Eu^{3+}$ site. So the luminescence from the $Eu^{3+}$ ion in different host symmetries shows different spectral characteristics. The luminescence intensity ratio of $^5D_0 \rightarrow {}^7F_2$ to $^5D_0 \rightarrow {}^7F_1$ is regards as a probe to detect the inversion symmetry around $Eu^{3+}$ in the host.

**$Yb^{3+}$**

In singly doped phosphors, since 4f-4f transitions are Laporte rule forbidden, inefficient absorption of the NIR excitation light contributes to low efficient upconversion process. To enhance upconversion luminescence efficiency of lanthanide dopes phosphors, a sensitizer with strongly absorption cross-section in the NIR region is usually co-doped along with the activator to ensure efficient energy transfer to the activator. In the case of upconversion phosphors based on $Er^{3+}$, trivalent Yb possesses an energy separation between the $^2F_{7/2}$ ground state and its $^2F_{5/2}$ excited state located around 980 nm. So $Yb^{3+}$ has a much larger absorption cross-section than that of other lanthanide ions. In addition, the $^2F_{7/2} \rightarrow {}^2F_{5/2}$ transition matches well with many 4f-4f transitions of upconversion lanthanide ions. Many reports on $Yb^{3+}/Er^{3+}$, $Yb^{3+}/Tm^{3+}$, and $Yb^{3+}/Ho^{3+}$ co-doped upconversion phosphors have published [Chatterjee, 2010].

### 1.1.5 Transition Metal Ions

Transition metals are a class of elements which exist in the d-block of the periodic table of elements. Transition metal ions have an incompletely filled d shell, whose electron configuration is $3d^n$ ($0 < n < 10$). These transition metals contain two or more electrons in their outer shell. The atomic structure of transition metal ions is shown in Figure 1.8. The 3d transition metal ions utilized in powder phosphors possess three electrons ($Cr^{3+}$ and $Mn^{4+}$) or five electrons ($Mn^{2+}$ and $Fe^{3+}$) occupying the outermost 3d electron orbitals [Yen, 2007]. The transition metals are characterized by an emission which consists of a broad band. Transition metals are strongly coupled to host lattice and susceptible to the host lattice ions. The position of the luminescence depends strongly on the host lattice. The emission can vary from green to deep red.

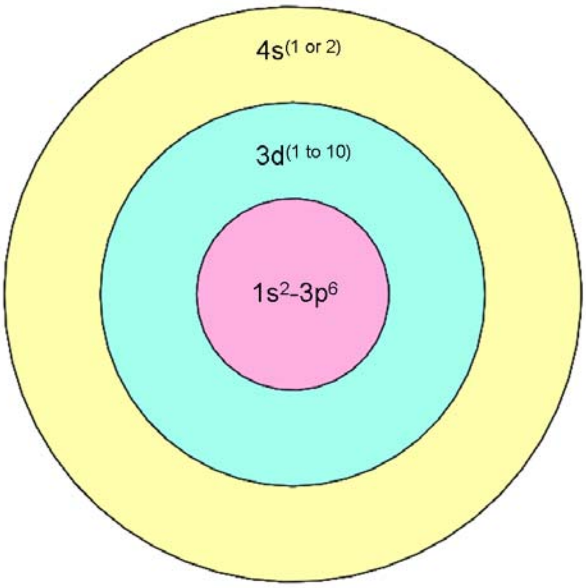

Figure 1.8. Transition metal ion atomic structure.

### $Cr^{3+}$

The luminescence of $Cr^{3+}$ in $Al_2O_3$ (ruby) was utilized for the first solid-state laser in 1960. The emission consists of two strong luminescence lines at 694.3 nm and 692.9 nm (the so-called $R_1$ and $R_2$ lines). These lines correspond to the transition from $^2E \rightarrow {}^4A_2$ transition. Spectroscopic properties of $Cr^{3+}$ ions depend strongly on the crystal field, which determines the sequence of the two lowest excited states, the $^2E$ doublet and $^4T_2$ quartet. Since $^4T_2$ level is sensitive to the crystal field, for relatively low crystal fields, the luminescence of $Cr^{3+}$ occurs from the spin-allowed $^4T_2 \rightarrow {}^4A_2$ transition and is characterized by a broadband with a short lifetime (~ 100 $\mu$s). An example is the emission spectrum of $Cr^{3+}$ doped $Mg_4Nb_2O_9$ [You, 1994].

In contrast, $^2E$ is insensitive to crystal field, in the high field case, the luminescence of $Cr^{3+}$ arises from the spin-forbidden $^2E \rightarrow {}^4A_2$ transition and is characterized by sharp lines and relatively long lifetime (~ms). So the strength of the crystal field on the $Cr^{3+}$ ion is of importance for its spectroscopic properties. Its emission can be varied from red in high crystal field strength into green in low crystal field strength.

### $Mn^{4+}$

The $Mn^{4+}$ ions ($3d^3$) in a crystalline host possess the same electronic structure of $Cr^{3+}$ ions. The $Mn^{4+}$ ions have been intensively studied as an activator or co-activator with rare-earth ions in many crystal hosts. The luminescence of $Mn^{4+}$ locates from 620 to 700 nm in most host materials. The crystal field at the higher charged $Mn^{4+}$ ion is stronger, so that the $Mn^{4+}$ emission always arises from the $^2E \rightarrow {}^4A_2$ transition. In $Al_2O_3$, the luminescence of $Mn^{4+}$ ions resembles that of $Cr^{3+}$, and is assigned to the $^2E \rightarrow {}^4A_2$ transition [Wu, 2008]. The spectroscopic studies of $Mn^{4+}$ ions in $YAlO_3$ performed by Noginov showed that three types of $Mn^{4+}$ centre with different decay times [Noginov, 1999]. $Mn^{4+}$-doped $CaAl_{12}O_{19}$ phosphors showed a main emission peak appeared at the 658 nm due to $^2E \rightarrow {}^4A_2$ transition of $Mn^{4+}$ ion [Pan, 2008; ]. These red phosphors are useful for LED applications.

**$Mn^{2+}$**

The $Mn^{2+}$ ion ($3d^5$) has a broad emission band, the position of which depends strongly on the host lattice. With the increase in the crystal field, the transition energy between $^4T_1$ and $^6A_1$ levels is predicted to decrease (shift to longer wavelength). The emission can vary from green to deep red. In a spinel structural host materials, $Mn^{2+}$ can occupy either tetrahedral or octahedral sites. Tetrahedrally coordinated $Mn^{2+}$ possesses a weak crystal field, typically resulting in a green emission. While, octahedrally coordinated $Mn^{2+}$ suffers stronger crystal field, usually exhibits an orange to red emission. An example is that the luminescence wavelength in $Zn_2SiO_4$:$Mn^{2+}$ is shorter than in $CaSiO_3$:$Mn^{2+}$ [Blasse, 1969]. This is attributed to a smaller coordination number in the former as compared with that in the latter. ZnS doped with $Mn^{2+}$ is one of the most successful phosphors used in PL and EL [Vlasenko, 1960; Lu, 2004]. This material emits a yellow-orange light located around 585 nm. The transition involved is also $^4T_1 \rightarrow {}^6A_1$ transition. ZnS:$Mn^{2+}$ based thin-film electroluminescence devices have shown great potential in flat panel display and lighting applications [Mito, 1974; Takeda, 1983].

Transition metal ions also can be used as activator in upconversion phosphors. Many lanthanide-transition metal systems were investigated by Güdel and co-workers [Güdel, 2001; Wermuth, 2001]. For instance, $Yb^{3+}$ ions are incorporated into $Mn^{2+}$ sites in $CsMnBr_3$ host. Near infrared absorption by $Yb^{3+}$ give broad band visible emission. The emission corresponds to the $^4T_1 \rightarrow {}^6A_1$ transition of $Mn^{2+}$

[Valiente, 2002]. In this thesis, transition metals are mainly used for electroluminescence and strain-induced luminescence except for upconversion phosphors, so here gives a brief introduction.

### 1.1.6 Host Materials

Selection of appropriate host materials plays a fundamental role in determining the optical properties such as upconversion efficiency and emission profile of the rare-earth doped phosphors. A rare-earth ion doped in a solid host can be considered as an impurity ion embedded in the host lattice. These dopant ions replace the host ions substitutionally. So the host lattice determines the distance between the dopant ions as well as their relative spatial position. Another influence of the host lattice on the optical properties of the dopant ions is the crystal field. The crystal field is essential in influencing the features of the spectral profile of a given ion. In addition, it also is responsible in the Stark effect regarding the splitting of energy levels of dopant ions in the host lattice.

The host materials typically have close lattice matches to dopant ions. The host lattices based on cations with ionic radii close to those of dopant ions can prevent the formation of crystal defects and lattice stress, and have been proven to be preferred host materials. Up to now, hexagonal phase $NaYF_4$ co-doped with $Yb^{3+}/Er^{3+}$ is known to be the most efficient host material for upconversion phosphors [Aebischer, 2006]. The host materials also generally require low phonon energies [Wang, 2009].

Typically, low phonon energies contribute to minimize nonradiative loss and maximize the radiative emission. The phonon energies of the host lattices and their interaction with the dopant ions have a strong influence on the upconversion process. As shown in Figure 1.9, under the excitation of 980 nm, through excited state absorption (ESA) and energy transfer upconversion (ETU) process, $Er^{3+}$ ion can populates the $^4F_{7/2}$ level from the $^4I_{11/2}$ level. Subsequently, the $Er^{3+}$ ion then relaxes nonradiatively to $^2H_{11/2}$ and $^4S_{3/2}$ levels by multiphonon relaxation, from which the green emission $^2H_{11/2}/^4S_{3/2} \rightarrow {}^4I_{15/2}$ occur. In addition, the nonradiative relaxation to the $^4I_{13/2}$ level from the above $^4I_{11/2}$ level can also be significant. Then, the strong red emission is observed by excited $Er^{3+}$ ion from $^4I_{13/2}$ level to the $^4S_{3/2}$ level. So to achieve efficient green emission, long lifetime of the excited $^4I_{11/2}$ level is required. Low phonon energies of the host materials benefit a long $^4I_{11/2}$ lifetime. Oxides exhibit high chemical stability with the phonon energy of about 500 $cm^{-1}$. In comparison, fluorides usually exhibit low energies (~350 $cm^{-1}$) and high chemical stability, and thus are often used as the host materials for upconversion.

It is well known that the variation of the crystal structure in the host materials can significantly influence the optical properties of dopant ions. For example, hexagonal phase $NaYF_4$:Yb/Er materials exhibit about an order of magnitude enhancement of upconversion efficiency relative to their cubic phase counterparts [Kramer, 2004]. The phase-dependent optical property can be ascribed directly to the different symmetries crystal fields around trivalent rare-earth ions. To date, modification of the upconversion photoluminescence in phosphors excited by a given excitation source can normally be achieved through a conventional chemical approach, i.e. changing the composition of host materials and/or doping ions. Low symmetry hosts typically exert a crystal-field containing more uneven components around the dopant ion compared to high symmetry counterparts [Wang, 2009]. The uneven components enhance the electronic coupling between 4f energy levels and higher electronic configuration and subsequently increase 4f transition probability of the dopant ions.

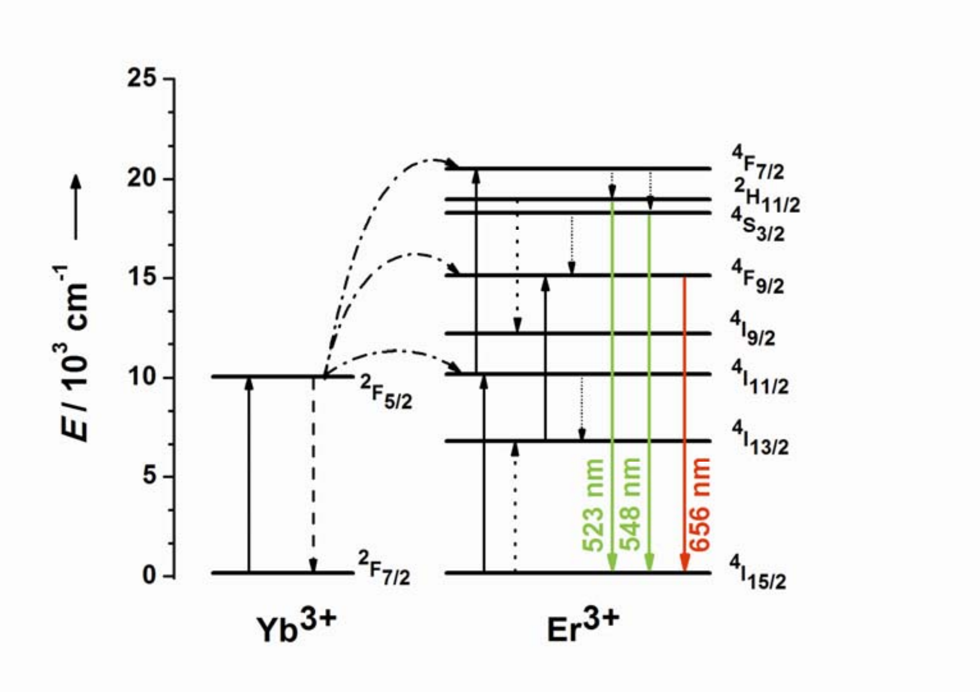

Figure 1.9. Energy level diagram of $Er^{3+}$ and $Yb^{3+}$ ions as well as the relevant upconversion process in $Yb^{3+}/Er^{3+}$ co-doped BTO under 980 nm laser excitation. The dashed-dotted, dashed, and dotted lines represent energy transfer, multiphonon relaxation, and cross-relaxation, respectively.

However, the tuning of PL by changing hosts is essentially an irreversible and *ex-situ* process. The unique crystal structure of ferroelectric materials provides us an opportunity to couple variables including electric-field and temperature to crystal symmetry in a single compound.

The family of ferroelectric properties, materials and devices has attracted considerable attention over several decades. Ferroelectric crystals are those polar crystals in which the direction of the spontaneous polarization can be switched by an external electric field. Most important ferroelectrics are oxides with a perovskite structure. The perovskite structure, named after the $CaTiO_3$, is a ternary compound of formula $ABO_3$, where A and B are two cations of different sizes. Typically, the A atoms are larger than the B atoms. In the ideal cubic unit cell, it is considered an FCC derivative structure in which A atom sits at the corner positions, B atoms sits at body centre positions and oxygen atoms sit at face centre positions. The unit cell of perovskite cubic structure can be viewed as consisting of $BO_6$ octahedra surrounded by A cations as shown in Figure 1.10.

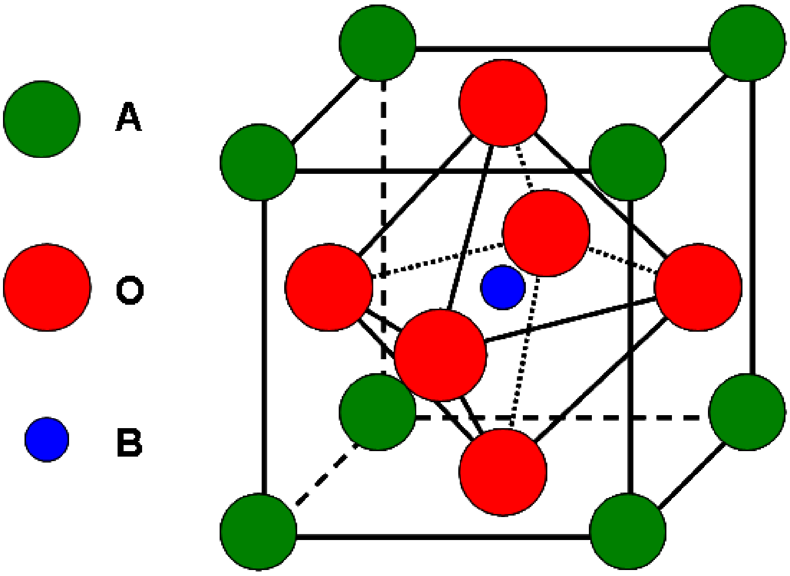

Figure 1.10. The perovskite structure $ABO_3$ which has a cubic structure.

$BaTiO_3$ (BTO) lattice can accommodate a large number of different dopants owe to the intrinsic capability of the perovskite structure to host ions of different size. It is found that these dopant ions can choose their site occupancy as a result of the local Ba/Ti ratio [Tsur, 2001]. By enhancing the Ba/Ti ratio, $Yb^{3+}$ and $Dy^{3+}$ are B-site dopants, and $Eu^{2+}$ and $Ce^{3+}$ are partially found on the A-site. While, $Y^{3+}$ and $Er^{3+}$ can occupy either A- or B-site. Among them, $Er^{3+}$ as an active ion has drawn broad attention. Since the size of the $Er^{3+}$ ion is almost intermediate between those of the $Ba^{2+}$ and $Ti^{4+}$ ion, $Er^{3+}$ ions exhibits amphoteric behaviour. The site substitutions of the dopant ions can strongly influence the electric properties of host materials [Buscaglia, 2000]. $Er^{3+}$ ions enter into the Ba site result in an extra electron as a compensating defect and a donor-type semiconducting material, while Ba-rich forces $Er^{3+}$ ions into the Ti site leading to the formation of an insulating BTO [Hwang, 2001]. Recently, the study of the luminescent properties of the rare-earth doped ferroelectric materials is strongly motivated because of their extensive applications in optoelectronic devices and displays. BTO has been an efficient host material due to its electronic, ferroelectric, and electro-optic properties [Jezowski, 2007; Joshi, 1997; Tenne, 2004]. Due to the 4f shell of rare-earth ions is well shielded by the outer electrons, the intra-4f transition is relatively independent of the host matrix. Nevertheless, the relative intensity of their photoluminescence is sensitive to their around environments.

## 1.2 Thin-film Electroluminescence (TFEL)

### 1.2.1 Background of EL

Electroluminescence (EL) is a luminescent material is excited by application of an electric voltage [Vij, 2004]. EL is the conversion of electrical energy into optical radiation. EL can be classified into two groups: high-field EL and low-field EL (injection EL). In injection EL, the applied voltage is characteristically a few volts, light-emitting diodes (LEDs) are typical of injection EL. The light radiation of LEDs generates from the direct injection and subsequent recombination of electro-hole pairs at a p-n junction. Injection EL devices are usually direct current driven, whereas high-field EL operates usually with alternating current. High-field EL is categorized into two types: powder phosphor EL and thin-film EL (TFEL). The high-field EL phenomenon was first discovered in the ZnS powder phosphor dispersed in castor oil [Destriau, 1936]. Until the transparent electrically conductive films made of $SnO_2$ were developed, AC powder EL devices were developed by Sylvania. Early power phosphor EL devices were direct driven and used mainly for lighting applications. However, these EL devices based on powder phosphors exhibited insufficient luminance and poor stability for practical use. TFEL was proposed by Vlasenko and Popkov in 1960 [Vlasenko, 1960]. They studied direct current driven TFEL in ZnS:Mn phosphors. Direct current driven TFEL devices feature a simple metal-insulator-metal (MIM) structure. Because of low efficiency and reliability related problems, direct current driven TFEL devices are not too common today. In 1974 Inoguchi reported that a alternating current driven TFEL (AC-TFEL) devices, consisting of a ZnS:Mn phosphor layer sandwiched by a pair of insulating layers, which had high brightness and excellent lifetimes [Inoguchi, 1974]. This type structure has become the center of research and development of EL since Inoguchi reported. AC-TFEL devices have become a commercialized technology for high resolution, good brightness and robust flat panel display. The structure of typical AC-TFEL device is shown in Figure 1.11. Double insulating layers can protect the phosphor layer against high electric field breakdown and moisture penetration to ensure high stability. The mechanism of EL in the thin film can be understood in the following way: electrons are injected from the interface between phosphor and insulating layers by field emission. The injected electrons are accelerated and gain high energy. High energy electrons excite the luminescent centres to the excited quantum states via impact ionization and/or impact excitation. The injected electrons travel through the phosphor layer and are finally re-trapped by the opposite interface between phosphor and insulating layers. The excited luminescent centres must eventually relax to ground state through optical radiation.

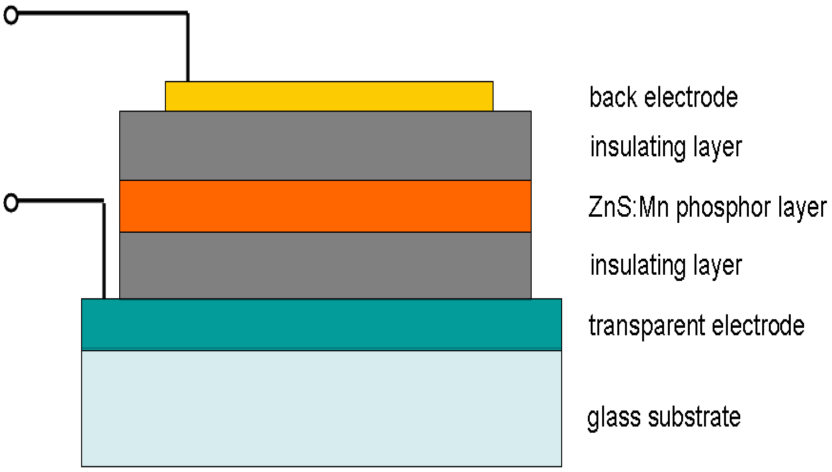

Figure 1.11. The schematic diagram of TFEL.

### 1.2.2 EL Phosphors

The great development from the 1970s has urged AC-driven TFEL (AC-TFEL) devices with high luminance and long lifetime commercially available, and AC-TFEL devices already occupy a segment of flat panel display market. AC-TFEL devices consist of a phosphor layer. In general, EL phosphors consist of a host material doped with an activator. The host materials typically have a large band gap so that the emission from the dopant can emit without absorption. II-VI compounds such as ZnS, ZnSe, SrS and Cas are extensive used as the host materials [Yen, 2007]. Among them, ZnS is the most widely used material. As to the dopant ions, transition metal ions (such as $Mn^{2+}$, $Cu^{2+}$) [Ihanus, 2005; Huang, 1997], and rare-earth ions (such as $Tb^{3+}$, $Tm^{3+}$, $Ce^{3+}$, $Eu^{2+}$) are found to be suitable as luminescent centers

[Streicher, 1995; Adachi, 2006; Shanker, 1984; Krupka, 1972]. $Mn^{2+}$ doped ZnS has proved to be the most successful EL phosphor. This phosphor emits a yellow-orange light with a peak around 586 nm. The emission corresponds to the $^4T_1 \rightarrow {}^6A_1$ transition of $Mn^{2+}$. Emission colors can be realized by incorporating different dopant ions in the phosphor. ZnS host doped with $Mn^{2+}$ has shown efficient yellow-orange color. Doped with $Tb^{3+}$ can give green and $Sm^{3+}$ red emission. The combination of Cu and Al produces a green emission, while Cu and Cl give blue and green emission bands, the relative intensity depends on the relative amount of Cu and Al [Blasse, 1994].

### 1.2.3 Insulating layers

The insulating layers play an important role in the AC-TFEL devices. The insulating layers need high breakdown electric field strength to protect the phosphor layer against electric breakdown. Nowadays, two types of dielectric insulating materials are mainly used in AC-TFEL devices. One is amorphous oxides, such as $Al_2O_3$, $SiO_2$, $TiO_2$ and so on [Basurto, 1975]. The other one is ferroelectric materials, such as $BaTiO_3$, $SrTiO_3$ and $PbTiO_3$ [Yen, 2007]. All of these insulating materials exhibit high dielectric constant to ensure the stability of devices.

# 1.3 Literature Review

## 1.3.1 Metal Ion-doped Phosphors

Rare-earth-doped phosphors are extensively being studied due to their potential applications in electro-optical devices and flat panel displays. Rare-earth ions exhibit a characteristic intra-4f shell luminescence, while the luminescence features and relative intensity of the spectra depend on the crystal symmetry of the host materials. Recently, increasing interests have been focused on luminescent properties of perovskite-type oxides activated by rare-earth ions. Perovskite-type oxides exhibit greater chemical stability than sulphide, thus being suitable as phosphor hosts. $ABO_3$-type perovskite compounds such as $BaTiO_3$ (BTO), $CaTiO_3$ (CTO) and $SrTiO_3$ (STO) have drawn great attention because of their attractive dielectric constant, ferroelectric activity and electro-optic properties. Thus a great deal of perovskite-type phosphors, such as BTO and STO activated by rare-earth ions, including $Er^{3+}$, $Pr^{3+}$, $Eu^{3+}$ and so forth have been investigated extensively [Zhang, 2000; Wang, 2005a; Weber, 1965;].

In the past, ferroelectrics doped with rare-earth ions have been extensive investigated in ferroelectricity, phase transitions and luminescence. The luminescent properties of rare-earth-doped perovskite-type oxides did not attract much attention due to the low luminescence efficiency. Until 1994, CTO: $Pr^{3+}$ was found as a potential red phosphor for display applications [Vecht, 1994]. Later in 1996, Toki et al. reported STO: $Pr^{3+}$ as a new red phosphor for field-emission displays [Toki, 1996]. BTO is ferroelectric and has different host symmetry from that of STO and CTO, promising to launch many investigations on the luminescent properties of $Pr^{3+}$-doped BTO phosphors. Pengzhan Zhang et al. found that the PL spectra of $Pr^{3+}$-doped BST were sensitive to both polarization and phase transition of the ferroelectric ceramics [Zhang, 2008]. Both polarization and phase transition effects on the PL of $Pr^{3+}$ ions were ascribed to local environmental changes. The $Eu^{3+}$ ion is a highly luminescent species, and it can be detected even at very low concentrations. The luminescent properties of $Eu^{3+}$ ions were found to be associated with the crystallinity of the hosts. The luminescence from $Eu^{3+}$ ions in different host crystals reveals different spectral characteristics, which can be contributed to the different site symmetries of the $Eu^{3+}$ ions in the various host materials [Chen, 1992]. Mingrong Shen et al. reported that the luminescent, dielectric and magnetic properties of $Eu^{3+}$-doped STO strongly depended on the substituting positions of Eu ion [Jiang, 2009].

Among all rare-earth ion, $Er^{3+}$ ion as an active ion has been studied intensively. Cheng-Hung Wen et al. used the PL spectroscopy of $Er^{3+}$-doped potassium niobate ($KNbO_3$) to study the phase transition of $KNbO_3$ [Wen, 2005a]. BTO is a potential thin film integrated optic host because of its electro-optic properties. Green upconversion emission had been obtained from BTO: $Er^{3+}$ film under 980 nm laser excitation [Zhang, 2000]. The sensitization of rare-earth ions co-doped with $Yb^{3+}$ ions is a well-known method for increasing the luminescent efficiency because of the high absorption cross-section of $Yb^{3+}$ ions around 980 nm and the efficient energy transfer from $Yb^{3+}$ to other rare-earth ions [Gao, 2009].

Transition metals with the unfilled 3d shell are not well screened due to only a single outer shell. So transition metal ions are strongly coupled to the host lattices. The optical spectroscopy of transition metals is characterized by broad, undefined features. Some sharp lines are also observed. The two strong $R_1$ and $R_2$ lines of ruby ($Al_2O_3:Cr^{3+}$) are related with the crystal field [Bartolo, 2006]. $Mn^{2+}$-doped ZnS is also a famous PL and EL phosphor due to its high efficient yellow emission of $Mn^{2+}$. $Zn_2SiO_4$ is a good host material for both rare-earth and transition metal ions, $Zn_2SiO_4$ doped with divalent transition metal ions ($Mn^{2+}$, $Co^{2+}$ and $Ni^{2+}$) provides excellent luminescence in visible spectrum [Kotera, 1985; Ouyang, 1996]. Octahedral $Ni^{2+}$ in appropriate crystal has been observed to emit ultra-broadband infrared luminescence. Recently, Shifeng Zhou et al. reported that $Ni^{2+}$-doped $ZnO$-$Al_2O_3$-$SiO_2$ composite glasses which presented near-infrared activity [Zhou, 2011].

### 1.3.2 Tunable PL

The ability to manipulate the PL of phosphors is of significance for their applications as lighting emitting displays, lasers, and electro-optic devices. To date, modification of the PL in phosphors excited by a given excitation source can usually be achieved through a conventional chemical approach, i.e. changing the composition of host materials and/or doping ions. Xiaogang Liu et al. presented a general and versatile approach to fine-tuning the upconversion emission, by doping the same $NaYF_4$ host doped with $Yb^{3+}$, $Er^{3+}$, and $Tm^{3+}$, and adjusting their concentrations as shown in Figure 1.12. This approach also can be extended to other host-activator combinations.

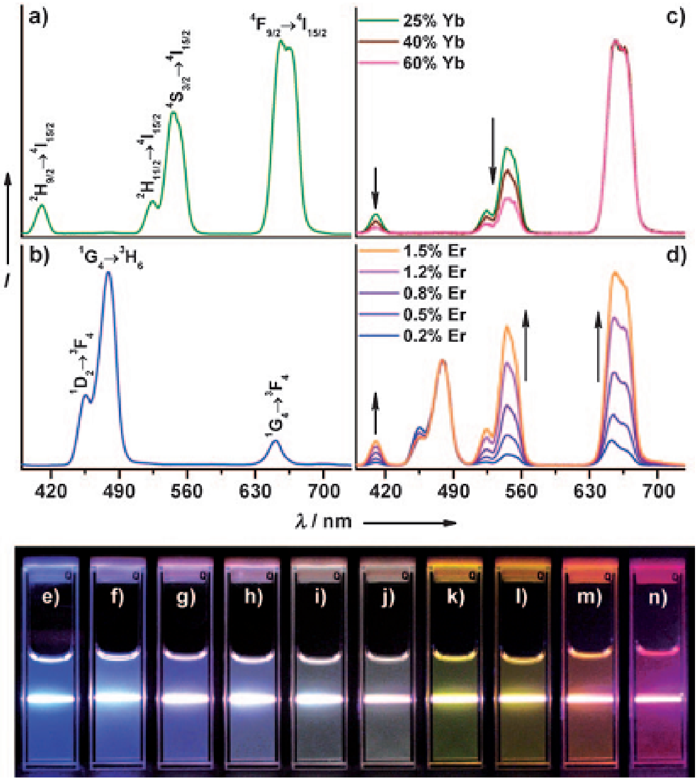

Figure 1.12. Room-temperature upconversion emission spectra of (a) $NaYF_4$:$Yb^{3+}$, $Er^{3+}$ (18 and 2 mol%), (b) $NaYF_4$:$Yb^{3+}$, $Tm^{3+}$ (20 and 0.2 mol%), (c) $NaYF_4$:$Yb^{3+}$, $Er^{3+}$ (25-60 and 2 mol%), and (d) $NaYF_4$:$Yb^{3+}$, $Tm^{3+}$, $Er^{3+}$ (20, 0.2, and 0.2-1.5 mol%) particles in ethanol. Complied luminescent photos showing corresponding colloidal solutions of (e) $NaYF_4$:$Yb^{3+}$, $Tm^{3+}$ (20 and 0.2mol%), (f-j) $NaYF_4$:$Yb^{3+}$, $Tm^{3+}$, $Er^{3+}$ (20, 0.2, and 0.2-1.5 mol%), (k-n) $NaYF_4$:$Yb^{3+}$, $Tm^{3+}$, $Er^{3+}$ (18-60 and 2 mol%). These samples were excited at 980 nm with a 600 mW diode laser [Wang, 2008a].

Besides the color-tunable phosphors, sources of white light have attracted intensive interest for various applications. As the infrared laser excitation source has been commercial available, rare-earth-doped upconversion white light phosphors have been successfully prepared. Jun Lin et al. has synthesized $BaYF_5:Yb^{3+}$, $Er^{3+}$, $Tm^{3+}$ via a hydrothermal process [Zhang, 2011a]. Under the excitation of a 980 nm single-wavelength diode laser, their phosphors can produce different colors, including blue, green, red, and white, by controlling the doping concentration of rare-earth ions.

Recently, upconversion PL has shown a great potential applications ranging from optical imaging, display and biomedicine. Enhancement and modulation of upconversion PL still represents a significant challenge. Plasmon-enhanced upconversion PL was recently presented. Stefan Schietinger et al. have performed enhanced upconversion PL by controlled nanoassembly of $NaYF_4:Yb^{3+}$, $Er^{3+}$ nanoparticles with gold nanospheres [Schietinger, 2010]. Later, Hua Zhang et al. reported the distinct modulation of upconversion emission through plasmonic interaction between the $NaYF_4:Yb^{3+}$, $Tm^{3+}$ nanocrystals and gold nanostructures [Zhang, 2010].

Besides the methods mentioned above, there are also several approaches for tuning upconversion PL, such as surface modification [Yi, 2007], nanocrystal size controlling [Mai, 2007], and utilizing multicolour-encoded microbeads [Wang, 2006a].

### 1.3.3 Thin-film Electroluminescence (TFEL)

Luminescence controlled by electric-field is related to electroluminescence (EL). EL can be classified into two groups: high-field EL and injection EL. The high-filed EL phenomenon was discovered from ZnS phosphor powder by Destriau in 1936 [Destriau, 1936]. EL in thin film was described in 1960s [Vlasenko, 1960]. Russ and Kennedy firstly proposed the sandwiched structure thin-film EL (TFEL) device [Russ, 1967]. In 1974, Inoguchi reported that a triple-layered TFEL devices, which was considered as a tuning point in the studies on EL. The AC-driven TFEL (AC-TFEL) devices consisted on ZnS:Mn phosphor layer sandwiched by a pair of insulating layers, showed high luminance and a reasonable lifetime for the flat panels [Inoguchi, 1974]. Since then, the AC-TFEL panels with triple-layered structure have occupied a segment of flat panel display market. New phosphor materials for red, green and other colors were investigated in order to get full-colour displays. For example, ZnS:Tb exhibits green, and ZnS:Sm shows red EL [Blasse, 1994]. And many other proposals can be found in the literature.

When researchers advanced high-field EL, in the 1960s, a carrier injection-recombination type light-emitting diode was realized using a GaAs single-crystal p-n junction. The first red emitting LED was made from GaAsP alloy by N. Holonyak [Holonyak, 1962]. However, the emission efficiency was very low. With continuous research on new phosphors and architectures, the performance of LED has achieved a series of great advances. A new form of red-emitting light LED with high efficiency based on AllnGaP/Gap was reported [Humphreys, 1990]. In 1993, the first blue color LED was made by Nakamura [Nakamura, 1994]. In 1996, Nakamura et al. produced the first white LED. Recent years, organic light emitting diodes (OLEDs) have attracted more and more interest [Shinar, 2004]. OLEDs provide a promising route towards low cost, flexible, and efficient devices. Now, OLEDs have realized commercial applications. Herein, we don't make much discussion.

## 1.4 Objective and Scope of This Thesis

The main objectives of the present research are summarized as follows: The first one is to investigate the influences of factors such as doping concentration, site substitution and temperature on the optical properties of rare-earth-doped ferroelectrics. The second one is to explore a new approach to enhance and modulate upconversion emission of rare-earth-doped phosphors. The last one is try to find out electric-field-controllable light-emission system beyond traditional working principles.

The thesis consists of seven chapters. Introduction in Chapter 1 gives an overview of rare-earth and transition metal ions doped phosphors.

Chapter 2 provides the basic theory pertinent to this thesis including the relevant physics of the rare-earth ions and ferroelectric properties of ferroelectric thin films and ceramics.

Chapter 3 describes the sample fabrication techniques and characterization methods used in the thesis.

In Chapter 4, BTO doped with different rare-earth ions substituting positions and concentrations were prepared by solid-state reaction method. Effects of site substitutions and concentration on upconversion PL of $Er^{3+}$-doped BTO were studied. Co-doping ($Yb^{3+}$, $Tm^{3+}$, $Er^{3+}$) BTO phosphors with different doping concentrations were prepared and studied. The PL properties of $Eu^{3+}$-doped BTO phosphor has also been investigated,

Chapter 5 presents an enhancement and modulation of upconversion emission by applying low bias voltage to the rare-earth-doped BTO thin films.

In Chapter 6, strain-mediated light emission from ZnS:Mn thin-film grown on piezoelectric PMN-PT substrate is demonstrated.

Chapter 7 gives the conclusion and suggestions for future work.

## 1.5 Statement of Original Contributions

To the best of our knowledge, the present work has made the following original contributions:

1. The influence of site substitution of $Er^{3+}$-doped BTO on its PL properties was demonstrated. In order to understand the relationship between phase transition and luminescent behavior, the PL spectra of $Er^{3+}$-doped BTO as a function of temperature were investigated.

2. We have demonstrated that the enhancement and modulation of upconversion PL can be realized by applying relatively low voltage to Yb/Er co-doped BTO thin film in an *in situ* and real-time manner. The approach is in contrast to conventional chemical routes.

3. We propose a novel materials system of ZnS:Mn film grown on piezoelectric PMN-PT substrate and firstly demonstrate electric-field-controllable light-emission based on a new device principle. Moreover, simultaneous generation of light and ultrasound wave can be observed in this single system.

# Chapter 2 Elements of Relevant Physics

In this chapter, I will provide only the basic theoretical aspects related to this thesis. I first briefly outline the conventional models used for describing the spectroscopic properties of trivalent lanthanide ions. The second part of the chapter is denoted to the ferroelectric properties of ferroelectric ceramics and thin films.

## 2.1 Optical Spectroscopy of Lanthanide Ions

Lanthanide ions doped in host lattice can be considered as impurities that replace the host ions and form the luminescent centers. The spectroscopic properties of lanthanide ions embedded in host materials are quite dissimilar to that of free lanthanide ions. The host material plays a fundamental role in determining the nature of the spectra of the dopant ions. This is known as crystal field theory. The crystal field influences greatly the features of lanthanide ions. It is well known that electric-dipole transitions require a change in parity between initial and final states and therefore are forbidden between 4f states of the lanthanide ions. If a non-centrosymmetric crystal field around the ion, a small admixture of opposite parity states from a higher configuration can be introduced into the original 4f states and thereby electric-dipole transitions become allowed. Judd and Ofelt have shown that under certain simplifying assumptions the probabilities for electric-dipole transitions can be expressed as of sum of a small number of terms involving parameters which contain the strength of the configuration mixing.

### 2.1.1 Free Ions Interaction

The trivalent lanthanide ions (Ln$^{3+)}$ possess the [Xe]4f$^{n}$ (n=0-14) electric configuration. The ground state electronic configuration of Ln$^{3+}$ ions is energetically well separated from the [Xe]4f$^{n-1}$5d$^{1}$ configuration ($\Delta E$ > 32,000 cm$^{-1}$). The optical transitions occurred within the unfilled 4f shell is shielded by the larger radial expansion of the 5s$^{2}$5p$^{6}$ subshells, so the 4f electrons are weakly perturbed by the crystal field. The resulting electronic transitions between the 4f states are very sharp. In the central field approximation, the terms of the Hamiltonian for free ion in the absence of external fields are [Liu, 2005]:

$$H_F = H_0 + H_c + H_{so} \tag{2.1}$$

where

$$H_0 = -\frac{h^2}{2m}\sum_{i=1}^{N}\nabla_i^2 - \sum_{i=1}^{N}\frac{Ze^2}{r_i} \tag{2.2}$$

$$H_c = -\sum_{i<j}^{N}\frac{e^2}{r_{ij}} \tag{2.3}$$

$$H_{so} = \sum_{i=1}^{N}\xi(r_i)(\mathbf{s}_i \cdot \mathbf{l}_i) \tag{2.4}$$

In Eq. (2.2), the first term is the sum of the kinetic energy, the second term is the potential energy of all the electrons in the field of the nucleus. In Eq. (2.3), the term $H_C$ is the inter-electron repulsive Coulomb potential between pairs of electrons. In Eq. (2.4), the term $H_{SO}$ represents spin-orbit interaction, which accounts for magnetic dipole-dipole interactions between the spin and angular moment of the electrons. In the central field approximation, each electron can be considered to move independently in the field of nucleus and a spherically averaged potential of all the other electrons [Hartree, 1957]. So for free lanthanide ions, there is a spherical symmetry in the absence of crystal field. There are three types of radiative transition probabilities for lanthanide ions: magnetic dipole transitions, electric dipole transitions, and electric quadrupole transitions. Among them, magnetic dipole and electric quadrupole transitions between states of the ground 4f configuration of trivalent lanthanide ions are parity allowed, but their intensity is weak. Electric dipole transitions are known to be forbidden between 4f states of lanthanide ions by the Laporte selection rule. When a lanthanide ion doped in a crystal site without inversion symmetry, the spherical symmetry of lanthanide ions is destroyed. Such electric dipole transitions require a change in parity between initial and final states and electric dipole transitions can be forced if an admixing of states of opposite parity from higher configuration are introduced into the 4f states. The crystal field also removes the ($2J+1$) fold degeneracy of the free ion $J$ levels, giving rise to the familiar crystal field Stark splitting.

### 2.1.2 The Crystal Field Effect

When the lanthanide ions are doped into a crystalline material, the behavior of lanthanide ions in crystals is obviously different from the free ion. The spherical symmetry of its electric structure is destroyed, and energy levels split under the influence of the crystal field. The Hamiltonian of the lanthanide ions in a crystal is written as,

$$H = H_F + H_{CF} \tag{2.5}$$

where $H_{CF}$ is the perturbation Hamiltonian, which is due to the potential provided by the crystal environment around the ion. The perturbation Hamiltonian $H_{CF}$ in terms of spherical harmonics,

$$H_{CF} = \sum_{kq} A_{kq} \sum_{i} r_i^k V_{kq}(\theta_i, \varphi_i) \tag{2.6}$$

where $r_i$ is the radial coordinate of the *i*th electron. $V_{kq}(\theta_i, \varphi_i)$ is the *q*th component of the spherical harmonic of order *k*. $\theta_i$ and $\varphi_i$ are the angular coordinates of the *i*th electron. $A_{kq}$ are the parameters which depend on the specific crystal-symmetry group. For the lanthanide ions, the magnitude of the crystal field splitting $H_{CF}$ compared to the Coulomb interaction $H_C$ and the spin orbit interaction $H_{SO}$ is weak.

### 2.1.3 Electronic Dipole Transitions

The operators for odd-parity electric dipole, magnetic dipole and electronic quadrupole are given by [Bartolo, 2006]

$$\vec{P} = -e\sum_i \vec{r}_i \tag{2.7}$$

$$\vec{M} = -\frac{eh}{4\pi mc}\sum_i (\vec{l}_i + 2\vec{s}_i) \tag{2.8}$$

$$\vec{Q} = \frac{1}{2}\sum_i (\vec{k}\cdot\vec{r}_i)\vec{r}_i \tag{2.9}$$

respectively. Electric dipole transitions require a change in parity between initial and final states. So the intra-4f transitions of lanthanides are forbidden. Electric dipole transitions become allowed only when the ions in a solid which induces an admixing of states of opposite parity from higher configurations into 4f. The states of the system may be labelled by the usual set of quantum numbers $L$, $S$, $J$. The term symbol used to represent the states and spectral transitions of atoms has the form ${}^{2S+1}L_J$, where $S$ is the total spin quantum number, $L$ is the total orbital quantum number, and $J$ is the total angular momentum quantum number. So the selection rules for electric dipole transitions include

$$\Delta S = 0,\ \Delta L = 0, \pm 1,\ \Delta J = 0, \pm 1 \tag{2.10}$$

Although some magnetic dipole transitions have been noticed, the observed spectra of lanthanide ions consist mainly of electric dipole transitions. Broer and co-researcher had demonstrated that the observed intensities of electric dipole transition were in almost all cases stronger than magnetic dipole or electric quadrupole radiation [Broer, 1945]. Magnetic dipole transitions are parity allowed between states of 4f. The selection rules for magnetic dipole transition is given by

$$\Delta S = 0\,,\ \Delta L = 0\,,\ \Delta J = 0, \pm 1 \tag{2.11}$$

Electric quadrupole transitions are also parity allowed between states of 4f. Quadrupole radiation accounts for all the transitions, but it is too weak to compare with odd-parity electric dipole transitions. The selection rules for electric quadrupole transitions are defined by

$$\Delta S = 0\,,\ \Delta L, \Delta J = 0, \pm 1, \pm 2 \tag{2.12}$$

The selection rules for electric dipole, magnetic dipole, and electric quadrupole transitions are shown in Table 2.1.

Table 2.1 The selection rules for electric dipole, magnetic dipole and electric quadrupole transitions [Bartolo, 2006].

| | S | L | J | Parity |
|---|---|---|---|---|
| Electric Dipole | $\Delta S = 0$ | $\Delta L = 0, \pm 1$ | $\Delta J = 0, \pm 1$ | opposite |
| Magnetic Dipole | $\Delta S = 0$ | $\Delta L = 0$ | $\Delta J = 0, \pm 1$ | same |
| Electric Quadrupole | $\Delta S = 0$ | $\Delta L = 0, \pm 1, \pm 2$ | $\Delta J = 0, \pm 1, \pm 2$ | same |

There are three types of electronic transitions involving lanthanide ions: sharp intra-4f transitions, broader 4f-5d transitions, and broad charge-transfer transitions. Most visible and infra-red electronic transitions are predominantly within the 4f configuration, while UV and VUV transitions involve 4f5d or charge-transfer states. Extensive researches of energy levels of the 4f configurations of lanthanide ions in various host lattices were carried out in 1960s [Judd, 1962; Krupke, 1966; Weber, 1967; Carnall, 1968;]. The lanthanides usually exist as trivalent cations. Electric-dipole transitions are forbidden in the absence of an odd-parity interaction with the crystal. Laporte's parity selection rule implies that states with even parity can be connected by electric dipole transitions. The shielding of the 4f electrons by $5s^2$ and $5p^6$ sub-shells results in sharp and narrow 4f-4f transition bands.

### 2.1.4 Judd-Ofelt Theory

Generally speaking, electric dipole transitions require a change in parity between the initial and final states. So, electric dipole transitions are forbidden between 4f states of the lanthanide ions. However, this is possible when the ions are placed in a non-centrosymmetric static or dynamic crystal field. The odd parity states from higher lying configurations outside the 4f shell, such as 4f5d, are mixed into the 4f states and as a result, the electric dipole transitions become allowed. Judd and Ofelt independently have proposed a general theoretical framework for calculating the intensities of such transitions. The Judd-Ofelt (J-O) theory describes the intensities of lanthanide 4f-4f transitions in solids and solutions. According to the Judd-Ofelt theory [Judd, 1962; Ofelt, 1962], the oscillator strength can be calculated from

$$P_{cal} = P_{ed} + P_{md} = \frac{8\pi^2 mcv}{3h(2J+1)e^2 n^2}(\chi_{ed} S_{ed} + \chi_{md} S_{md}) \qquad (2.13)$$

where $m$ is the electron mass and $e$ is the electron charge, $c$ is the light velocity. $J$ is the total angular momentum quantum number of the ground state. $\chi_{ed}$ and $\chi_{md}$ are the electric and magnetic field corrections for the refractive index $n$, respectively, are given by

$$\chi_{ed}=\frac{n(n^2+2)^2}{9} \tag{2.14}$$

and

$$\chi_{md}=n^3 \tag{2.15}$$

The electric dipole and magnetic dipole, $S_{\mathrm{ed}}$ and $S_{\mathrm{md}}$ are expressed as

$$S_{ed}(J,J')=e^2\sum_{t=2,4,6}\Omega_t\left|\left\langle 4f^n[S,L]J\right|U^{(t)}\left|4f^n[S',L']J'\right\rangle\right|^2 \tag{2.16}$$

$$S_{md}(J,J')=\frac{e^2}{4m^2c^2}\left|\left\langle 4f^n[S,L]J\right|L+2S\left|4f^n[S',L']J'\right\rangle\right|^2 \tag{2.17}$$

The $\Omega_t$ parameters are known as the Judd-Ofelt parameters, and can be determined from a least squares fit to the values of experimental data. The spontaneous emission probabilities $A(J,J')$ of the electronic transitions are given in the Judd-Ofelt theory by

$$A(J,J')=A_{ed}+A_{md}=\frac{64\pi^2v^3}{3h(2J+1)}(\chi_{ed}S_{ed}+\chi_{md}S_{md}) \tag{2.18}$$

## 2.2 Ferroelectric Thin Films and Ceramics

Ferroelectric materials such as $BaTiO_3$ (BTO) and $KNbO_3$ (KNO), have proven to be successful host for their high electro-optic and non-linear optical coefficients. Rare-earth-doped ferroelectric materials have attracted for their applications in micro-electronics and optoelectronics. The unique crystal structure of ferroelectric materials provides us an opportunity to couple variables including electric field and temperature to crystal symmetry in a single compound. Ferroelectric and piezoelectric properties of ferroelectric ceramics and thin films are briefly introduced with the aim of understanding factors may affect the behaviour of ferroelectrics.

### 2.2.1 Spontaneous Polarization

Ferroelectric materials possess a domain structure and spontaneous polarization at temperatures below the Curie point, in which the direction of the spontaneous polarization can be switched by an external electric field. Not every dielectric is a ferroelectric. According to the crystallographic symmetry, crystals can be classified into 32 point groups. Among these 32 crystal point groups, crystals that belong to 20 non-centrosymmetric point groups can exhibit the piezoelectric effect. 10 of the piezoelectric point groups possess a polar axis and exhibit spontaneous polarization in the absence of an external electric field. The 10 polar point groups include 1, 2, *m*, 2*mm*, 4, 4*mm*, 3, 3*m*, 6, and 6*mm*. All ferroelectric crystals belong to one of these 10 point groups.

The reason for spontaneous polarization in ferroelectric crystals is briefly explained below. If one particular lattice vibration is less than the crystal energy, the ions will shift and stabilize the crystal structure so as to minimize the energy. With the temperature decreases, this particular vibration mode becomes stabilized, the vibration mode frequency decreases (soft phonon mode), and finally at a certain temperature, this frequency becomes zero (phase transition).

### 2.2.2 Landau Theory of the Phase Transition

The Laudau free energy as a function of the polarization P and temperature T can be written as [Strukov, 1998]

$$F(P,T)=\frac{1}{2}\alpha P^2+\frac{1}{4}\beta P^4+\frac{1}{6}\gamma P^6+\ldots \tag{2.19}$$

the coefficients $\alpha$, $\beta$, $\gamma$, are temperature dependent. The equilibrium polarization under an applied electric field E follows that

$$\frac{\partial F}{\partial P}=\alpha P+\beta P^3+\gamma P^5 \tag{2.20}$$

For a crystal in ferroelectric state, the coefficient of the $P^2$ term must be negative so that the polarized state can be stable. While if the crystal in paraelectric state, the $P^2$ term should be positive and passes through zero at the Curie-Weiss temperature $T_0$.

$$\alpha=\frac{T-T_0}{\varepsilon_0 C} \tag{2.21}$$

where $C$ is a positive constant called the Curie-Weiss constant. $T_0$ is equal to or lower than the transition temperature $T_c$ (Curie temperature). When $\beta$ is positive, $\gamma$

can be neglected. Under zero electric field, the polarization is obtained from Eq. (2.20) as

$$\frac{T-T_0}{\varepsilon_0 C}P_S+\beta P_S{}^3=0 \tag{2.22}$$

to satisfy Eq. (2.22), $P_S=0$ or $P_S{}^2=\dfrac{T-T_0}{\beta\varepsilon_0 C}$.

For $T>T_0$, this yields the unique solution $P_S=0$. For $T<T_0$, the minimum of the Laudau free energy is obtained at

$$P_S=\sqrt{\frac{T-T_0}{\beta\varepsilon_0 C}} \tag{2.23}$$

The relative permittivity $\varepsilon$ can be written as

$$\varepsilon=\frac{1}{\varepsilon_0(\alpha+3\beta P^2)} \tag{2.24}$$

In combination, then yields

when $T>T_0$, $P_S=0$, and $\varepsilon=\dfrac{C}{T-T_0}$; When $T<T_0$, from Eqs. (2.21) and (2.23), then yields $P_S=\sqrt{\dfrac{T-T_0}{\beta\varepsilon_0 C}}$, and $\varepsilon=\dfrac{C}{2(T-T_0)}$. The polarization $P_S$ goes continuously to zero at the phase transition temperature $T_C$, this kind of phase transition is called a second-order transition. For second-order transition, the phase transition temperature $T_C$ equals to Curie-Weiss temperature $T_0$ (Figure 2.1).

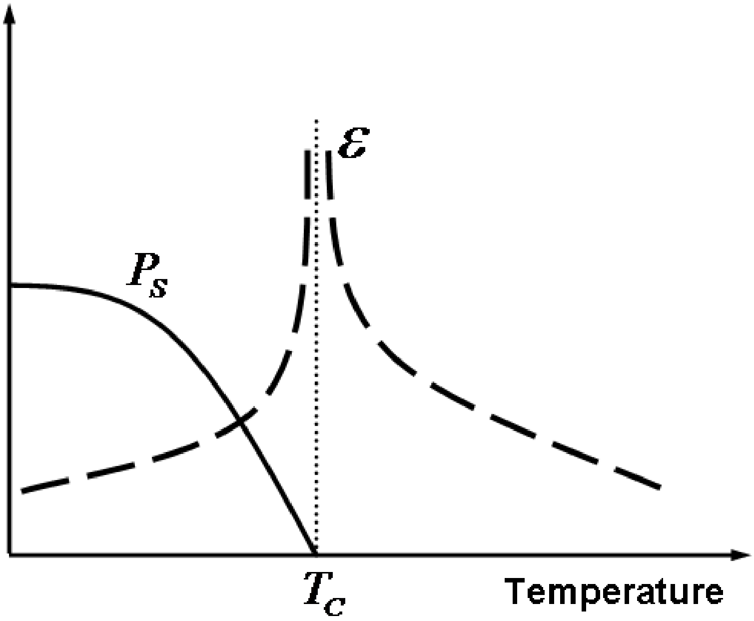

Figure 2.1. Schematic temperature dependence of the dielectric permittivity $\varepsilon$ and spontaneous polarization $P_S$ for a second-order ferroelectric [Damjanovic, 1998].

When $\beta$ is negative, then $\gamma$ should be positive. To realize the equilibrium condition for zero electric field, $P_S = 0$ or it follows that

$$\frac{T-T_0}{\varepsilon_0 C} P_S + \beta P_S^3 + \gamma P_S^5 = 0 \tag{2.25}$$

then yields

$$P_S^2 = \frac{-\beta + \sqrt{\beta^2 - 4\gamma \frac{T-T_0}{\varepsilon_0 C}}}{2\gamma} \tag{2.26}$$

the transition temperature $T_C$ can be obtained to satisfy the condition that the free energies of the paraelectric and ferroelectric phases are equal

$$\frac{T-T_0}{\varepsilon_0 C}+\frac{1}{2}\beta P_S^{\ 2}+\frac{1}{3}\gamma P_S^{\ 4}=0 \tag{2.27}$$

therefore, the combination of Eq. (2.26) and (2.27),

$$T_C=T_0+\frac{3}{16}\left(\frac{\beta^2\varepsilon_0 C}{\gamma}\right) \tag{2.28}$$

So it can be seen that the Curie temperature $T_C$ is higher than the Curie-Weiss temperature $T_0$. $P_S$ also exhibits a discrete jump at $T_C$, and the permittivity presents a finite maximum at $T_C$. This kind phase transition is called first-order transition (Figure 2.2). Some ferroelectric materials, such as barium titanate ($BaTiO_3$) is an example of a ferroelectric undergo first-order phase transition.

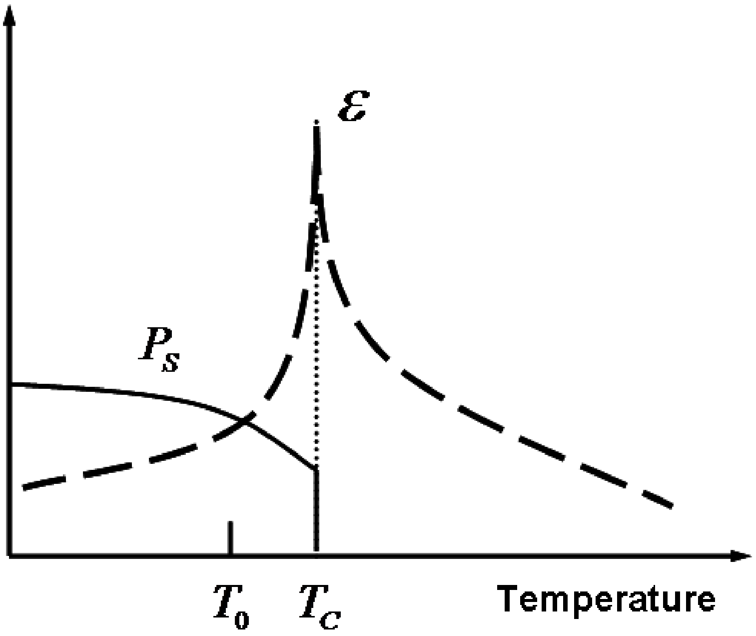

Figure 2.2. Schematic temperature dependence of the dielectric permittivity ε and spontaneous polarization $P_S$ for a first-order ferroelectric [Damjanovic, 1998].

### 2.2.3 Poled Ferroelectric Materials

The spontaneous polarization in a ferroelectric crystal exhibits zero net polarization due to the random orientation of grains and domains [Damjanovic, 1998]. The direction of the spontaneous polarization is usually not uniformly aligned throughout the whole crystal. The regions of the crystal with uniformly oriented spontaneous polarization are called ferroelectric domains (Figure 2.3). The region between two domains is called the domain wall. Domain walls are characterized by the angle between the directions of polarization on either side of the wall. The walls which separate domains with oppositely oriented polarization are called 180° walls and those with perpendicular polarization are called 90° walls. Ferroelectric domains contribute to minimize the electrostatic energy of depolarizing fields.

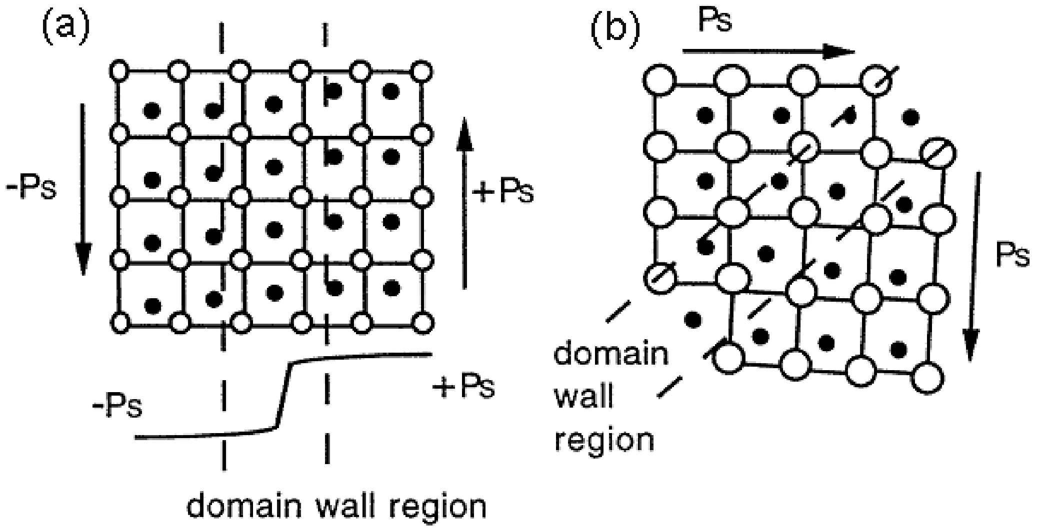

Figure 2.3. Schematic illustration of ferroelectric domains and domain walls in tetragonal perovskite ferroelectric. (a) 180°. (b) 90°. [Damjanovic, 1998].

Ferroelectric grains in ceramics and polycrystalline films always compose of many domains. An unpoled ferroelectric material exhibits zero net polarization due to the random orientation of grains and domains. Polycrystalline ferroelectric materials can be poled into a polar state by applying a strong electric field. During the poling process, grains in crystal can not reorient, but the domains within individual grains can reorient in the direction of the electric field (Figure 2.4). The polarization after the removal of the electric field is called remanent polarization.

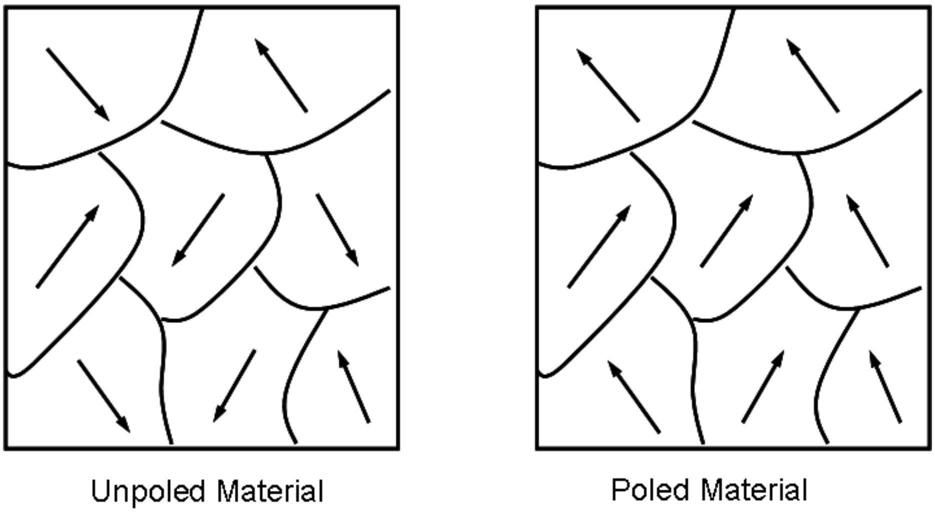

Figure 2.4. A polycrystalline ferroelectric with random orientation of grains before and after poling.

### 2.2.4 Ferroelectric Hysteresis Loop

An important characteristic of ferroelectric materials is the occurrence of hysteresis in the relation between input fields E and output polarization P. The ferroelectric hysteresis loop can be observed by using a Sawyer-Tower circuit as shown in Figure 2.5.

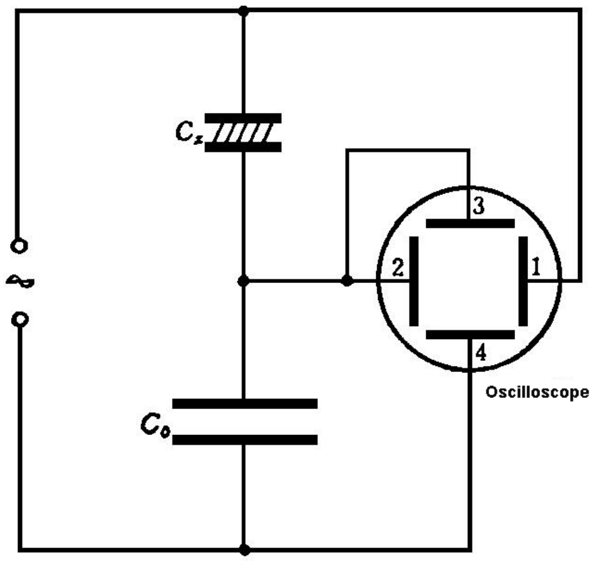

Figure 2.5. The Sawyer-Tower circuit [Sawyer, 1930].

At small values of the AC electric field, as shown in Figure 2.6, the polarization increases with the field amplitude. In the region AB, the polarization of domains starts to switch in the direction of the electric field as the field increased. The polarization response in this region is nonlinear with the electric field. All dipoles in domains are aligned with the electric field (Point B). After all domains are aligned, increasing the filed beyond this point the ferroelectricity again behaves linearly (segment BC). Then the electric field strength starts to decrease, some domains will switch back. At zero electric field, the polarization is nonzero, the ferroelectric exhibits a positive remanent polarization $P_r$. Further decease the electric field to the negative values will cause a new alignment of dipoles. As the electric field is reduced through the negative coercive field -$E_c$, the polarization comes to zero. Still increase the electric field in the negative direction, all dipole orient with the negative electric field. Increasing the electric field to zero causes dipoles to reorient to the negative remanent polarization –$P_r$. The remanent polarization, coercive field and the shape of hysteresis loop may be influenced by many factors including the thickness of the film, the charged defects, mechanical stresses, and sample preparation.

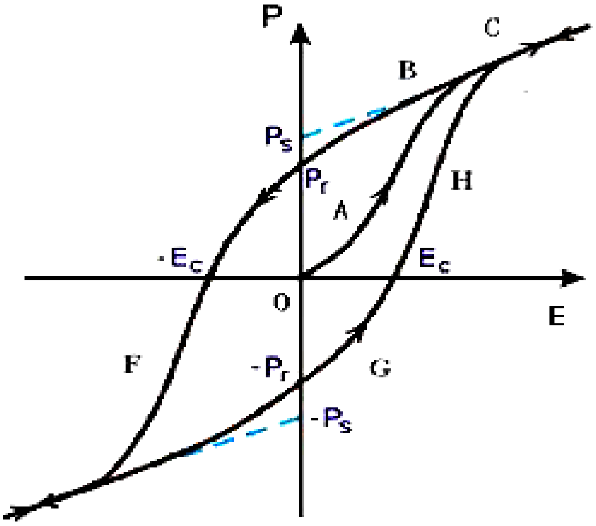

Figure 2.6. Hysteresis loop showing polarization switching in ferroelectric materials. Important parameters such as coercive field (Ec), remnant polarization (Pr) and saturation polarization (Ps) are indicated.

### 2.2.5 Crystal Symmetry

Ferroelectric materials exhibit a domain structure and spontaneous polarization at the temperature below the Curie point. Above the Curie temperature $T_C$, the dielectric permittivity accords to the Curie-Weiss law

$$\varepsilon = \varepsilon_0 + \frac{C}{T - T_0} \approx \frac{C}{T - T_0} \tag{2.29}$$

where $C$ is the Curie constant, $T_0$ is the Curie-Weiss temperature. Most ferroelectric materials undergo successive structural phase transition from a high-temperature paraelectric phase into a low-temperature ferroelectric phase. The symmetry of the ferroelectric phase is always lower than the symmetry of the paraelectric phase. $BaTiO_3$ (BTO) is a well-known classic ferroelectric material which is cubic above 393 K with the space group $Pm3m$ ($O_h$). Below the Curie temperature, BTO is ferroelectric of a tetragonal form, which further transforms to orthorhombic and rhombohedral structures at 278 and 183 K, respectively as illustrated in Figure 2.7. From high temperature to low temperature, BTO tends to lower symmetry phases. The host symmetry has great influence on the optical properties of dopant ions. So the substituted lanthanide ions may be used as a structural probe for ferroelectrics.

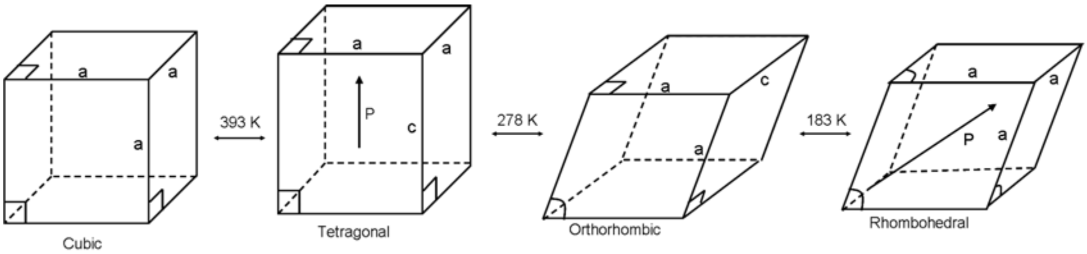

Figure 2.7. Cubic, tetragonal, orthorhombic and rhombohedral structures and approximate transition temperature for $BaTiO_3$.

BTO is selected as ferroelectric host because it has been regarded as a model system for investigating crystal structure transformation under mechanical stress, electric field, and temperature. The piezoelectric effects in tetragonal BTO are the effects of coupling between the external electric field and the electric spontaneous polarization (P) that arises from the Ti off-centering displacement along the *c*-axis of the tetragonal structure. Under the applied electric field, the Ti ion shifted along the electric field direction. When an electric field is applied along the direction of spontaneous polarization, the *c*-axis of the lattice elongates, giving rise to the lattice distortion (indicated by the dashed lines). In principle, an increase in asymmetry of the BTO host, approaching lower symmetry around lanthanide ions. The lower symmetry at the site of lanthanide ions subsequently increases the 4f transition probabilities of the dopant ions.

### 2.2.6 Piezoelectricity

Piezoelectricity is linear electromechanical systems in crystalline materials with non-inversion symmetry. The direct piezoelectric effect is defined as the change of electric polarization proportional to the mechanical strain. The piezoelectric effect strongly depends on the symmetry of the crystal. Among 32 crystal classes, 21 classes are non-centrosymmetric, and of these with one exception, 20 classes exhibit piezoelectricity. 10 of these classes show a spontaneous polarization without mechanical stress, and the spontaneous polarization can be reversed by an electric field, the materials is said to be ferroelectric. Piezoelectric materials also show the opposite effect, called converse piezoelectric effect, where the application of an electrical field creates mechanical deformation in crystal. Figure 2.8a shows a free piezoelectric material which has been polarized. If the material is compressed, then a voltage of the same polarity as the poling voltage will appear (Figure 2.8b). If stretched, there will be a voltage with opposite polarity (Figure 2.8c). For converse piezoelectric effect, when a negative electric field is applied to the positively polarized material, the lattice of the material will contract along the *c* axis and expand perpendicular to that direction (Figure 2.8d). In contrast, upon the positive electric field, the material will expand along the *c* axis and contract perpendicular to that direction (Figure 2.8e).

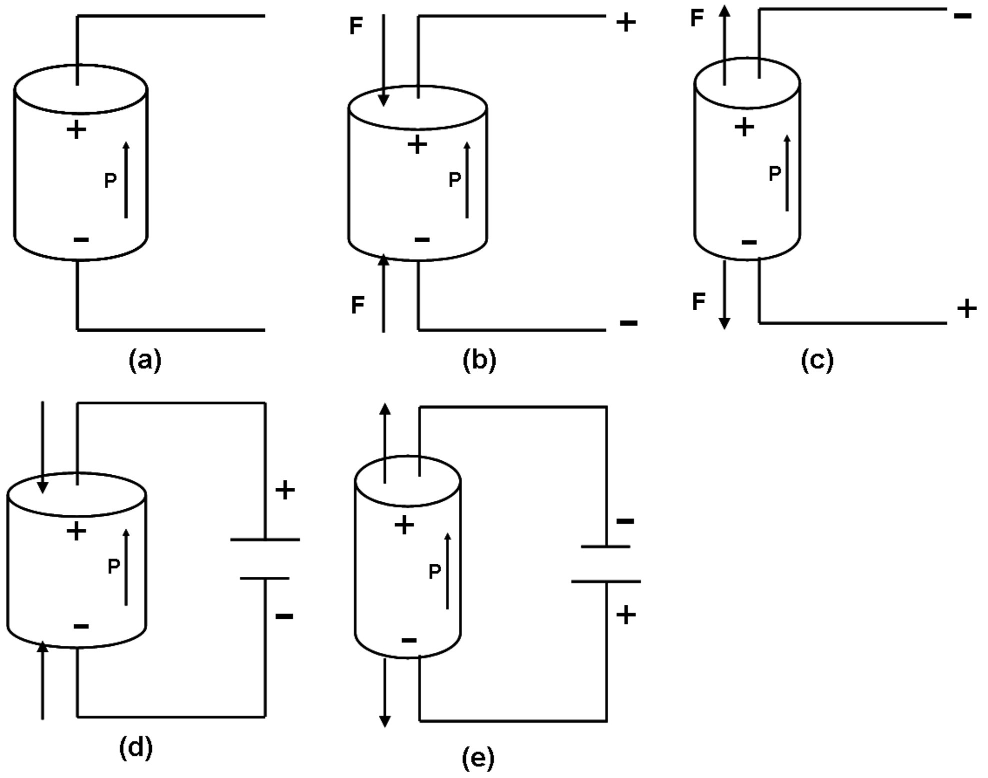

Figure 2.8. Schematic diagrams showing the piezoelectric and converse piezoelectric effect.

The piezoelectric equations [Damjanovic, 1998] are

$$\{S\} = [s^E]\{T\} + [d^t]\{E\} \tag{2.30}$$

$$\{D\} = [d]\{T\} + [\varepsilon^T]\{E\} \tag{2.31}$$

where $D$ is the electric charge density displacement, $\varepsilon$ is permittivity, $E$ is electric field strength, $S$ is strain, $s$ is compliance, $T$ is stress, $[d]$ is the matrix for direct piezoelectric effect and $[d^t]$ is the matrix for converse piezoelectric effect. The strain-charge for a material of the 4mm ($C_{4v}$) crystal class (such as tetragonal BTO and $PbZr_xTi_{1-x}O_3$, PZT) can also be written as

$$\begin{bmatrix} S_1 \\ S_2 \\ S_3 \\ S_4 \\ S_5 \\ S_6 \end{bmatrix} = \begin{bmatrix} s_{11}^E & s_{12}^E & s_{13}^E & 0 & 0 & 0 \\ s_{21}^E & s_{22}^E & s_{23}^E & 0 & 0 & 0 \\ s_{31}^E & s_{32}^E & s_{33}^E & 0 & 0 & 0 \\ 0 & 0 & 0 & s_{44}^E & 0 & 0 \\ 0 & 0 & 0 & 0 & s_{55}^E & 0 \\ 0 & 0 & 0 & 0 & 0 & s_{66}^E = 2(s_{11}^E - s_{12}^E) \end{bmatrix} \begin{bmatrix} T_1 \\ T_2 \\ T_3 \\ T_4 \\ T_5 \\ T_6 \end{bmatrix} + \begin{bmatrix} 0 & 0 & d_{31} \\ 0 & 0 & d_{32} \\ 0 & 0 & d_{33} \\ 0 & d_{24} & 0 \\ d_{15} & 0 & 0 \\ 0 & 0 & 0 \end{bmatrix} \begin{bmatrix} E_1 \\ E_2 \\ E_3 \end{bmatrix} \tag{2.32}$$

$$\begin{bmatrix} D_1 \\ D_2 \\ D_3 \end{bmatrix} = \begin{bmatrix} 0 & 0 & 0 & 0 & d_{15} & 0 \\ 0 & 0 & 0 & d_{24} & 0 & 0 \\ d_{31} & d_{32} & d_{33} & 0 & 0 & 0 \end{bmatrix} \begin{bmatrix} T_1 \\ T_2 \\ T_3 \\ T_4 \\ T_5 \\ T_6 \end{bmatrix} + \begin{bmatrix} \varepsilon_{11} & 0 & 0 \\ 0 & \varepsilon_{22} & 0 \\ 0 & 0 & \varepsilon_{33} \end{bmatrix} \begin{bmatrix} E_1 \\ E_2 \\ E_3 \end{bmatrix} \tag{2.33}$$

where Eq. (2.32) represents the relationship for converse piezoelectric effect and Eq. (2.33) is for the direct piezoelectric effect.

# Chapter 3 Experimental Techniques

Rare-earth-doped polycrystalline powders as well as the targets for pulsed laser deposition were prepared by solid-state reaction method. All thin films investigated in this study were deposited by pulsed laser deposition method. Their structure characteristics were determined by X-ray diffraction, Raman spectroscopy, transmission electron microscope and scanning electron microscope. The luminescent properties of samples were studied by using a fluorescence spectrometer.

## 3.1 Sample Preparation

### 3.1.1 Solid-state Reaction

Rare-earth-doped polycrystalline powders as well as the targets for pulsed laser deposition were prepared by solid-state reaction synthesized method [Fluvkiger, 1977]. The processing flow diagram is described in Figure 3.1. Reagent grade materials are used as raw materials. Based on the designed formulas, the starting powders with designed stoichiometric quantities are ball milled, then dried and calcinated generate the rare-earth-doped powders. These powders sample can be used for PL measurements. The as-prepared powders are further processed into the targets used for pulsed laser deposition. These powders are pressed into disk pellets and sintered, then we obtain the targets for pulsed laser deposition.

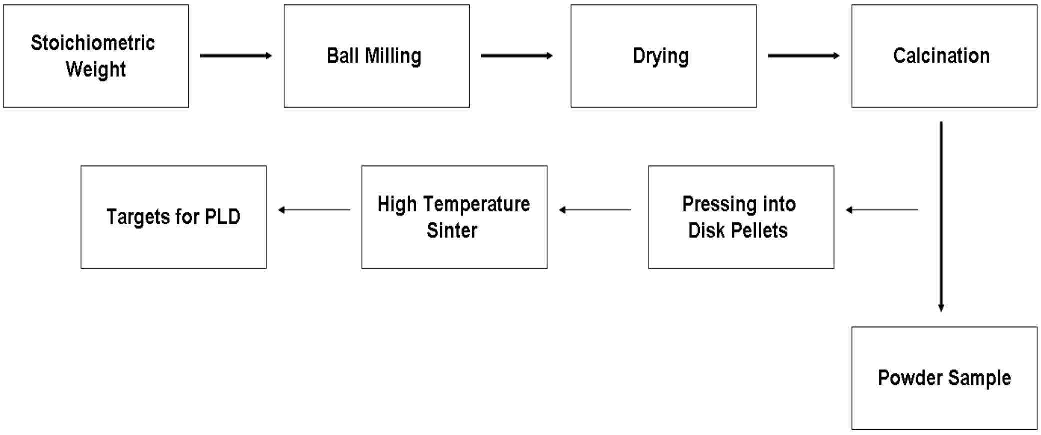

Figure 3.1. Flow diagram of the sample's preparation procedure.

### 3.1.2 Pulsed Laser Deposition (PLD)

Pulsed laser deposition (PLD) is one of the most widely used techniques for the growth of thin films developed in the recent years [Chrisey, 1994]. All the thin film samples used in the thesis are prepared by PLD. The PLD technique of thin film growth involves evaporation of a target of the material to be deposited in an ultra high vacuum or in the presence of a background gas. The basic set-up of PLD is shown in Figure 3.2. A high power pulsed laser is focused to strike the target. The physical phenomena of laser-target interaction and film growth are quite complex. The focused short pulse laser results in sufficiently high flux densities. Within the incident laser pulse penetration depth, the atoms of the target material are rapidly evaporated. The materials emitted from the target surface travel in a plasma form. The density of the plasma varies as a function of cos($x$) with a Gaussian curve shape. The high-energy species ablated from the target impinge onto the substrate surface and may cause some damage to the surface. They may sputter some atoms form the substrate surface and also form a collision region with these sputtered species from the substrate. This thermalized region serves as a source for condensation of particles. When the condensation rate is higher than the rate of particles from the sputtering, once thermal equilibrium reaches, the film grows on the substrate surface. The critical growth parameters for the nucleation process and the growth of the film include the deposition rate, the substrate temperature, substrate surface conditions and background pressure.

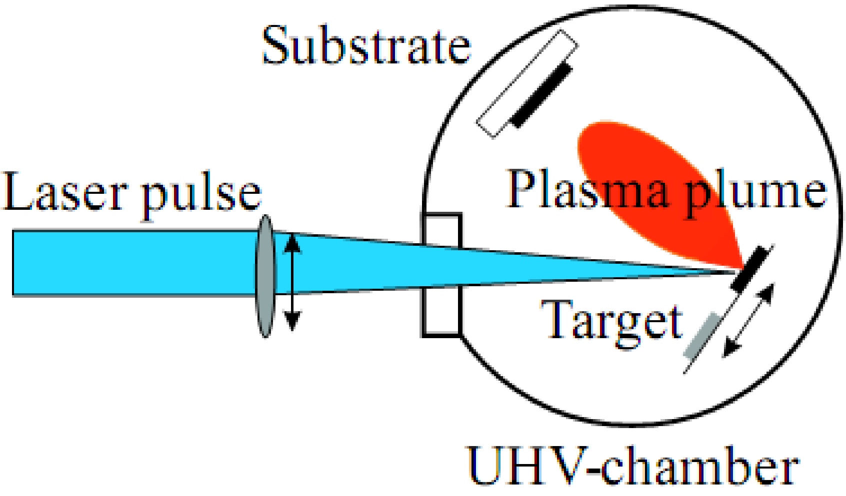

Figure 3.2. Schematic diagram of a typical PLD set-up [Kramer, 2003].

## 3.2 Characterization

### 3.2.1 X-ray Diffraction (XRD)

The crystalline of the bulk materials and thin films were investigated by X-ray diffraction (XRD). X rays are scattered by the electron clouds of the individual atoms in a crystal. The interference between the elastic scattered X rays can result in a diffraction pattern. The diffraction pattern contains information about the architecture of atoms of materials and thin films. XRD was first used to reveal the three-dimensional arrangement information in a crystal by William Lawrence Bragg in 1913. A crystal is a solid that has an order repeating pattern in three spatial dimensions. Crystals are classified into seven crystal systems (triclinic, monoclinic, orthorhombic, tetragonal, trigonal/rhombohedral, hexagonal, and cubic), which are combined with four crystal lattice types (primitive, single-face-centered, face-centered, and body-centered) to give 14 Bravais lattices. These Bravais combined with symmetry elements result in 230 space groups. All crystals belong to one of 230 space groups. The distances between atoms or ions in a crystal are of the order of $10^{-9}$ to $10^{-10}$ m. In order to investigate the fine crystal structure, it is necessary to employ a radiation source with a wavelength comparable to or smaller than the dimensions of the interatomic distances. X rays have high energies ranging from about 100 eV to 10 MeV, responding to wavelength ranging from about 10 to $10^{-3}$ nm. When a parallel beam of X-rays is incident on the testing sample, the incident X-ray beam will be reflected from the crystal planes. As shown in Figure 3.3, the angle between the incident X-ray and the normal to the reflection plane is equal to the angle of reflection. The incident X-ray, the plane normal, and the diffracted X-ray are coplanar. When the Bragg equation derived by Bragg is satisfied, thus the diffraction maxima occur.

$$n\lambda = 2d_{hkl}\sin\theta \tag{3.1}$$

Where $\lambda$ is the wavelength of X-rays used, $n$ is the order of reflection, $d_{hkl}$ is the perpendicular spacing between the lattice plane in the crystal, $\theta$ is the complement ($90-\theta$) of the angle of incident of the X-ray beam, and $h$, $k$, and $l$ are the Miller index.

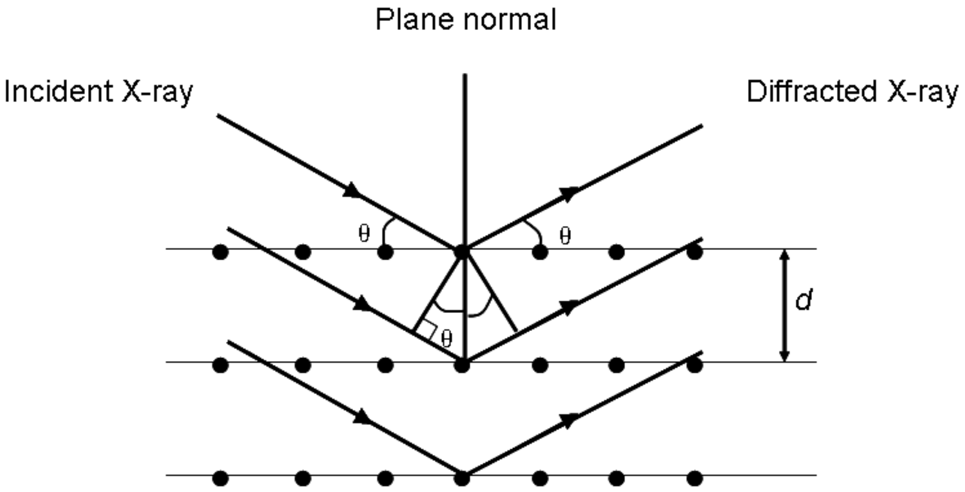

Figure 3.3. The schematic diagram of X-ray diffraction.

### 3.2.2 Atomic Force Microscopy (AFM)

Atomic force microscopy (AFM) was firstly made in 1986 [Binnig, 1986]. Since then, AFM has become an inevitable tool for researchers in the physics, chemistry, and biological sciences. AFM operates by scanning with an atomically sharp tip very close to the surface of the interest sample. AFM works in constant height or constant force mode by response the attractive or repulsive forces between the tip and the sample surface. The major forces that measured in AFM include Van der Waals, electrostatic, hydrophobic, hydrophilic, and magnetic forces, etc. Today, most AFMs use a laser deflection system as shown in Figure 3.4. When the tip is brought close to the surface of sample, forces between the tip and the sample leads to a deflection of the cantilever. A diode laser light is focused at the top surface of the cantilever, then reflected into an array of photodiodes that provides the feedback signal for the deflection. AFM can provide three-dimensional surface profile of samples. Additionally, it can supplement scanning electron microscopy, samples for AFM does not require surface treatment and need not be electrically conductive. Most measurements of AFM can be operated at ambient conditions.

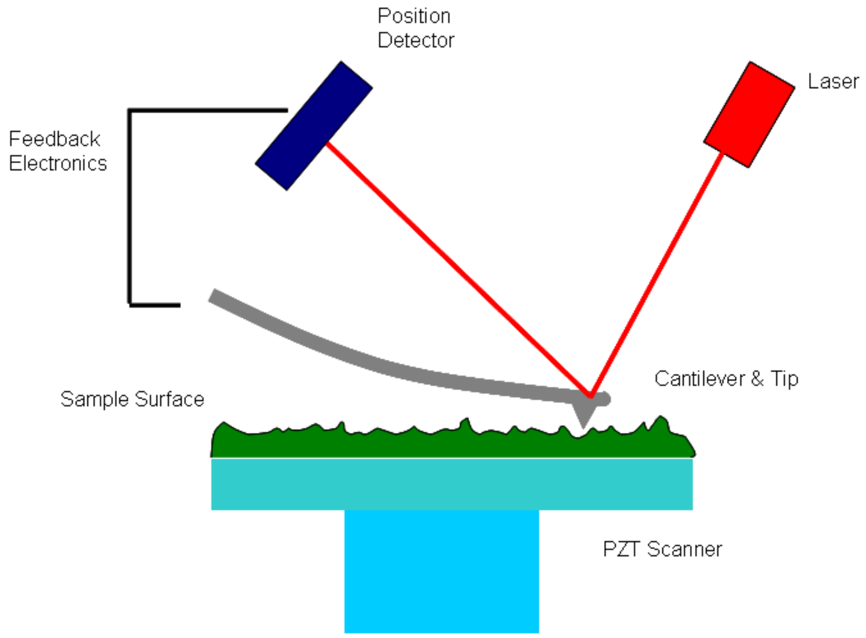

Figure 3.4. The schematic diagram of atomic force microscopy.

### 3.2.3 Transmission Electron Microscopy (TEM)

Transmission electron microscopy (TEM) has become a basic technique and inevitable for the microstructural characterization of materials. In practice, TEM employs a high energy electron beam transmitted across an ultra thin specimen. The electrons are focused with electromagnetic lenses on imaging devices, such as fluorescent screen, or recorded on photographic film or detected by a CCD camera. Theoretically, the maximum resolution is limited by the wavelength of the photons used to probe the sample. The wavelength of electrons is dominated by the de Broglie equation to the kinetic energy of an electron. The electrons are accelerated by several hundred kV, giving wavelengths much smaller than that of light. Thus, the resolution for TEM is many orders of magnitude better than that of light microscope.

### 3.2.4 Scanning Electron Microscopy (SEM)

The scanning electron microscope (SEM) is a microscope that uses electrons rather than light to image a sample. The SEM utilizes a focused high-energy beam of electrons generate a variety of information of the surface of the sample. The electron beam comes from an electron Gun. The electron beam travels through electromagnetic fields and lenses, which focus the beam down toward the sample. Once the high-energy electrons hit the sample, a variety of signals derive from electron-sample interaction as shown in Figure 3.5. These signals include secondary electrons, backscattered electrons, diffracted backscattered electrons, characteristic X-ray, transmitted electrons and visible light. Secondary electrons and backscattered electrons are commonly used for imaging samples. Secondary electrons are used to show the morphology and topography of samples. Backscattered electrons are used for illustrating contrasts in composition of samples. The characteristic X-ray is used to identify the composition of elements in the samples. The SEM has many advantages over traditional optical microscope. The spatial resolution of the SEM depends on the wavelength of the electrons and the electron-optical system which controls the scanning beam. The wavelength of the electrons is much smaller than that used in optical microscope. So the SEM has mach higher resolution. In addition, the SEM can provide a variety of information that contains the sample's surface topography, composition, and other properties in one time. All of these advantages make the SEM become the most useful instruments in research today.

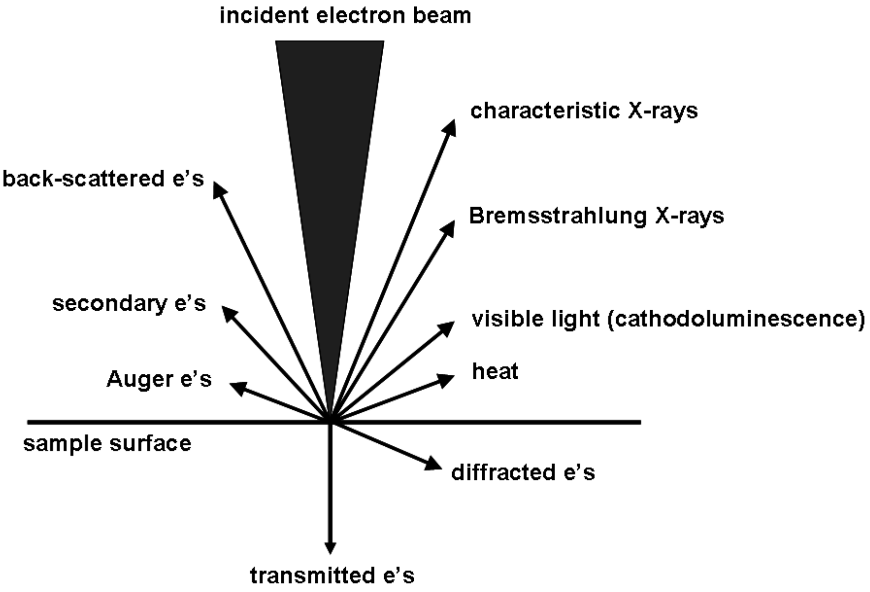

Figure 3.5. The schematic diagram of interactions between electrons and a sample.

## 3.3 Optical Spectroscopy

### 3.3.1 Steady-state and Time-resolved Photoluminescence (PL)

Steady-state PL includes both excitation and emission spectra. An emission spectrum is the wavelength distribution of photons emitted by atoms or molecules measured at a single constant excitation wavelength. An excitation spectrum is conversely, whereby the emission is measured at a single emission wavelength, upon scanning the excitation wavelength. All the PL spectra in the thesis are measured by Edinburgh FLSP920 spectrometer as shown in Figure 3.6. The FLSP 920 is a modular, computer controlled spectrometer for measuring steady-state and time resolved luminescence spectra in the ultraviolet-near infrared spectra range.

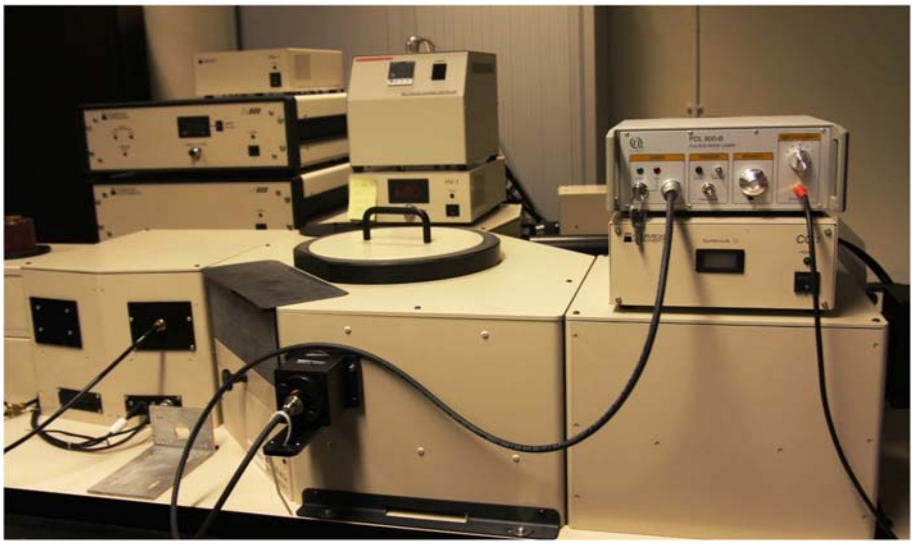

Figure 3.6. Picture of Edinburgh FLSP920 spectrometer used in our laboratory.

We briefly describe the individual functional components (Figure 3.7) of the Edinburgh FLSP920 spectrometer system in our laboratory.

**Light Sources:**

- Xe900 Xenon Arc Lamp is a 450W ozone free xenon arc lamp that emits continuous radiation from 230 to 2600 nm.
- Continuous 980 nm Laser diode is mainly used as excitation source for upconversion PL measurement.
- nF900 Nanosecond Flashlamp is a thyratron triggered, all metal, pulsed flashlamp. And provide sub-nanosecond pulses over the VUV to NIR spectra range, 110-850 nm at repetition rates to 100 kHz.

- μF900 Microsecond Flashlamp is a pulsed xenon microsecond flashlamp producing short, typically a few *μ*s, high irradiance optical pulses at repetition rates up to 100 Hz. It can be an excitation source for luminescence decay measurement.

**Detectors:**

- Red sensitive Photomultiplier (PMT) is available spanning the range from 185 to 870 nm at -20 °C.
- NIR PMT operated at -80 °C can respond to the spectral range 300-1700 nm.

**Grating:**

- Type: Plane holographic or ruled grating
- Standard: 250/500 nm blaze, 1800 grooves/mm
- Resolution: 0.05-18 nm
- Wavelength Accuracy: 0.2 nm

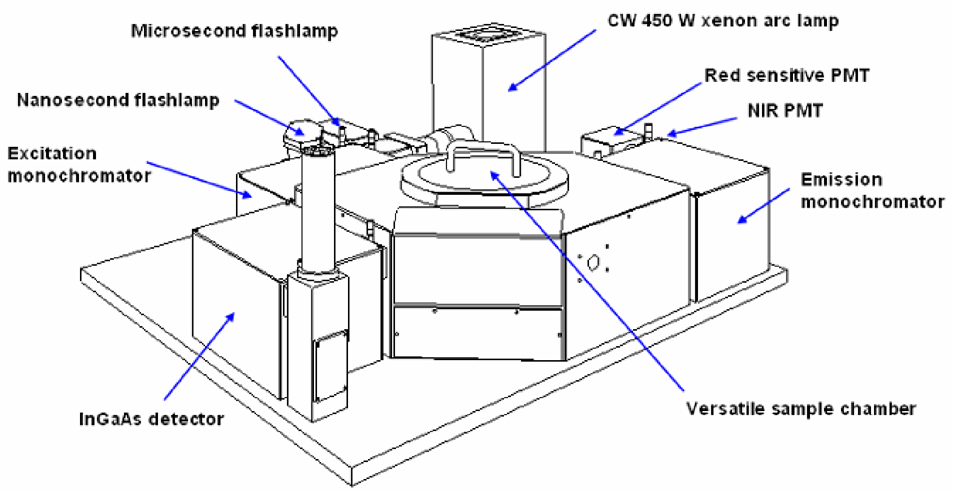

Figure 3.7. Schematic diagram of Edinburgh FLSP920 spectrometer used in our laboratory.

Time-resolved PL is widely used in the studies of physics, chemistry, and biology. Time-resolved measurements can provide more dynamic information than that is available from the steady-state PL. Luminescence decay kinetics give a complete picture of the phosphor and its interactions within the microenviroment. From this, the researcher can gain a deep understanding of the reaction mechanisms and electronic structure of the excited states of organic and inorganic molecules. For luminescence decay measurement, the sample is excited by a pulsed of light, the time-dependent intensity of PL is measured following the excitation pulse. The excitation sources include μF900 microsecond flashlamp, and picosecond pulsed semiconductor diode lasers EPL-series lasers. The monochromator and detectors used for time-resolved PL is the same as that of steady-state PL. Among time-resolved PL, fluorescence decay kinetics demonstrates a complete picture of the phosphor and its interactions within the microenvironment. An example of fluorescence decays measured using FLS920 is shown in Figure 3.8.

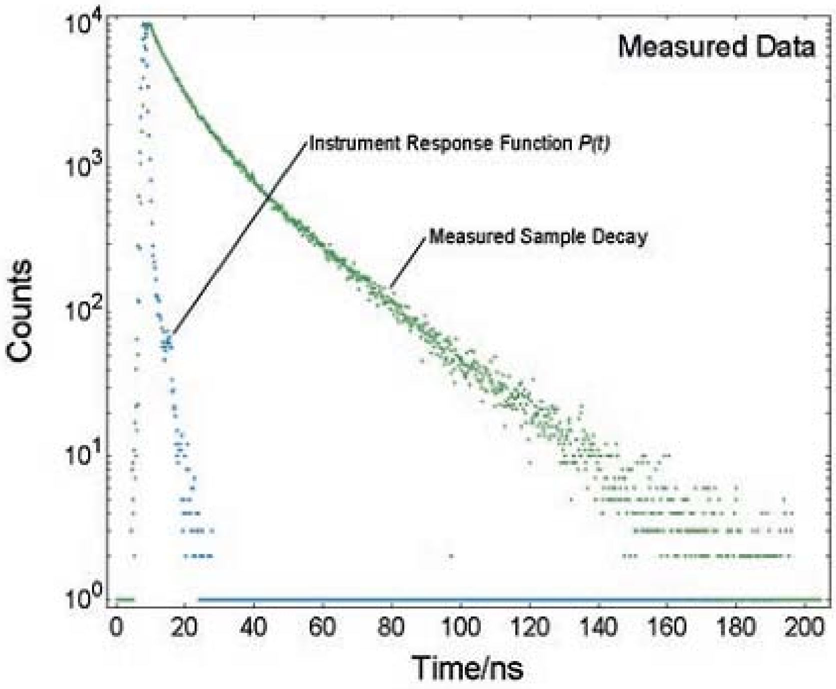

Figure 3.8. Sample of fluorescence decay curve.

The luminescence decay curve can be fitted into a sum of exponential terms as and by a constant background $A$,

$$I = A + \sum_i B_i \exp\{-\frac{t}{\tau_i}\} \tag{3.2}$$

and the average lifetime is determined,

$$\langle \tau \rangle = {\sum_i B_i \tau_i^2} \Big/ {\sum_i B_i \tau_i} \tag{3.3}$$

### 3.3.2 Raman Spectroscopy

Raman spectroscopy is one of the most widely used techniques in the physical and natural sciences. Raman scattering effect is discovered by C. V. Raman in 1921 [Raman, 1928]. The Raman Effect allows the observation of vibrational, rotational and other low-frequency spectra providing information of molecules in a system. The origin of Raman spectroscopy relies on the inelastic scattering effect. Typically, when a sample is illuminated, the elastic as well as the inelastic scattering of the sample is also observed. The elastic scattering is also called Rayleigh scattering, where the scattered photons have the same frequency as that of the incident radiation. As to the Raman radiation, it is related with the inelastic scattering, where the scattered photon is shifted in frequency compared to that the incident photon. Raman scattering involves transitions between the vibrational and rotation levels. The corresponding process is illustrated in Figure 3.9. The energy lost of the scattered photons is called the Raman shift. For a Stokes, it is positive, while negative for an anti-Stokes process. Raman shift is typically expressed in wavenumbers as follow,

$$\bar{\nu}(cm^{-1}) = \left(\frac{1}{\lambda_0(nm)} - \frac{1}{\lambda_1(nm)}\right) \tag{3.4}$$

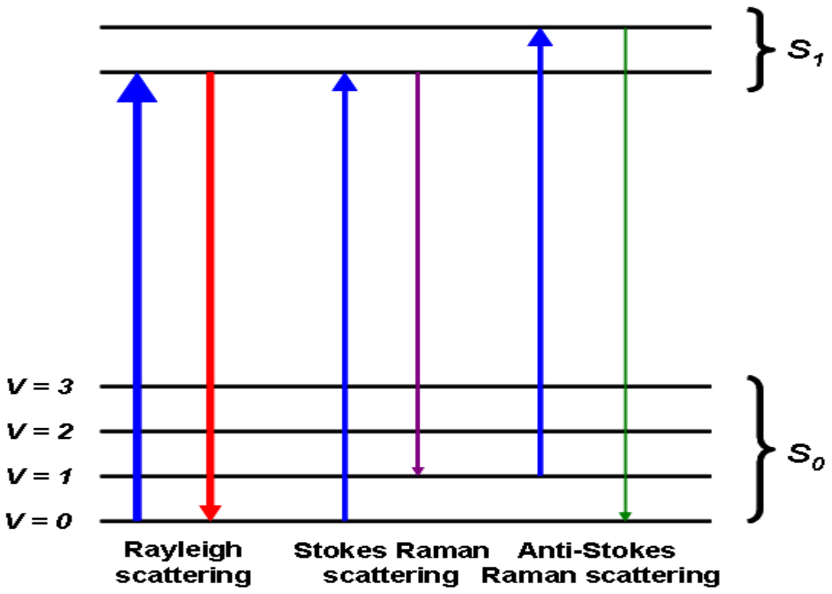

Figure 3.9. Simplified Jablonski diagram illustrating schematically the Rayleigh, Stokes, and anti-Stokes Raman scattering.

The Raman scattering process is typically very weak in comparison with the Rayleigh scattering. On the other hand, according to Boltzmann's distribution, at ambient temperature, molecules in their vibrational ground state are much more than that being in the vibrationally excited state. Therefore, The Anti-Stokes Raman scattering process has a much lower probability than the Stokes scattering. So, Raman spectroscopy is typically referred to the Stokes Raman scattering.

Compared with the widespread used fluorescence analysis technique, Raman spectroscopy has its advantages. The most attracting aspect of Raman spectroscopy is its high specificity, providing a unique fingerprint of the sample under study. Another attractive feature of Raman spectroscopy is that it has much more extended application scope. Raman spectroscopy can be applied any molecule, whereas fluorescence need there being fluorophore. Furthermore, Raman spectroscopy can be in principle excited under any excitation wavelength. An important difference between Raman spectroscopy and fluorescence is that Raman scattering process is instantaneous which means that Raman scattering can happen without a direct absorption of the photon, whereas this step is required for fluorescence. The main difficulty of Raman spectroscopy is the weakness of the Raman Effect. The discovery of the laser together with the development of sensitive detectors substantially improves the sensitivity of the Raman spectroscopy.

In this thesis, Raman spectra were measured using a Horiba Jobin Yvon LabRAM HR800 Raman spectrometer produced by Horiba Jobin Yvon with a 488 nm laser excitation source as shown in Figure 3.10. LabRAM HR 800 Raman spectrometer is a powerful optical instrument for material study and characterization.

- High spectral resolution (0.3 $cm^{-1}$ ~ 1 $cm^{-1}$);
- Large spectral range of Raman shift from 100 to 4000 $cm^{-1}$;
- Unique adjustable angle notch filter technology;
- Multiple laser wavelengths: UV, visible and near infra-red (NIR)

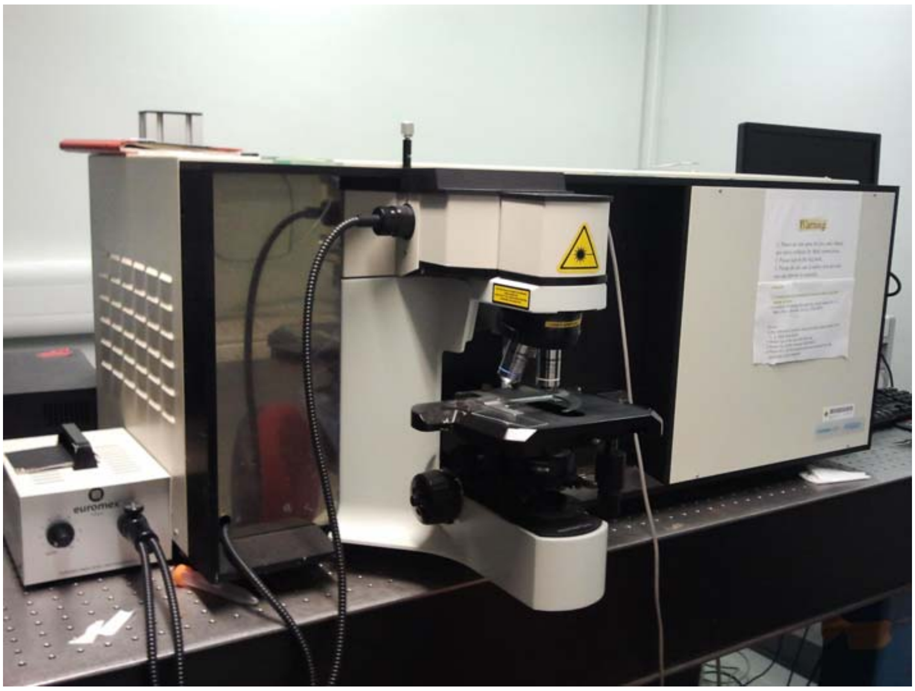

Figure 3.10. Picture showing the LabRAM HR 800 Raman spectrometer in our laboratory.

# Chapter 4 Luminescence of Rare-earth-doped $BaTiO_3$ Powders

## 4.1 Introduction

Rare-earth-doped ferroelectric materials have attracted much attention for their applications in microelectronics and optoelectronics. Ferroelectric titanates such as $SrTiO_3$ (STO) and $BaTiO_3$ (BTO) with typical perovskite $ABO_3$ structure have been extensively studied due to their excellent dielectric, ferroelectric, and electro-optic properties [Daniels, 2009; Tinte, 2001; Hao, 2005; Ganeev, 2008]. In the 1960s and 1970s, the interests in the rare-earth-doped perovskite-type oxides were mainly focused on the ferroelectricity, phase transitions and dielectric properties of these materials [Makishima, 1962; Makishima, 1965]. Trivalent lanthanide ions, such as $Er^{3+}$, $Tm^{3+}$, and $Eu^{3+}$, are common activator ions for luminescent phosphors. Among them, $Er^{3+}$ as an active ion has drawn broad attention to meet the request used for upconversion (UC) phosphors, planar waveguide and structure probe [Liu, 2009; Schlaghechen, 2004; Polman, 2001]. BTO doped with $Er^{3+}$ ion has been extensively investigated in ferroelectricity, phase transitions and luminescence. It is noted that the radius of the $Er^{3+}$ ion is intermediate between that of the $Ba^{2+}$ ion and $Ti^{4+}$ ion. $Er^{3+}$ ion can occupy either A- or B-site depending on Ba/Ti ratio [Takada, 1987; Dunbar, 2004]. Dopant site location was found to play an important role in electrical properties of $Er^{3+}$-doped BTO [Buscaglia, 2002; Mitic, 2010; Hwang, 2001]. It is well known that crystal field caused by structure symmetry of the host materials would contribute to different perturbation in terms of the $Er^{3+}$ inner shell transitions. Therefore, UC photoluminescence (PL) efficiency should be dependent on the excited-state dynamics of the $Er^{3+}$ ions and their interactions with the host matrix [Zhang, 2008; Wen, 2005b]. The interactions are strongly influenced by the host and the dopant. Unfortunately, there is very limited knowledge about the influence of site substitution of $Er^{3+}$-doped BTO on its PL properties. Furthermore, BTO is a typical ferroelectric material that undergoes successive phase transitions under different temperatures. UC mechanism of substituting sites corresponding to different symmetry structures has not been investigated yet.

Owing to the weak ground state absorption of 980 nm of $Er^{3+}$ ions, typically, the procedure of co-doping samples with $Yb^{3+}$ is frequently used for increasing the optical pump efficiency [Balakrishnaiah, 2009]. The high absorption cross-section of $Yb^{3+}$ ions around 980 nm ($^2F_{7/2} \rightarrow {}^2F_{5/2}$) is more than four times higher than that of $Er^{3+}$ ($^4I_{15/2} \rightarrow {}^4I_{11/2}$) [Camargo, 2005]. So, $Yb^{3+}$ is usually chosen as the sensitizer in upconversion phosphors because its large absorption cross section at 980 nm and the efficient energy transfer from $Yb^{3+}$ to other rare-earth ions which have a resonant electronic energy state [Guo, 2006; Oliveira, 1998]. Through appropriate combination, multicolour upconversion in the visible spectral region can be achieved. Previous results showed that $Yb^{3+}$, $Er^{3+}$, and $Tm^{3+}$ co-doped phosphors could exhibit controllable colors [Wang, 2008a; Zhang, 2011a]. By previous control of dopant concentration, the color output can be tunable from blue to white. $Eu^{3+}$ as one of mostly investigated rare-earth ions has an intense characteristic emission in the red light region. The structural, luminescent and magnetic properties of $Eu^{3+}$-doped SrTiO3 (STO) ceramics have been investigated [Jiang, 2009].

In this chapter, BTO doped with different rare-earth ions substituting positions and concentrations were prepared. X-ray diffraction (XRD) and Raman spectra were used to reveal the lattice distortion by doped rare-earth ions. The PL spectra of $Er^{3+}$-doped BTO and the UC mechanism related to the structure and cross-relaxation (CR) were studied. The PL spectra as a function of measuring temperature were investigated in order to understand the relationship between phase transition and luminescent behavior. The energy transfer and upconversion luminescence properties of BTO co-doped with $Yb^{3+}$ and $Er^{3+}$ ions were investigated. We demonstrated the tri-doped ($Yb^{3+}$, $Er^{3+}$, $Tm^{3+}$) BTO phosphor can emit different colors by variation of the dopant relative concentrations. The PL properties of $Eu^{3+}$-doped BTO phosphor have also been investigated,

## 4.2 Luminescence of $Er^{3+}$-doped BTO

### 5.2.1 Experiment

$Er^{3+}$-doped BTO powders with different site substitutions and concentrations were prepared by solid-state reaction method. Reagent grade $BaCO_3$, $TiO_2$, and

$Er_2O_3$ powders were used as raw materials. The charge compensation could be compensated by barium and oxygen vacancy for the A- and B-site substitutions, respectively. Here the samples for A- and B-site substitutions are refered to $Ba_{1-3x/2}Er_xTiO_3$ (BTO: A) and $BaTi_{1-x}Er_xO_{3-x/2}$ (BTO: B), respectively. Based on the above formulas, the starting powders with designed stoichiometric quantities were ball milled for 24 h, the dried and calcinated at 1100 °C for 8 h in air to generate the $Er^{3+}$-doped BTO powders.

The crystal structure of the samples was examined by a Bruker D8 Advanced X-ray diffractometer (XRD). Raman spectra were measured using a Horiba Jobin Yvon HR800 Raman spectrometer with a 488 nm laser excitation source. The PL spectra were recorded using an Edinburgh FLSP920 spectrophotometer under the excitation of a 980 nm laser diode. The fluorescence lifetime data for $Er^{3+}$ were recorded at 552 nm with a μF900H micro-second flashlamp ($\lambda_{ex}$ = 488 nm) as the excitation sources. The temperature-dependent PL spectra were carried out in the temperature range of 15-300 K.

### 5.2.2 Results and Discussion

Figure 4.1 shows the XRD patterns of $Er^{3+}$-doped BTO with different site substitutions and concentrations. The characteristic diffraction peaks of tetragonal BTO phase without secondary impurity phases were observed. The result implied that $Er^{3+}$ ions were doped efficiently into BTO host. A comparison of these XRD patterns with various $Er^{3+}$ doping shows the broaden diffraction peaks for samples with higher $Er^{3+}$ doping concentrations as shown in Figure 4.1. It suggests that the doping with higher $Er^{3+}$ concentrations may lead to the worse crystalline of doped BTO. In addition, compared with pure BTO, there are minor shifts of the diffraction peak (111) for the $Er^{3+}$ doped samples as seen in the inset of Figure 4.1. It means that the lattice constant of $Er^{3+}$-doped BTO shrinks or expands in the case of $Er^{3+}$ occupying A- or B-site, respectively [Jiang, 2009].

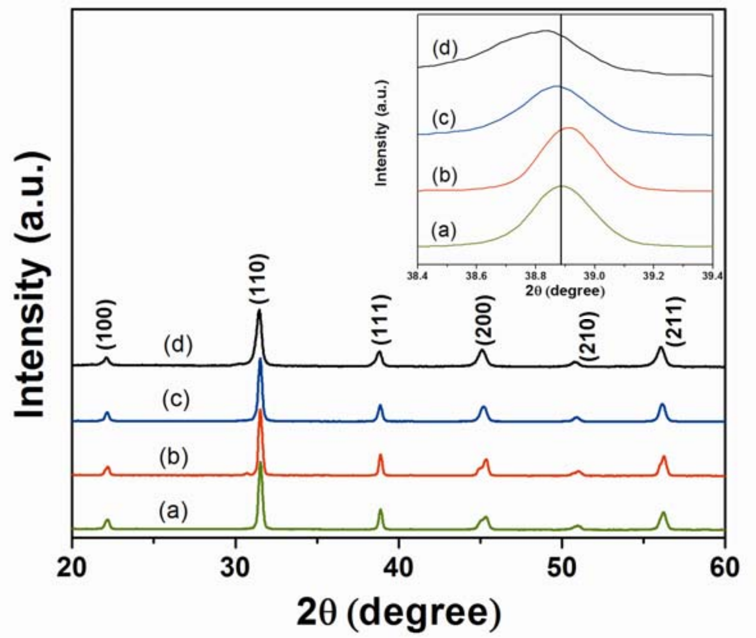

Figure 4.1. XRD patterns of the pure BTO and $Er^{3+}$-doped BTO with different site substitutions and concentrations: (a) pure, (b) x = 3 mol% with A-site substitution, (c) x = 3 mol% with B-site substitution and (d) x = 5 mol% with B-site substitution. The inset shows the enlarged (111) peak.

Figure 4.2 gives the Raman spectra of $Er^{3+}$-doped BTO and pure BTO at room temperature. BTO exhibits tetragonal structure belonging to the space group $C_{4v}$

symmetry. All of the features observed in the tetragonal phase have been reported in the literature [Dobal, 2002]. The peak observed at 305 $cm^{-1}$ corresponds to the $E(TO_2)$ phonon mode of tetragonal BTO. The $A_1(TO_1)$, $A_1(TO_2)$, $A_1(TO_3)$ and $A_1(LO_3)$ modes were observed at about 180, 270, 516 and 720 $cm^{-1}$, respectively. Raman spectra obtained from $Er^{3+}$-doped BTO did not show any remarkable wavelength shift. It can also be seen that all Raman modes become weaker and broader with an increase in $Er^{3+}$ concentration. It indicates that the higher $Er^{3+}$ concentration results in the worse crystallinity, which is consistent with the XRD results.

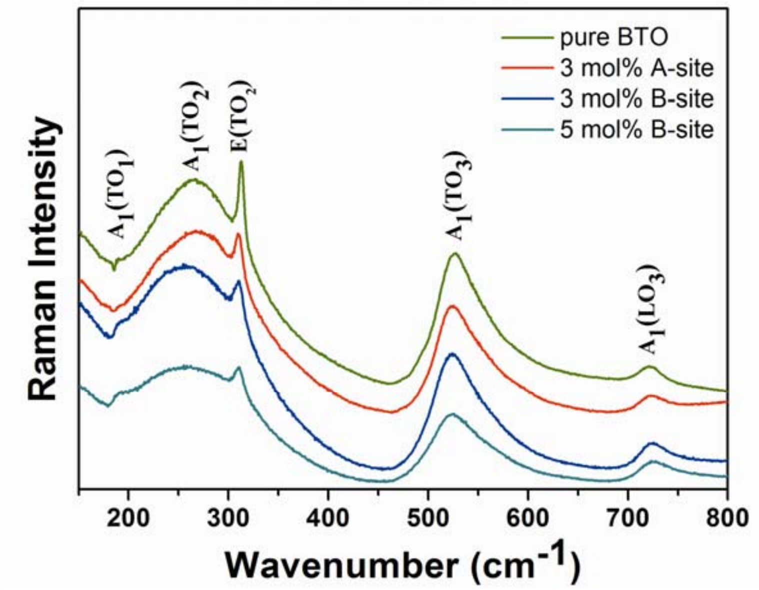

Figure 4.2. Raman spectra of the pure BTO and $Er^{3+}$-doped BTO with different site substitutions and concentrations.

Figure 4.3 shows the upconversion emission BTO doped with different $Er^{3+}$ ion concentrations and site substitutions measured at room temperature. The red (at 656 nm) and green (at 523/552 nm) emission bands correspond to the intra 4f-4f electronic transitions $^4F_{9/2} \rightarrow {}^4I_{15/2}$ and $^2H_{11/2}/^4S_{3/2} \rightarrow {}^4I_{15/2}$ of the $Er^{3+}$ ion, respectively. Obvious Stark-splitting can be observed in all samples [Huang, 2009]. Note that with an increase in $Er^{3+}$ doping concentration (0.5-5 mol% for BTO: B), the emission intensity reaches a maximum value at 1 mol%, and then deceases with an increase in doping concentration. There are two reasons responsible for this observation. Structural analysis based on XRD and Raman spectra has revealed that worse crystalline occurs in BTO: Er with increasing $Er^{3+}$ content. Worse crystalline phase corresponds to higher defect density of the materials. Both subband gap defect levels and impurity atoms in the grain boundaries could participate in the relaxation process and change the probability of radiative recombination [Hao, 2001; Wang, 2008b]. On the other hand, an increased dopant concentration could also enhance CR process with remarkable decrease UC emission as shown in Figure 4.5. Under the excitation of 980 nm, through excited state absorption (ESA) or energy transfer (ET) process, $Er^{3+}$ ion can populates the $^4F_{7/2}$ level. Subsequently, the $Er^{3+}$ ion then relaxes nonradiatively to the $^2H_{11/2}$ and $^4S_{3/2}$ levels by multiphonon relaxation, from which the green emissions ($^2H_{11/2}/^4S_{3/2} \rightarrow {}^4I_{15/2}$) occur. As shown in Figure 4.3, red UC emissions from the $^4F_{9/2}$ state are weak, since the $^4F_{9/2}$ state has a relatively large energy separation below the $^4S_{3/2}$ state, compared with the phonon energy of the BTO lattice.

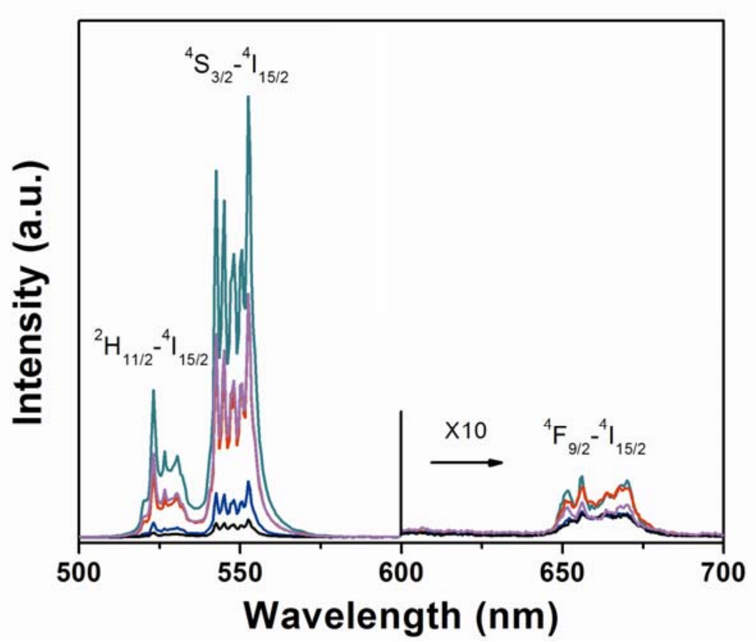

Figure 4.3. The PL spectra of BTO: A with x = 3 mol% (red) and BTO: B with x = 0.5 mol% (magenta), 1 mol% (cyan), 3 mol% (blue) and 5 mol% (black).

Moreover, we calculated the intensity of green-to-red ratio ($I_{523nm}/I_{656nm}$) for the BTO: B sample as shown in Figure 4.4. It can be seen that the ratio ($I_{523nm}/I_{656nm}$) is 23.4, 24.2, 5.7, and 1.8 for 0.5, 1, 3, and 5 mol% B-site $Er^{3+}$-doped BTO, respectively. The result can be understood based on the CR process shown in Figure 4.5. Higher $Er^{3+}$ concentration contributing to a shorter distance between ions results in an enhanced ET probability of the CR process, i.e. $^2H_{11/2} + {}^4I_{15/2} \rightarrow {}^4I_{9/2} + {}^4I_{13/2}$. Hence, the $Er^{3+}$ ions at the $^4I_{13/2}$ state through ESA populate the $^4F_{9/2}$ state. This enhanced population of the $^4F_{9/2}$ state primarily enhances the intensity of the red emission.

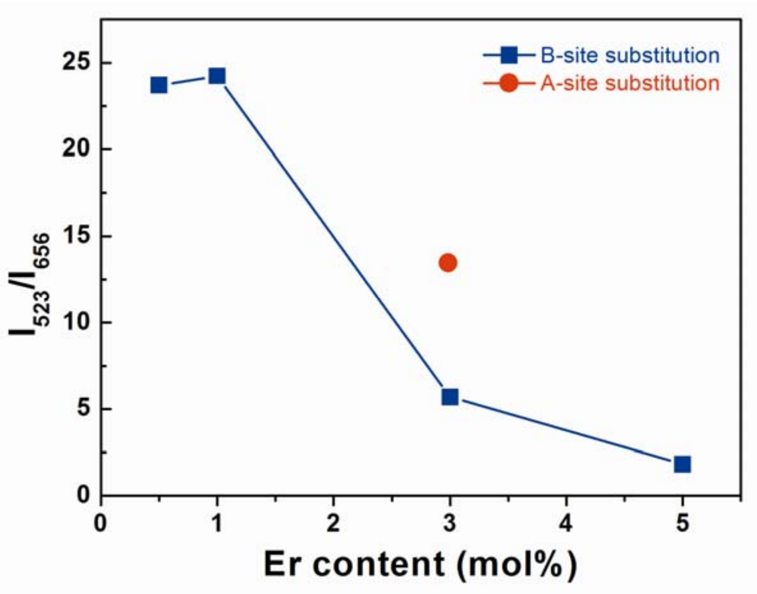

Figure 4.4. The intensity of green-to-red ratio ($I_{523nm}/I_{656nm}$) for BTO: A with x = 3 mol% (red) and BTO: B with x = 0.5, 1, 3, and 5 mol%.

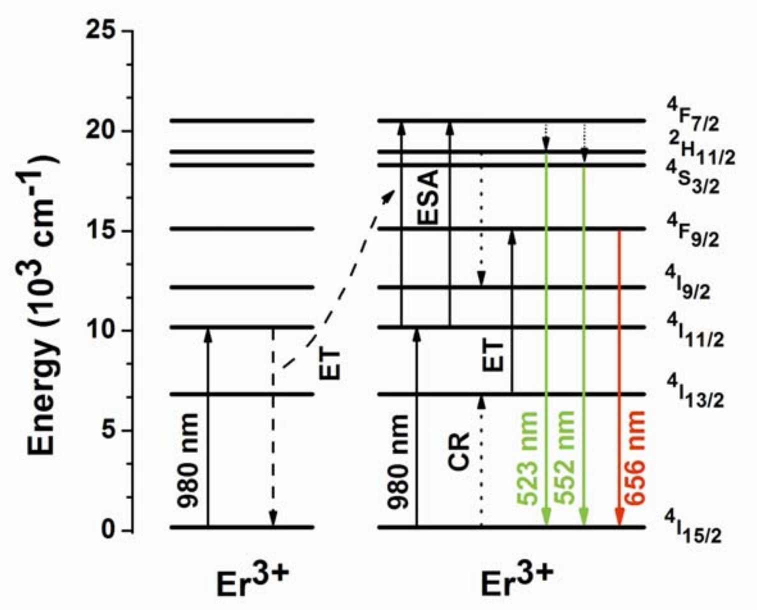

Figure 4.5. Schematic diagram for the UC mechanism of $Er^{3+}$ ions under 980 nm laser excitation.

The PL spectra of BTO with 3 mol% $Er^{3+}$ ion doped for A- and B-site substitutions are also presented in Figure. 4.3. The PL intensity differs for different site substitutions, but there is no obvious shift of the emission peaks. These results indicate that the crystal field surrounding $Er^{3+}$ ions can change the relative radiative probability of the transitions from the excited state to the eight Stark components of the $^4I_{15/2}$ ground state. The PL intensity of A-site doped sample is much stronger than that of B-site doped BTO. Compared with that of A-site doped sample, the decrease in PL intensity for B-site substitution $Er^{3+}$-doped BTO may be affected by oxygen vacancies when $Er^{3+}$ ion as an acceptor type impurity replace Ti site, leading to an oxygen-deficient nonstoichiometry [Hwang, 2001; Jiang, 2009]. Compared the fluorescence lifetimes for two samples at 552 nm corresponding to $^4S_{3/2} \rightarrow {}^4I_{15/2}$ transition, the double exponential fitting results for A- and B-site doped samples are 132 and 52 $\mu$s, respectively. The decrease of lifetime of B-site substituted sample could be ascribed to the introduction of oxygen vacancies. We speculate that these oxygen vacancies would induce new energy levels, which promote nonradiative energy transfer.

It is well-known that BTO undergoes successive phase transitions. PL evolution of the samples has been evaluated as a function of temperatures between 15 and 300 K. It shows that the PL response of $Er^{3+}$ ions to the structural changes occurring during phase transition is related to their site location in the BTO host. Figure 4.6 shows the temperature dependence of the PL intensity for the case of A-site substitution.

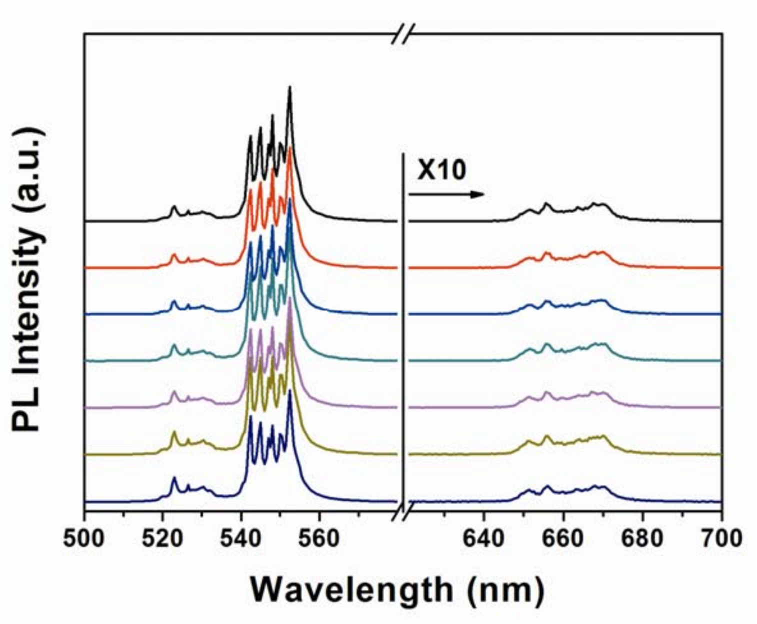

Figure 4.6. The PL spectra of $Er^{3+}$-doped BTO (x = 3 mol%) for A-site substitution at different temperatures 15 K (black), 50 K (red), 100 K (blue), 150 K (cyan), 183 K (magenta), 250 K (yellow) and 300 K (navy).

It is known that pure BTO crystal undergoes ferroelectric phase transitions at 278 and 183 K. Rare-earth doping has slight influence on the phase transition temperature of BTO [Na, 2003]. As presented in Figure 4.7, the abnormal jump in PL intensity of $Er^{3+}$-doped BTO (x = 3 mol%) for A-site substitution across the vicinity of 150 K and 250 K may be related to the crystal field changes around $Er^{3+}$ ions induced by the phase transition.

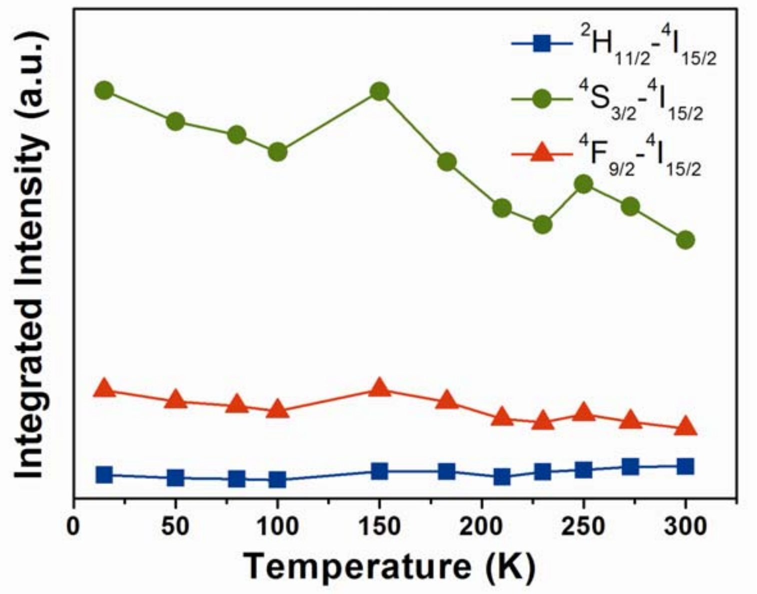

Figure 4.7. The corresponding integrated intensity of three emission bands at different temperatures for A-site substitution $Er^{3+}$-doped BTO (x = 3 mol%).

For the B-site substitution, the UC emission from $^2H_{11/2}$ is strongly suppressed, while the emission from $^4S_{3/2}$ increases remarkably as shown in Figure 4.8. The $^2H_{11/2}$ state is thermally quenched to $^4S_{3/2}$ state and subsequently contributed to the enhanced population of $^4S_{3/2}$ state with decreasing temperature. Apart from the thermal quenching, the phenomenon is also relative to the crystal field. The crystal field formed by the octahedral oxygen ions with a lower symmetry than $O_h$ is more suitable for the Er intra-4f transitions [Ishii, 2001; Zhou, 2005]. Therefore, $Er^{3+}$ located B-site with lower symmetry due to phase transition facilitates the UC emissions.

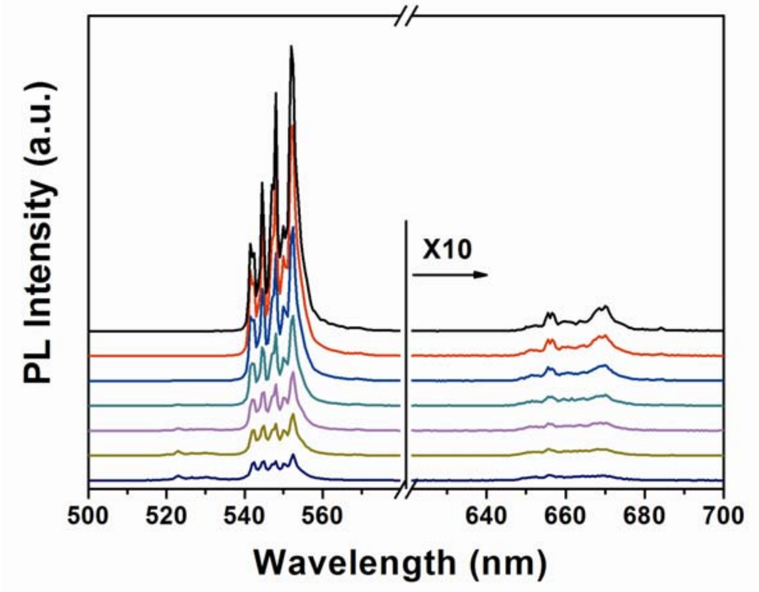

Figure 4.8. The PL spectra of $Er^{3+}$-doped BTO (x = 3 mol%) for B-site substitution at different temperatures 15 K (black), 50 K (red), 100 K (blue), 150 K (cyan), 183 K (magenta), 250 K (yellow) and 300 K (navy).

An increase in red emission $^4F_{9/2} \rightarrow {}^4I_{15/2}$ with lower symmetry for B-site substitution $Er^{3+}$-doped BTO occurs as evidenced in Figure 4.9. The characteristics imply that the emission from substituted $Er^{3+}$ ions can be used as a structural probe for the BTO.

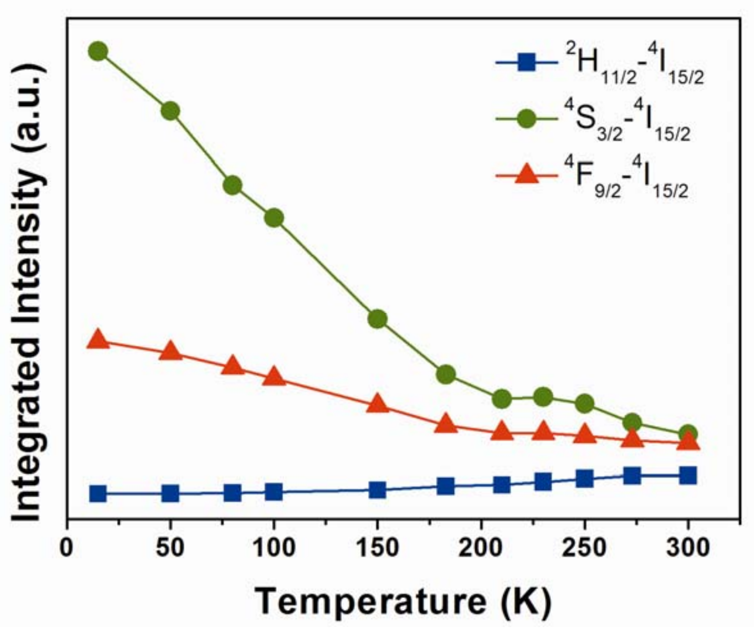

Figure 4.9. The corresponding integrated intensity of three emission bands at different temperatures for B-site substitution $Er^{3+}$-doped BTO (x = 3 mol%).

## 4.3 Upconversion Luminescence in $Yb^{3+}$/$Er^{3+}$ co-doped BTO Powders

### 4.3.1 Experiment

$Yb^{3+}$/$Er^{3+}$ co-doped BTO powder phosphors were synthesized by conventional solid-state reaction method. Reagent grade $BaCO_3$, $TiO_2$, $Yb_2O_3$ and $Er_2O_3$ powders were used as raw materials. $Er^{3+}$ and $Yb^{3+}$ were substituted at the $Ti^{4+}$ sites, the negative effective charge could be compensated by oxygen vacancy. The sum of $Er^{3+}$ and $Yb^{3+}$ ions concentration used in the BTO phosphor is fixed at 0.5 mol% and 2.5

mol%, respectively. Thus the formula could be given by $BaTi_{0.97}Er_{0.005}Yb_{0.025}O_{3-\delta}$ (BTO:Yb/Er) Based on the above formula, the starting powders with designed stoichiometric quantities were ball milled for 24 h, the dried and calcinated at 1100 °C for 8 h in air to generate the BTO:Yb/Er powders.

The crystal structure of the samples was examined by XRD, Raman spectra. The upconversion emission spectra were measured using the 980 nm excitation wavelength.

### 4.3.2 Results and Discussion

Figure 4.10 shows the XRD patterns of the BTO:Yb/Er powders. Only the characteristic diffraction peaks of tetragonal BTO phase can be observed from the XRD patterns, suggesting that $Yb^{3+}$ and $Er^{3+}$ ions were doped efficiently into the BTO host. Compared with the XRD pattern of pure BTO, it suggests that there are minor shifts of the diffraction peaks for the sample with the doping with $Yb^{3+}$ and $Er^{3+}$ ions as shown in the Figure 4.10. It means that the lattice constant of BTO:Yb/Er powders expands, this result is similar to the case of single $Er^{3+}$ occupying B-site of BTO which we have discussed before.

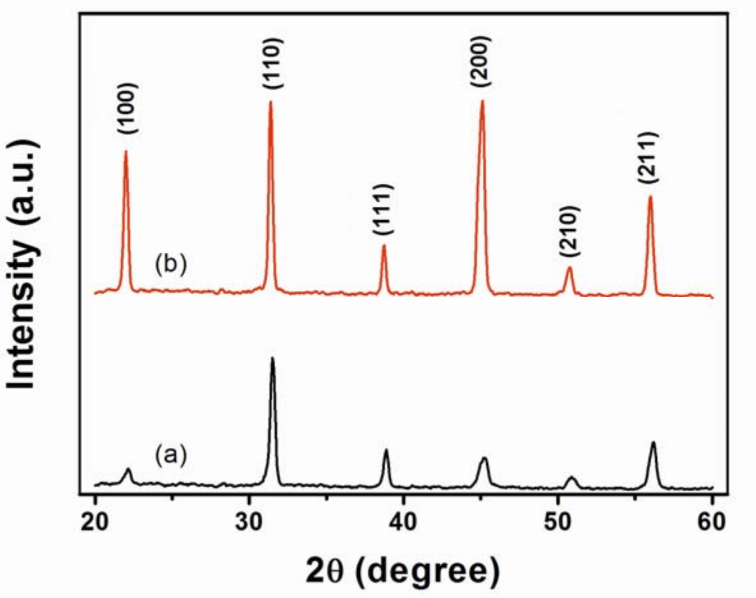

Figure 4.10. XRD patterns of the pure BTO (a black line) and BTO:Yb/Er (b red line).

Figure 4.11 gives the Raman scattering spectra of BTO:Yb/Er powders at room temperature. BTO exhibits tetragonal structure belonging to the space group $C_{4v}$ symmetry. The weak shoulder observed at 305 cm$^{-1}$ belongs to the E(TO$_2$) phonon mode of tetragonal BTO. The A$_1$(TO$_1$) mode and A$_1$(TO$_2$) mode were observed at about 180 and 270 cm$^{-1}$, respectively. A asymmetric A$_1$(TO$_3$) appeared at about 516 cm$^{-1}$. And the A$_1$(LO$_3$) modes appeared at 720 cm$^{-1}$ in tetragonal BTO.

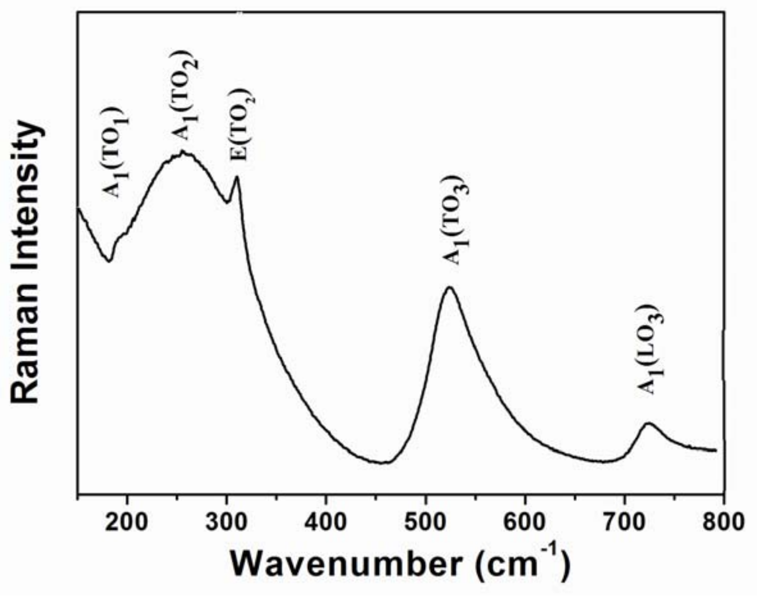

Figure 4.11. Raman spectra of the BTO:Yb/Er powders.

The emission spectra of BTO:Yb/Er under infrared excitation (~980 nm) at room temperature are presented in Figure 4.12. Two intense green emission bands at 523 and 550 nm are attributed to the $^2H_{11/2} \rightarrow {}^4I_{15/2}$ and $^4S_{3/2} \rightarrow {}^4I_{15/2}$ transitions of $Er^{3+}$ ions while a red emission corresponds to the $^4F_{9/2} \rightarrow {}^4I_{15/2}$ transition of $Er^{3+}$ ions. It is noted that the red emission of BTO:Yb/Er is much stronger than that of single $Er^{3+}$-doped BTO. To better understand the upconversion mechanism, the pump power dependence of the upconversion emission was investigated. For the upconversion process, the number of photons which are required to populate the upper emitting state can be obtained by the following relation [Chen, 2007]:

$$I \propto P^n \tag{4.1}$$

where $I$ is the emission intensity, $P$ is the pump power, and $n$ is the number of photons required [Bai, 2007; Sun, 2006]. A plot of ln $I$ versus ln $P$ yields a straight line with slope *n*. The results for the $^2H_{11/2}/^4S_{3/2} \rightarrow {}^4I_{15/2}$ green emission and $^4F_{9/2} \rightarrow {}^4I_{15/2}$ red emission of $Er^{3+}$ ion are shown in Figure 4.13. The calculated slopes n are 1.55 and 1.36 for green ($^2H_{11/2}/^4S_{3/2} \rightarrow {}^4I_{15/2}$) and red ($^4F_{9/2} \rightarrow {}^4I_{15/2}$) emissions, respectively. The result indicates that the upconversion mechanism corresponding to both green and red emissions where a two-photon process is involved. However, the smaller slope *n* of the red emission suggests that a one-photon process is needed to excite the electrons to the $^4F_{9/2}$ state of $Er^{3+}$ ion where red emission arises. The decrease in the slope of upconversion intensity versus pump power with increasing power can be explained well by the saturation process.

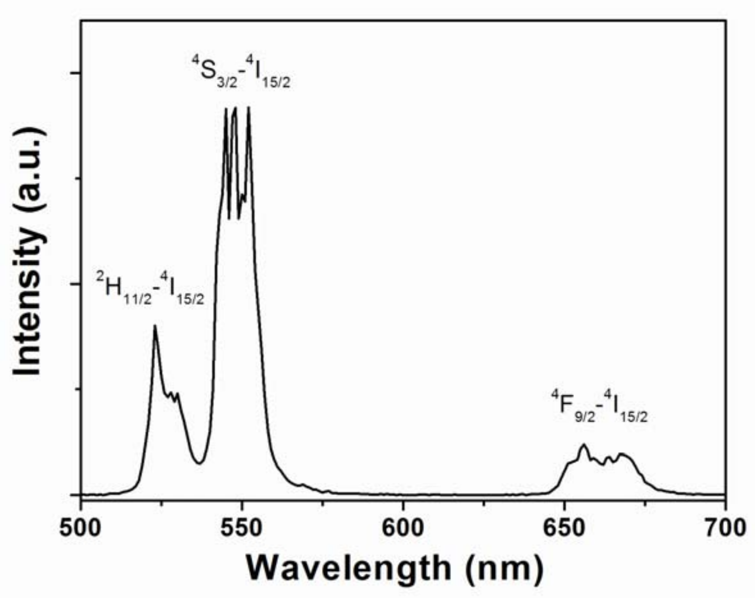

Figure 4.12. Upconversion emission spectra of $Yb^{3+}/Er^{3+}$ co-doped BTO under 980 nm laser excitation.

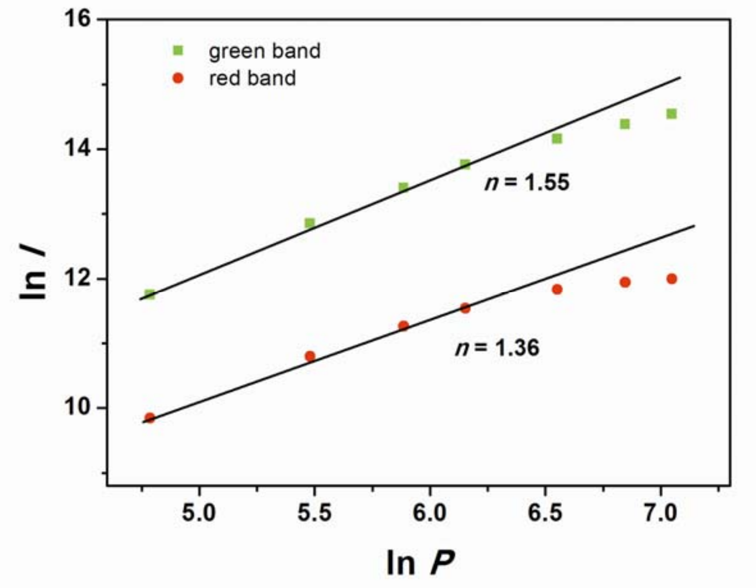

Figure 4.13. Pump power dependence of the green and red emission of $Yb^{3+}/Er^{3+}$ co-doped BTO under 980 nm laser excitation.

The upconversion mechanism in $Yb^{3+}$ and $Er^{3+}$ co-doped phosphors has been well investigated. Figure 4.14 shows the energy level diagrams of the $Er^{3+}$ and the $Yb^{3+}$ ions, as well as the upconversion processes under 980 nm laser excitation. An $Yb^{3+}$ ion in ground state $^2F_{7/2}$ absorbs a 980 nm photon and jumps to excited state $^2F_{5/2}$, and then drops back to the ground state while transfers the energy to neighboring $Er^{3+}$ ion. The $Er^{3+}$ ion is populated to the $^4I_{11/2}$ level from the ground state $^4I_{15/2}$. Then, a second 980 nm photon, or energy transfer from the $Yb^{3+}$ ion, can populate the $^4F_{7/2}$ level of the $Er^{3+}$ ion. The $Er^{3+}$ ion can relax nanradiatively to the $^2H_{11/2}$ and $^4S_{3/2}$ levels, and the green emissions $^2H_{11/2}/^4S_{3/2} \rightarrow {}^4I_{15/2}$ occur. Alternatively, the $Er^{3+}$ ion can further relax to the $^4F_{9/2}$ level of the $Er^{3+}$ ion, leading to the red emission $^4F_{9/2} \rightarrow {}^4I_{15/2}$. So both the green and red emissions are related with a two-photon process. Compared with $Er^{3+}$-doped BTO, red upconversion emission from $Yb^{3+}/Er^{3+}$ co-doped BTO is much larger. The energy separation between the $^4F_{9/2}$ and $^4S_{3/2}$ states is relatively large compared with the phonon energy of BTO lattice. As shown in Figure 4.14, the $Er^{3+}$ ion in the $^4I_{11/2}$ state may nonradiatively decay to the $^4I_{13/2}$ state and then populate the $^4F_{9/2}$ level via a one photon process by energy transfer from $Yb^{3+}$ to the $Er^{3+}$ ion. This is the reason for $Yb^{3+}/Er^{3+}$ co-doped BTO has larger red emission than that of $Er^{3+}$-doped BTO.

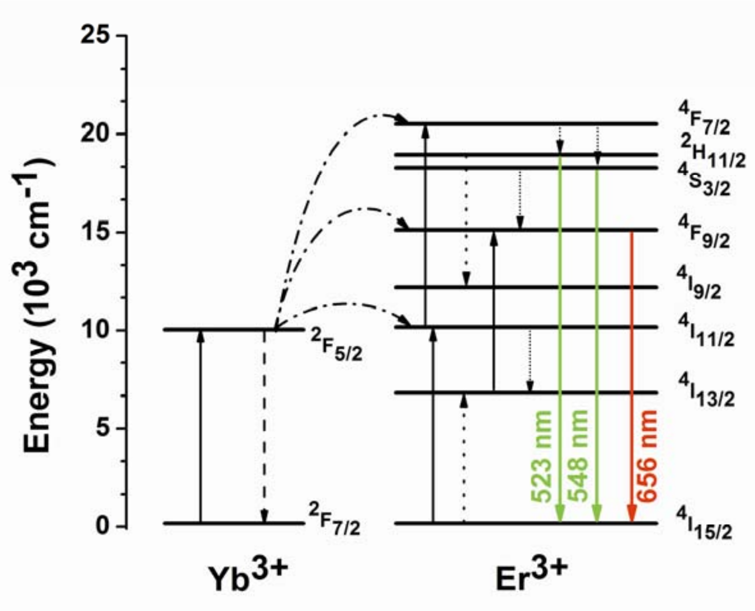

Figure 4.14. Energy level diagram of $Er^{3+}$ and $Yb^{3+}$ ions as well as the relevant upconversion process in $Yb^{3+}/Er^{3+}$ co-doped BTO under 980 nm laser excitation. The dashed-dotted, dashed, and dotted lines represent energy transfer, multiphonon relaxation, and cross-relaxation, respectively.

## 4.4 Upconversion Luminescence in $Yb^{3+}/Er^{3+}/Tm^{3+}$ tri-doped BTO Powders

### 4.4.1 Experiment

$Yb^{3+}/Er^{3+}/Tm^{3+}$ tri-doped BTO powder phosphors were synthesized by conventional solid-state reaction method. Reagent grade $BaCO_3$, $TiO_2$, $Yb_2O_3$, $Er_2O_3$ and $Tm_2O_3$ powders were used as raw materials. $Yb^{3+}$, $Er^{3+}$, and $Tm^{3+}$ were substituted at the $Ti^{4+}$ sites, the negative effective charge could be compensated by oxygen vacancy. Thus the formula could be given by $BaTi_{1-x-y-z}Yb_xEr_yTm_zO_{3-\delta}$ (BTO: $xYb^{3+}$, $yEr^{3+}$, $zTm^{3+}$, in which x, y, and z are the doping concentrations in molar percentage). Based on the above formula, the starting powders with designed stoichiometric quantities were ball milled for 24 h, the dried and calcinated at 1100 °C for 8 h in air to generate the $Yb^{3+}/Er^{3+}/Tm^{3+}$ tri-doped BTO powders.

The crystal structure of the samples was examined by XRD. The upconversion emission spectra were measured using the 980 nm excitation wavelength.

### 4.4.2 Results and Discussion

Figure 4.15 shows the XRD patterns of BTO: $2\%Yb^{3+}$, $0.2\%Tm^{3+}$ (a line), BTO: $2\%Yb^{3+}$, $0.02\%Er^{3+}$, $0.2\%Tm^{3+}$ (b line), and BTO: $2\%Yb^{3+}$, $0.2\%Er^{3+}$, $0.2\%Tm^{3+}$ (c line) samples, respectively. Only the characteristic diffraction peaks of tetragonal

BTO phase without secondary impurity phases can be observed from the XRD patterns, suggesting that $Yb^{3+}$, $Er^{3+}$, and $Tm^{3+}$ ions were doped efficiently into the BTO host lattice.

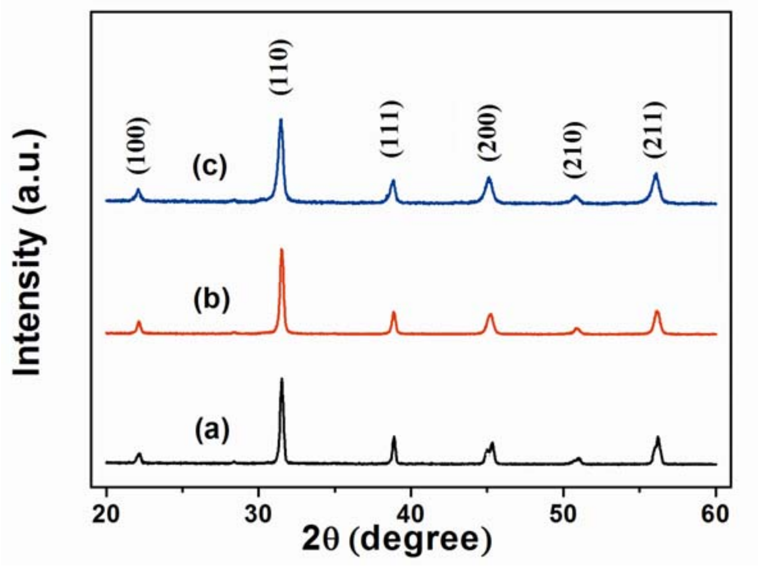

Figure 4.15. XRD patterns of BTO: $xYb^{3+}$, $yEr^{3+}$, $zTm^{3+}$ powders. (a) BTO: 2%$Yb^{3+}$, 0.2$Tm^{3+}$, (b) BTO: 2%$Yb^{3+}$, 0.02%$Er^{3+}$, 0.2%$Tm^{3+}$, and (c) BTO: 5%$Yb^{3+}$, 0.2%$Er^{3+}$, 0.2%$Tm^{3+}$.

Figure 4.16 shows the upconversion luminescence spectra of tri-doped BTO phosphors under 980 nm laser excitation. Figure 4.16a shows the upconversion emission spectrum of the BTO: 2%$Yb^{3+}$, 0.2$Tm^{3+}$ sample excited at 980 nm. The blue emission centered at about 464 and 478 nm, which can be attributed to the $^1D_2 \rightarrow {}^3F_4$ and $^1G_4 \rightarrow {}^3H_6$ transitions of $Tm^{3+}$ ion, respectively. The upconversion emissions appeared in the region (630-710 nm) corresponding to the $^1G_4 \rightarrow {}^3F_4$, $^3F_2/^3F_3 \rightarrow {}^3H_6$ transitions of $Tm^{3+}$ ion. In Figures 4.16 b and c, it can be seen that the upconversion spectra of BTO: 2%Yb$^{3+}$, 0.02%Er$^{3+}$, 0.2%Tm$^{3+}$ (b) and BTO: 5%Yb$^{3+}$, 0.2%Er$^{3+}$, 0.2%Tm$^{3+}$ (c) samples embrace blue emission at 464 and 478 nm assigned to the $^1D_2 \rightarrow {}^3F_4$ and $^1G_4 \rightarrow {}^3H_6$ transitions of Tm$^{3+}$ ion. Green emission at 523 and 550 nm due to the $^2H_{11/2}/^4S_{3/2} \rightarrow {}^4I_{15/2}$ transitions of Er$^{3+}$ ion, and red emission in the region (630-710 nm) can be arising from the $^4F_{9/2} \rightarrow {}^4I_{15/2}$ transition of the Er$^{3+}$ ion, as well as the $^3F_2/^3F_3 \rightarrow {}^3H_6$ transitions of Tm$^{3+}$ ion, respectively.

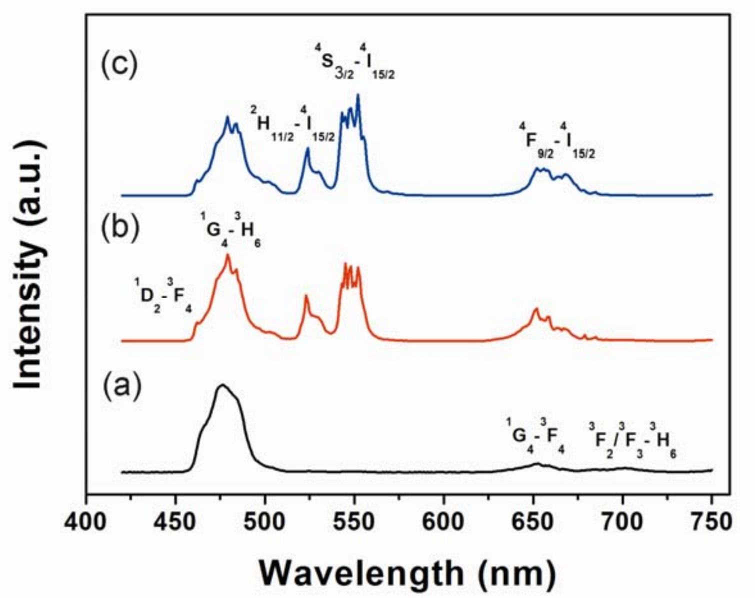

Figure 4.16. Upconversion emission spectra of Yb$^{3+}$, Er$^{3+}$, Tm$^{3+}$ tri-doped BTO under 980 nm laser excitation. (a) BTO: 2%Yb$^{3+}$, 0.2Tm$^{3+}$, (b) BTO: 2%Yb$^{3+}$, 0.02%Er$^{3+}$, 0.2%Tm$^{3+}$, and (c) BTO: 5%Yb$^{3+}$, 0.2%Er$^{3+}$, 0.2%Tm$^{3+}$.

Figure 4.17 is the schematic energy levels diagrams of Yb$^{3+}$, Er$^{3+}$, and Tm$^{3+}$ ions, as well as the proposed upconversion processes under 980 nm laser excitation. The upconversion emission mechanism for the Yb$^{3+}$ and Er$^{3+}$ co-doped system has been discussed in detail in chapter 4.2. As shown in Figure 4.17, an effective energy transfer occurs from the $Yb^{3+}$ ion to $Er^{3+}$, and $Tm^{3+}$ ions. For the $Yb^{3+}$ and $Tm^{3+}$ co-doped system, the blue emission ($^1G_4 \rightarrow {}^3H_6$) of $Tm^{3+}$ is a three-photon process. Under 980 nm laser excitation, nonresonant energy transfer arises from population of the $^2F_{5/2}$ level of $Yb^{3+}$ to the $^3H_5$ level of $Tm^{3+}$ ion. Subsequently, the $Tm^{3+}$ ion relaxes rapidly to the $^3F_4$ level by multiphonon processes. A second 980 nm photon can populate the $Tm^{3+}$ ion to the $^3F_2$ state. And subsequently nonradiative relaxation results in the population of the $^3H_4$ level. Meanwhile, the red emission also arises from $^3F_2$ state. A third 980 nm photon populates the $^1G_4$ level. Then, a strong blue emission state ($^1G_4 \rightarrow {}^3H_6$) and a weak red emissions (($^1G_4 \rightarrow {}^3F_4$) occur. A weak blue emission at 464 nm through four-photon process arises from $^1D_2 \rightarrow {}^3H_6$ transition.

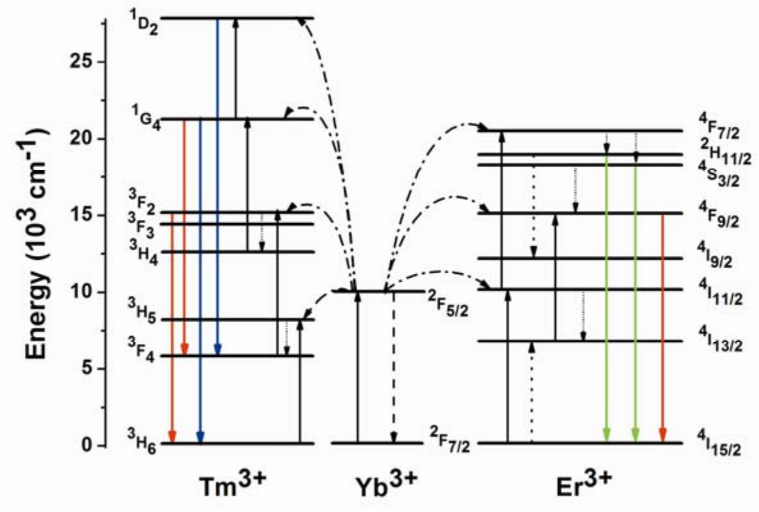

Figure 4.17. Energy level diagram of $Er^{3+}$, $Tm^{3+}$, and $Yb^{3+}$ ions as well as the relevant upconversion process in $Yb^{3+}$/ $Er^{3+}$/$Tm^{3+}$ tri-doped BTO under 980 nm excitation. The dashed-dotted, dashed, and dotted lines represent energy transfer, multiphonon relaxation, and cross-relaxation, respectively.

By precise control of dopant concentration, the relative intensities of RGB colors can be modulated. According to the 1931 commission International de l'Eclairage (CIE) coordinates of color, the calculated CIE chromaticity coordinates (*x*, *y*) of the as-synthesized rare-earth doped BTO phosphors under 980 nm laser excitation are summarized in Table 4.1.

Table 4.1 Chromaticity coordinates (*x*, *y*) of the rare-earth doped BTO phosphors under 980 nm laser excitation.

| Phosphor | Chromaticity coordinate (*x*) | Chromaticity coordinate (*y*) |
|---|---|---|
| BTO:0.5%Er, 2.5%Yb | 0.33 | 0.65 |
| BTO:2%Yb, 0.2%Tm | 0.13 | 0.14 |
| BTO:2%Yb, 0.02%Er, 0.2%Tm | 0.21 | 0.41 |
| BTO:5%Yb, 0.5%Er, 0.5%Tm | 0.23 | 0.51 |
| BTO:2%Yb, 0.1%Er, 0.2%Tm | 0.24 | 0.55 |

Obviously, the chromaticity coordinates (*x, y*) can be changed by control of the dopant concentrations. The calculated CTE coordinates are plotted in Figure 4.18. It is clear that the CIE coordinates are highly dependent on the dopant and their concentrations.

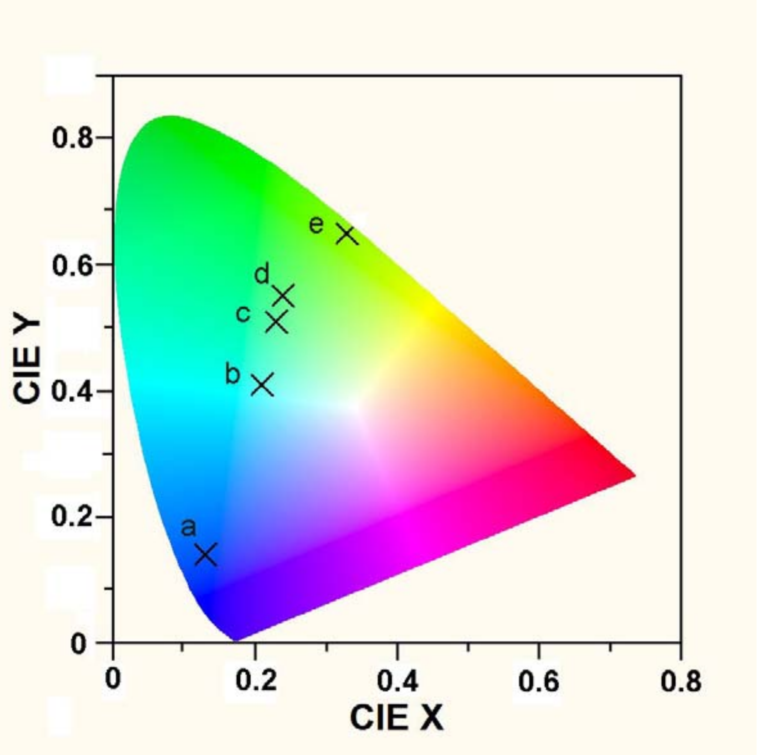

Figure 4.18. CIE chromaticity diagrams of BTO: $xYb^{3+}$, $yEr^{3+}$, $zTm^{3+}$ powders. (a) BTO: 2%$Yb^{3+}$, 0.2$Tm^{3+}$, (b) BTO: 2%$Yb^{3+}$, 0.02%$Er^{3+}$, 0.2%$Tm^{3+}$, (c) BTO: 5%$Yb^{3+}$, 0.5%$Er^{3+}$, 0.5%$Tm^{3+}$, (d) BTO: 2%$Yb^{3+}$, 0.1%$Er^{3+}$, 0.2%$Tm^{3+}$, and (e) BTO: 2.5%$Yb^{3+}$, 0.5%$Er^{3+}$.

## 4.5 Luminescence of $Eu^{3+}$-doped BTO Powders

### 4.5.1 Experiment

$Eu^{3+}$-doped BTO powder phosphors were synthesized by conventional solid-state reaction method. Reagent grade $BaCO_3$, $TiO_2$, and $Eu_2O_3$ powders were used as raw materials. $Eu^{3+}$ was substituted at the $Ti^{4+}$ site, the negative effective charge could be compensated by oxygen vacancy. Thus the formula could be given by

$BaTi_{0.99}Eu_{0.01}O_{3-\delta}$ (BTO: Eu). Based on the above formula, the starting powders with designed stoichiometric quantities were ball milled for 24 h, the dried and calcinated at 1100 °C for 8 h in air to generate the $Eu^{3+}$-doped BTO powders.

The crystal structure of the samples was examined by a Bruker Advanced X-ray diffractometer. The PL spectra were measured using an Edinburgh FLSP 920 spectrophotomter. A Xe lamp was used as the excitation source.

### 4.5.2 Results and Discussion

Figure 4.19 shows the XRD patterns of BTO: Eu. Only the characteristic diffraction peaks of tetragonal BTO phase without secondary impurity phases can be observed from the XRD patterns, suggesting that $Eu^{3+}$ ions were doped efficiently into the BTO host lattice.

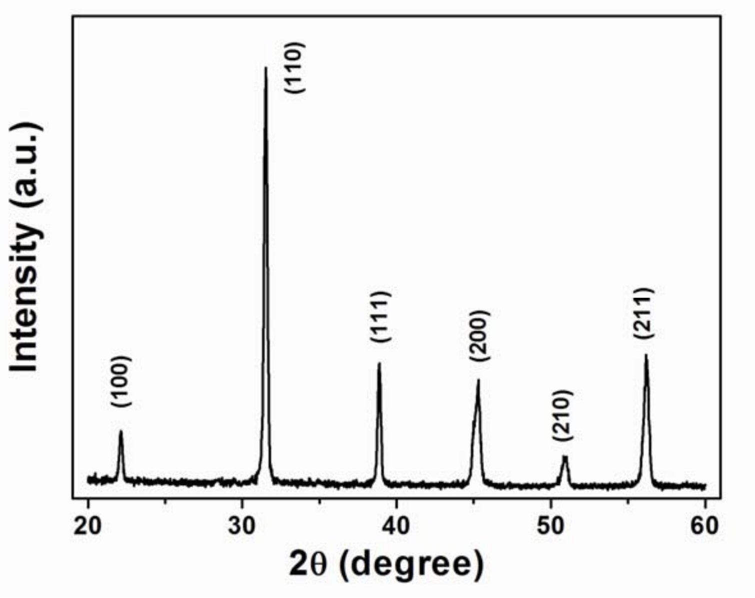

Figure 4.19. XRD patterns of BTO: Eu powders.

Figure 4.20 shows the room temperature PL spectra of the BTO: Eu phosphor under the excitation of 465 nm. The emission peaks at 579 and 652 nm, correspond to $^5D_0 \rightarrow {}^7F_0$ and $^5D_0 \rightarrow {}^7F_3$, respectively. Two other emission peaks at the positions of 593 and 614 nm contain more information, are attributed to $Eu^{3+}$ ion transitions of $^5D_0 \rightarrow {}^7F_1$ and $^5D_0 \rightarrow {}^7F_2$, respectively. When $Eu^{3+}$ ions exist in a symmetric center, the electric dipole transition $^5D_0 \rightarrow {}^7F_2$ is forbidden. The magnetic dipole transition $^5D_0 \rightarrow {}^7F_1$ hardly varies with the crystal field strength around the $Eu^{3+}$ ion [Feofilov, 2007; Peng, 2005]. In our results, the intensity of $^5D_0 \rightarrow {}^7F_2$ transition is stronger than that of $^5D_0 \rightarrow {}^7F_1$ transition, we can deduce that there is a non-symmetric crystal field around the $Eu^{3+}$ ion.

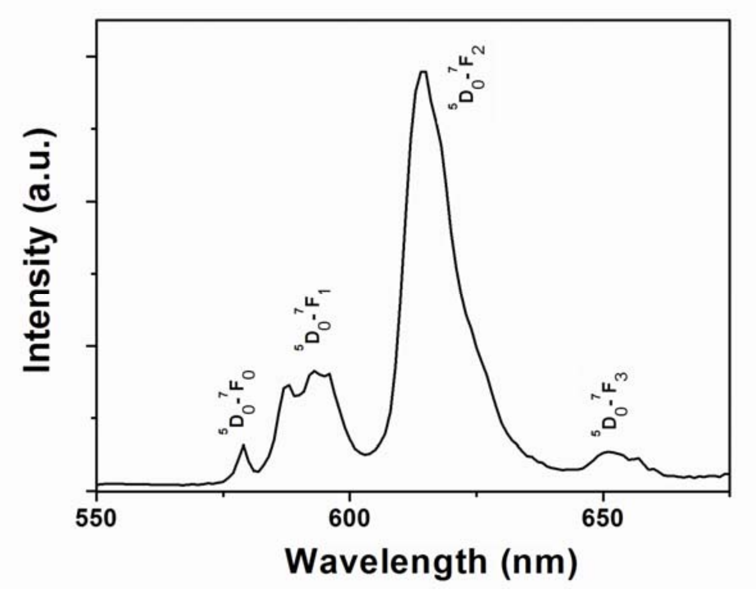

Figure 4.20. PL spectrum of BTO: Eu ($\lambda_{ex}$ = 465 nm).

## 4.6 Conclusion

In conclusion, BTO doped with different rare-earth ion substituting positions and concentrations were prepared by solid-state reaction method. PL quenching of $Er^{3+}$-doped BTO is due to the worse crystalline and cross-relaxation with an increasing in $Er^{3+}$ doping concentration. Phase transition results in the increase of PL spectra of A-site doped BTO across the phase transition temperature. For the case of B-site substitution, $^4S_{3/2} \rightarrow {}^4I_{15/2}$ emissions are strongly enhanced due to thermal quenching and lower symmetry induced by phase transition.

$Yb^{3+}/Er^{3+}$ co-doped BTO, $Yb^{3+}/Er^{3+}/Tm^{3+}$ tri-doped BTO and $Eu^{3+}$-doped BTO have been synthesized by solid-state reaction method. XRD results showed the dopant ions were doped efficiently into the BTO host. The upconversion PL results indicate that the red, green, and blue emission can be attributed to $Er^{3+}$ and $Tm^{3+}$ ions excited by the direct absorption of 980 nm photons and energy transfer from $Yb^{3+}$ ions. $Yb^{3+}$ ions acting as a sensitizer had a great influence on the upconversion emission of phosphors. The emission intensity balances were changed through control of the dopant concentrations. The $^5D_0 \rightarrow {}^7F_n$ PL spectra of $Eu^{3+}$ were studied. The magnetic and electric dipole transitions may be used to detect the structural asymmetry.

# Chapter 5 Electric-induced Modification of Upconversion of Yb/Er doped $BaTiO_3$ Thin Films

## 5.1 Introduction

The ability to tune the upconversion photoluminescence (PL) of rare-earth-doped phosphors is highly desirable for understanding the physical processes of energy transition and for widespread applications, such as laser mediums, optical waveguides, display, lighting, and biomedicine [Wang, 2010a; Boyer, 2007; Yang, 2009; Wong, 2010; Wang, 2010b]. To date, modification of the upconversion PL in phosphors excited by a given excitation source can normally be achieved through a conventional chemical approach, that is, changing the composition of host materials and/or doping ions. Xiaogang Liu et al. presented a general and versatile approach to fine-tuning the upconversion emission, by doping the same $NaYF_4$ host doped with $Yb^{3+}$, $Er^{3+}$, and $Tm^{3+}$, and adjusting their concentrations. This approach also can be extended to other host-activator combinations [Wang, 2008a]. Jun Lin et al. has synthesized $BaYF_5$:$Yb^{3+}$, $Er^{3+}$, $Tm^{3+}$ phosphors, which can produce different colors, including blue, green, red, and white, by controlling the doping concentration of dopant ions [Zhang, 2011a]. However, the tuning of PL by chemical way is essentially an irreversible and *ex-situ* process, thus limits our understanding of the detailed process of luminescence and applications. The variation of the PL in different hosts can be ascribed to the different crystal field around dopant ions of various symmetries. Low symmetry hosts typically exert a crystal field containing more uneven components around the doped ions compared to high symmetry counterparts [Wang, 2009]. However, it is unlikely to know from the kinetic process how the luminescence changes with structural symmetry. Moreover, it is almost impossible to isolate the pure crystal-field effect from other extrinsic effects present in different samples such as chemical inhomogeneities and defects. Hence, it is much needed to find a pathway in varying the host's symmetry in the same material, leading to the modification of PL. In particular, an enhancement of upconversion still presents a significant challenge. Recently, Hua Zhang et al. proposed a new approach for the modulation of upconversion emission through plasmonic interactions between the upconversion nanocrystals and gold nanostructures [Zhang, 2010]. To date, there are no reports of an established approach to modulate upconversion emission in an *in-situ* and real-time way.

The unique crystal structure of ferroelectric materials provides us an opportunity to couple variables including electric field and temperature to crystal symmetry in a single compound. Approaches through the use of ferroelectric characteristics have recently proven successful in controlling the ferromagnetism, spin polarization, and photovoltaic effects [Stolichnov, 2008; Choi, 2009; Garcia, 2010; Yang, 2010; Wu, 2010]. Comparatively, ferroelectric control of luminescence has not been exploited. Therefore, it is of great interest to take advantage of the properties of ferroelectric host in combination with the luminescent doping ions acting as sensitive process for structure and symmetry. PL in specific materials system should be modulated in reversible, real-time and dynamical way under ferroelectric control that can be realized by electrically changing the structural symmetry. Herein, $BaTiO_3$ (BTO) is selected as ferroelectric host because it has been regarded as a model system for investigating crystal structure transformation under mechanical stress, electric field, and temperature [Ahn, 2004]. Lanthanide $Er^{3+}$ ion is composed of an incompletely filled 4f inner shell and two closed outer shells. Actually, $Er^{3+}$ ion in doped hosts has been a spectroscopic probe for many applications [Polman, 2001; Wen, 2005; Schlaghecken, 2004], including ferroelectric domain imaging [Dierolf, 2003]. Just as described in chapter 4, we have observed the effect of Er doping and measuring temperature on the upconversion emission in BTO: Er powders. Therefore, it is interesting to observe the influence of electric field on the upconversion spectra of Er doping ions. Presently, silicon wafers are extensively used as substrate for fabrication electronic devices [Doering, 2008; Kondo, 2002]. Compared to single crystal substrates, silicon wafers are more available and inexpensive for industrial applications [Alexe, 1997; Warusawithana, 2009]. Perovskite oxides grown on the silicon wafers can be integrated as part of metal-oxide-semiconductor fabrication process.

Herein, we present a new approach to enhance and modulate upconversion emission through applying a relatively low bias voltage to the $Yb^{3+}/Er^{3+}$ co-doped BTO thin film grown on different substrates. Efficient enhanced upconversion PL of the thin films induced by external field was investigated. Reversible and dynamic tuning of the PL has been also realized.

## 5.2 Electric-induced Modification of Upconversion in Epitaxial BTO:Yb/Er Thin Films

### 5.2.1 Experiment

The $Yb^{3+}/Er^{3+}$ co-doped BTO target was prepared by conventional solid-state reaction methods using analytical grade $BaCO_3$, $TiO_2$, $Yb_2O_3$ and $Er_2O_3$ powders as the starting materials. These powders were weighted according to the molecular formula $BaTi_{0.97}Yb_{0.025}Er_{0.005}O_3$ (BTO:Yb/Er). When $Yb^{3+}$ and $Er^{3+}$ were substituted at the $Ti^{4+}$ site, the negative effective charge could be compensated by oxygen vacancies, respectively. The starting powders with designed stoichiometric quantities were ball milled for 24 h, the dried and calcinated at 1100 °C for 8 h. The resulting powders were pressed into disk pellets and sintered at 1350 °C for 4 h. The as-prepared target showed a prominent BTO crystalline phase in the XRD pattern. The BTO:Yb/Er thin film was grown by pulsed laser deposition (PLD). A 150 nm thickness lattice-matched $SrRuO_3$ (SRO) was used as a bottom electrode between BTO:Yb/Er film and $SrTiO_3$ (STO) substrate. The BTO:Yb/Er-SRO bilayers were deposited in situ with the substrate temperature of 700 °C, oxygen pressure of 20 Pa, and laser pulse energy density of 5 J/cm$^2$. The thickness of the BTO:Yb/Er film was 800 nm. After the deposition, the bilayer films were *in-situ* post-annealed at the growth temperature in 0.5 atm oxygen pressure for 15 min before they were allowed to cool naturally to room temperature to minimize oxygen deficiency. A 200 nm thick ITO layer as a top transparent electrode was deposited on the BTO:Yb/Er film at 700 °C under 2.5 Pa oxygen ambient by PLD.

Characterization: The crystal structure of the multi-layer structure was examined by a Bruker D8 discover X-ray diffractometer with Cu Kα radiation. The surface morphology of the films was analyzed using an Atomic Force Microscopy (AFM) (Nanoscope IV, Digital Instruments). The PL spectra were recorded using an Edinburgh FLSP920 spectrophotometer under the excitation of a 980 nm diode laser. All measurements were carried out at room temperature.

### 5.2.2 Results and Discussion

The method used for the modification of upconversion from BTO:Yb/Er thin film under control of electric field is shown in Figure 5.1. The light excitation and emission as well as applied electric field are denoted. The emission light can pass through the transparent indium tin oxide (ITO) electrode layer. The utilization of the BTO:Yb/Er thin film described herein facilitates the application of higher electric field on the sample under a low bias voltage than required for the bulk material.

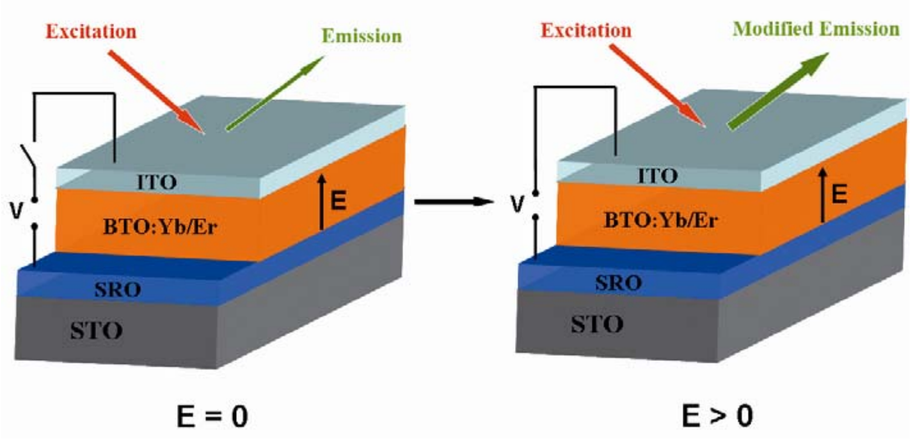

Figure 5.1. The setup used to measure the upconversion emission of a BTO:Yb/Er thin film when an external electric field is switched “off” and “on” (right). A 980 nm diode laser is used as an excitation source. See text for details.

The X-ray diffraction (XRD) patterns of the BTO:Yb/Er thin film on the SRO-coated STO (001) substrate are shown in Figures 5.2 and 5.3. In the $\theta$-$2\theta$ scan, only the (00*l*) peaks of BTO are present along with those of the STO substrate and SRO buffer layers (Figure 5.2). This result shows that the BTO:Yb/Er film grows with its *c*-axis normal to the substrate surface. The full widths at half-maximum (FWHM) of the BTO (001) and (002) peaks are approximately 0.2° and 0.3°, respectively. These small FWHMs indicate good crystallinity of the BTO:Yb/Er thin film along the out-of-plane orientation.

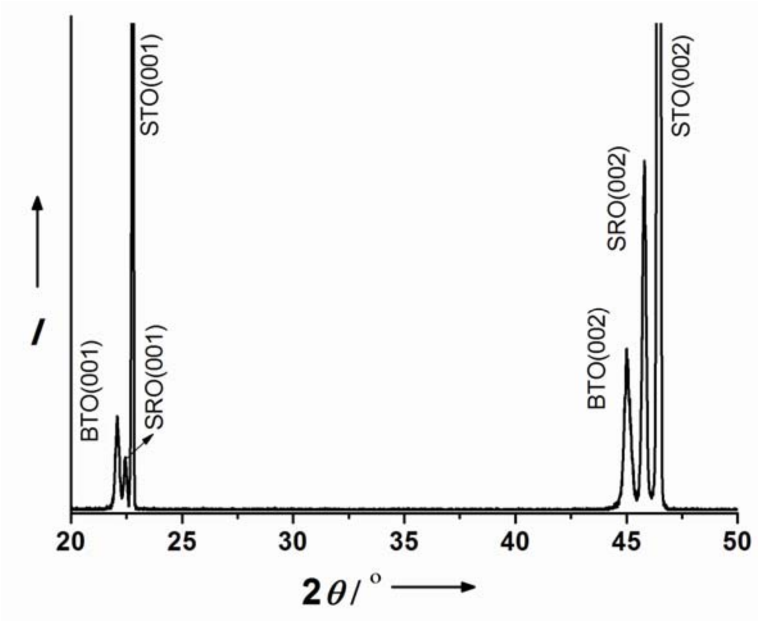

Figure 5.2. XRD $\theta$-$2\theta$ scan of the BTO:Yb/Er thin film grown on a conductive SRO buffered STO substrate.

The $\phi$ scans for the BTO:Yb/Er film on the STO substrate/SRO buffer layer are shown in Figure 5.3. The (101) diffraction peaks for the BTO:Yb/Er film and the substrate/buffer layer are used. Only four peaks, 90° apart, are observed for the BTO:Yb/Er film, which are at the same angles with those of substrate/buffer layer. This indicates that the BTO:Yb/Er film is in-plane aligned with the substrate/buffer layer. Thus, XRD measurements reveal that the BTO:Yb/Er film was epitaxially grown on the (001) surface of SRO with an in-plane relationship of [100]BTO//[100]SRO//[100]STO.

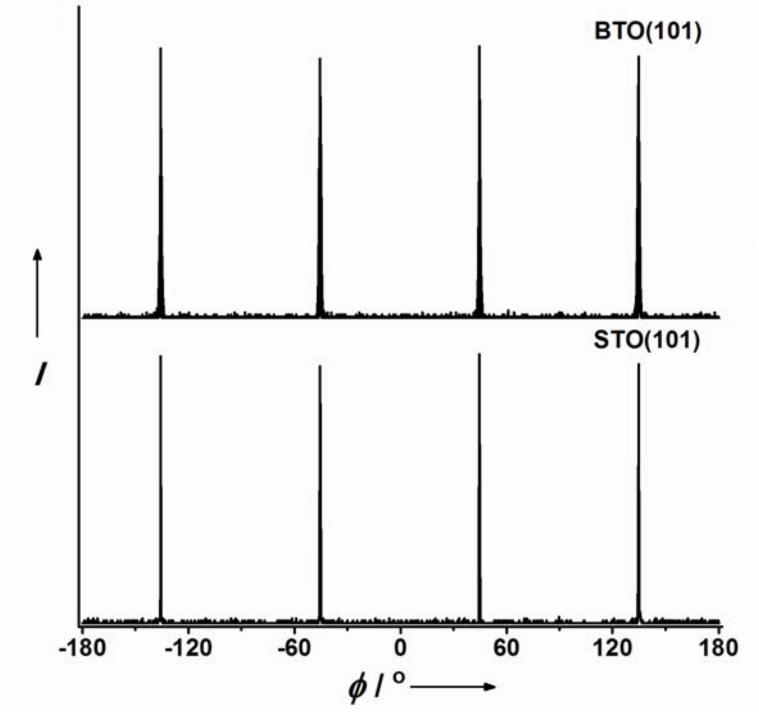

Figure 5.3. XRD $\phi$ scans for the BTO:Yb/Er film on the STO substrate/SRO buffer layer using the (101) peaks for BTO:Yb/Er film and the STO substrate/SRO buffer layer.

Figure 5.4 shows an AFM surface morphology image of the BTO:Yb/Er film grown on the SRO-coated STO substrate. The BTO:Yb/Er thin film shows a uniform surface morphology with a root-mean-square (RMS) of 3.2 nm.

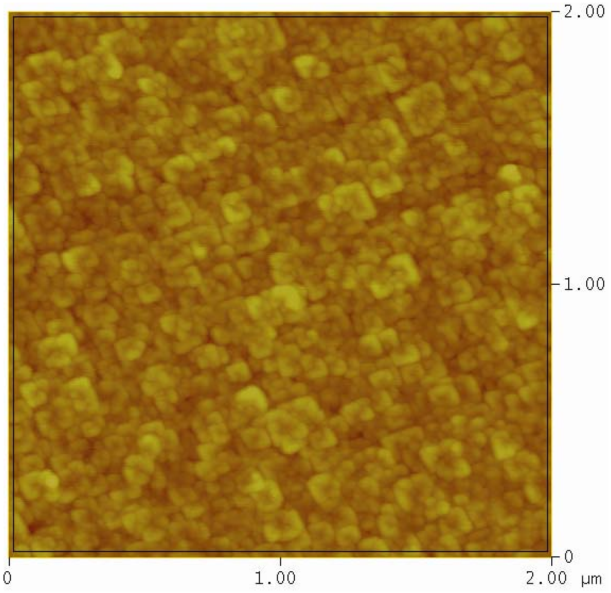

Figure 5.4. AFM image of the epitaxial BTO:Yb/Er film on the SRO-coated STO substrate.

The two-photon upconversion mechanism is described in Figure 5.5. Owing to the weak ground-state absorption of $Er^{3+}$ ions pumped by 980 nm laser, $Yb^{3+}$ ions as sensitizers are often preferred for increasing the pumping efficiency because of the efficient energy transfer from $Yb^{3+}$ to $Er^{3+}$ ions.

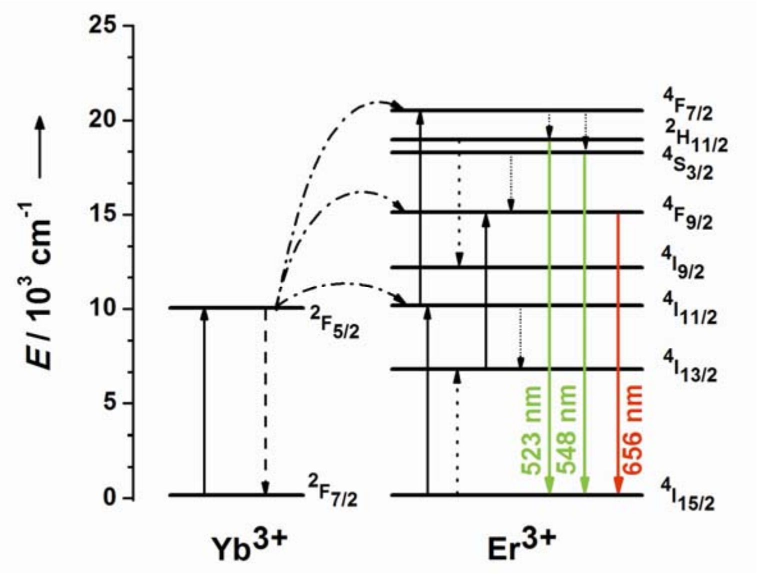

Figure 5.5. Energy scheme with the relevant upconversion process in $Yb^{3+}/Er^{3+}$ co-doped BTO. The dashed-dotted, dashed, and dotted lines represent energy transfer, multiphonon relaxation, and cross-relaxation, respectively.

Figure 5.6 shows the upconversion spectra of BTO:Yb/Er under a bias voltage up to 10 V limited by the breakdown voltage. Great attention was paid to ensure that the BTO:Yb/Er thin film was kept to be an insulator during measurements by monitoring leakage current. Green emission bands centered at 523/548 nm correspond to $^2H_{11/2}/^4S_{3/2} \rightarrow {}^4I_{15/2}$ transitions of $Er^{3+}$ ion. Generally, the PL intensity of thin films which can be measured is usually much lower than that of the corresponding bulks or powders. Therefore, the relatively high power density of incident light was used in our measurements in order to enhance the ratio of signal to noise. Since the upper $^2H_{11/2}$ level is thermally populated at the expense of $^4S_{3/2}$ level owing to Boltzmann's distribution [Vetrone, 2010], the emission from $^2H_{11/2}$ level is more intense than that from $^4S_{3/2}$ state (Figure 5.6), owing to the thermal effect caused by the laser. Obviously, the upconversion can be strongly enhanced when increasing the dc bias voltage. An enhancement factor of main green band can reach up to 2.7. on the other hand, the red emission band centered at 656 nm corresponding to $^4F_{9/2} \rightarrow {}^4I_{15/2}$ transition of the $Er^{3+}$ ion almost remains unchanged with an increase of voltage.

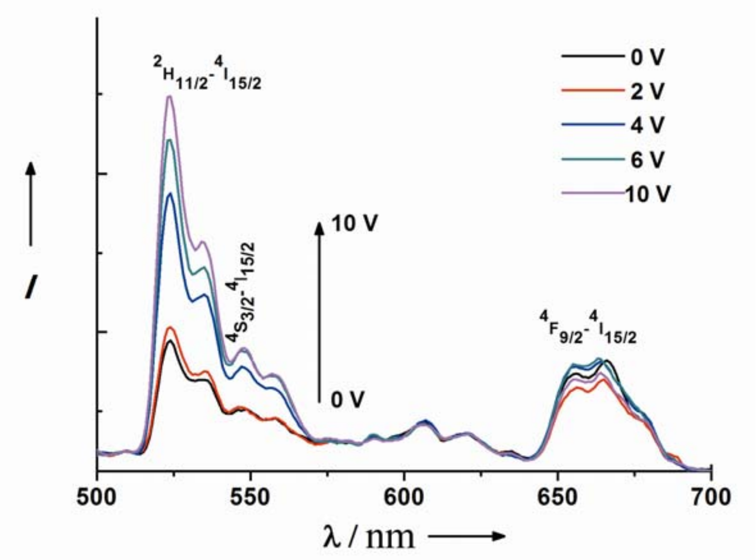

Figure 5.6. The upconversion emission spectra of the BTO:Yb/Er film under dc bias voltage ranging from 0 to 10 V.

As can be seen in Figure 5.7, the enhancement factors located in the green band are much higher than those in the red band. It indicates that the emission enhancement is highly wavelength-dependent. The PL intensity ratio of green to red emission ($f_{g/r}$) is significantly enhanced with increasing dc bias voltage up to 10 V, which is equivalent to an electric field of 125 kVcm$^{-1}$. The result rules out a potential piezoelectric effect that causes a misalignment of the sample.

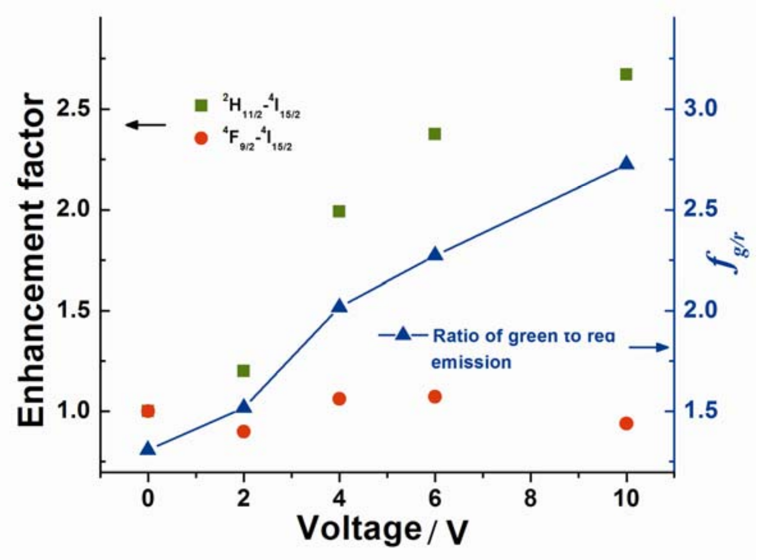

Figure 5.7. The enhancement factors (left axis) for green and red emission band as a function of the applied dc voltage. The PL intensity ratio of green to red emission ($f_{g/r}$) (right axis) as a function of the applied bias voltages is also shown. The thin film sample is excited by a 980 diode laser.

We have demonstrated a novel approach to modify PL. A large number of previous studies have indicated that the PL of dopant ions could be influenced by the crystal symmetry of the host materials [Kuo, 2005; Heer, 2004]. Tung-Ching Huang, et al. investigated the $Yb^{3+}$/$Er^{3+}$ co-doped ferroelectric perovskites with different tetragonal phases for controlling visible upconversion emissions. They found that the larger asymmetric crystal field at high $Yb^{3+}$ concentration resulted in weak red emission [Huang, 2009]. However, approaches to vary the symmetry of the host materials have been limited to the use of chemical routes to date. In Figure 5.6, the external electric field is applied to a ferroelectric BTO host to modify PL instead of conventional chemical methods. The observed results are largely ascribed to the unique crystal of ferroelectric host, which can provide an opportunity to couple variables including electric field to crystal symmetry. In a sense, the consequence for the variable-symmetry in a single ferroelectric host controlled by an external electric field in this work is in analogy to that for variation of symmetry in different hosts made by conventional chemical route. Lattice distortions under an electric field in a mono-domain of BTO ferroelectric crystal have been detected with X-ray radiation [Tazaki, 2009]. The prototypical perovskite BTO used in this work is non-centrosymmetric in tetragonal phase with the point group 4*mm* ($C_{4v}$) at room temperature, and Ti is shifted related to the negatively charged oxygen atoms, producing a polarization (Figure 5.8a). The variation of the lattice constant under an electric field was observed to show a linear response nature of the piezoelectric effect. When an electric field is applied along the spontaneous polarization direction, the *c*-axis of the lattice elongates and the a-axis shrinks (Figure 5.8b).

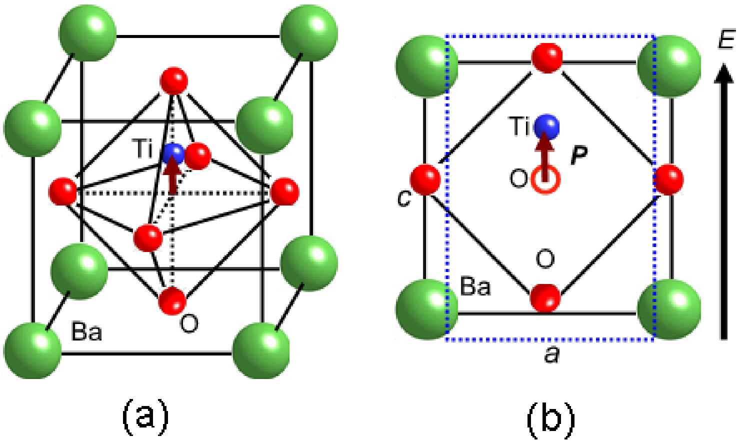

Figure 5.8. (a) Tetragonal perovskite structure of BTO. (b) Piezoelectric effects in a BTO lattice with a tetragonal structure under an electric field [Tazaki, 2009].

Our previous study showed that the doping $Er^{3+}$ ions can substitute $Ti^{4+}$ ions in BTO, hence $Er^{3+}$ ions in the lattice are non-centrosymmetric even when no electric field is applied. Therefore, the perturbation caused by the odd-order term of crystal-field forces the parity forbidden 4f-4f electric dipole (ED) transitions allowed, leading to the observed PL emission with zero bias as shown in Figure 5.6. When applying an electric field along the direction of spontaneous polarization, the *c*-axis of the lattice elongates (Figure 5.8b) and promotes the structure asymmetry of the BTO host, approaching lower symmetry around $Er^{3+}$ ions. In principle, the lower symmetry at the site of lanthanide ions means that the more uneven crystal-field components can mix opposite-parity into 4f configurational levels and subsequently increase the ED transition probabilities of the dopant ions. Herein, the increase in the radiative transition probabilities relating to the displacement of $Ti^{4+}$ and $O^{2-}$ ions by the external electric field is responsible for the enhancement of PL emission with bias as shown in Figure 5.6, while nonradiative transition probabilities are not dependent on the site symmetry.

The difference in the enhancement factors of green and red emission band shown in Figure 5.7 could be considered that the extent of the local symmetry influence on the different emission band may vary greatly, depending on the corresponding intra-4f transitions. According to the Judd-Ofelt (J-O) theory [Judd, 1962; Weber, 1967], the spontaneous emission probability $A_{ed}$ for an ED transition between initial $J$ manifold $|[S,L]J\rangle$ and a final $J$ manifold $|[S',L']J'\rangle$ is given by Eq. (5.1)

$$A_{\mathrm{ed}} = \frac{64\pi^4 e^2}{3h(2J+1)\lambda^3}[\frac{n(n^2+2)^2}{9}]S_{\mathrm{ed}} \tag{5.1}$$

where $e$ is the electron charge, λ is the mean wavelength of the transition, $n$ is the refractive index at the wavelength of the transition and $h$ is plank constant. The ED line strength $S_{\mathrm{ed}}$ is given by Eq. (5.2)

$$S_{\mathrm{ed}} = \sum_{t=2,4,6} \Omega_t \left| \left\langle 4f^n[S,L]J \left\| U^{(t)} \right\| 4f^n[S',L']J' \right\rangle \right|^2 \tag{5.2}$$

where three terms $<||U^{(t)}||>$ are reduced matrix elements of the unit tensor operators, and three J-O intensity parameters $\Omega_t$ ($t$ = 2,4,6) contain the effect of the crystal-field terms, radial integrals of an electron, and so on. In Figure 5.5, the transition producing main green emission band is one of hypersensitive transitions of $\mathrm{Er}^{3+}$ ions which could occur in the point group 4*mm* ($C_{4\mathrm{v}}$) of BTO. Such a hypersensitive transition is dominated by $\Omega_2$. Furthermore, the variation of $\Omega_2$ parameter is known to be closely associated with asymmetry of the lanthanide ion sites [Tanabe, 1992]. The lower symmetry usually contributed to the larger $\Omega_2$. Therefore, the larger enhancement factor of main green band shown in Figure 5.7 should be due to the increased $\Omega_2$ parameter induced by the lower symmetry of $\mathrm{Er}^{3+}$ sites with the application of electric field. On the other hand, the red emission is little affected by $\Omega_2$ and is therefore, relatively insensitive to the variation in local symmetry. Consequently, we consider that the observed modification of PL emission in BTO:Yb/Er is attributed to an increase of distortion of $\mathrm{Er}^{3+}$ site symmetry caused by an external electric field strongly coupling on the ferroelectric BTO host.

Note that the PL intensity at the wavelength of 523 nm from the sample under the bias voltage at 10 V is almost 2.7 times that of the unbiased sample in Figure 5.6. Currently, the enhancement of inefficient upconversion still represents a great challenge. Very recently, an enhancement factor of about 3 from Plasmon-enhanced upconversion was reached in $NaYF_4$ nanocrystals co-doped with $Yb^{3+}/Er^{3+}$ or $Yb^{3+}/Tm^{3+}$ through very precise manipulation. Plasmon-enhanced upconversion PL was recently presented. Stefan Schietinger et al. performed enhanced upconversion PL by controlled nanoassembly of $NaYF_4$:$Yb^{3+}$, $Er^{3+}$ nanoparticles with gold nanospheres (Figure 5.9). Later, Hua Zhang et al. reported the distinct modulation of upconversion emission through plasmonic interaction between the $NaYF_4$:$Yb^{3+}$, $Tm^{3+}$ nanocrystals and gold nanostructures [Zhang, 2010]. They found the attachment of gold nanostructures onto the upconversion nanoparticles can enhance the upconversion emission. While, the gold shell can significantly suppress the emission, because of considerable scattering of excitation irradiation (Figure 5.10). The enhanced upconversion from the gold nanstructures was attributed to the local electric-field enhancement associated with plasmonic resonance. Comparatively, we can simply apply a relatively low voltage to the sample and obtain the upconversion with an enhancement factor comparable to that of Plasmon-enhanced upconversion. Definitely, the value of enhancement factor reported herein is not a fundamental limit as the BTO:Yb/Er film was not completely poled in the measurement. There is much room for improvement, for example, applying larger poling fields limited by the breakdown field.

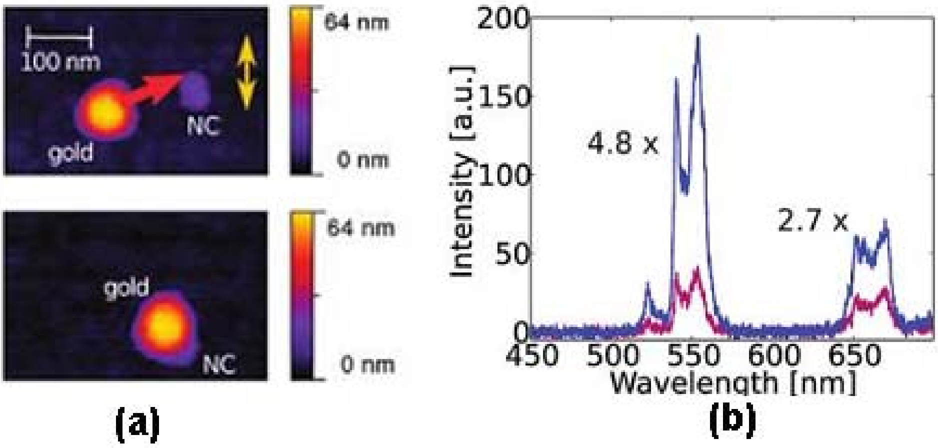

Figure 5.9. (a) AFM image showing the nanoassembly approach. (b) Upconversion spectra of $NaYF_4$:$Yb^{3+}$, $Er^{3+}$ nanoparticles without (violet curve) and with (blue curve) the gold nanosphere in close vicinity [Schietinger, 2010].

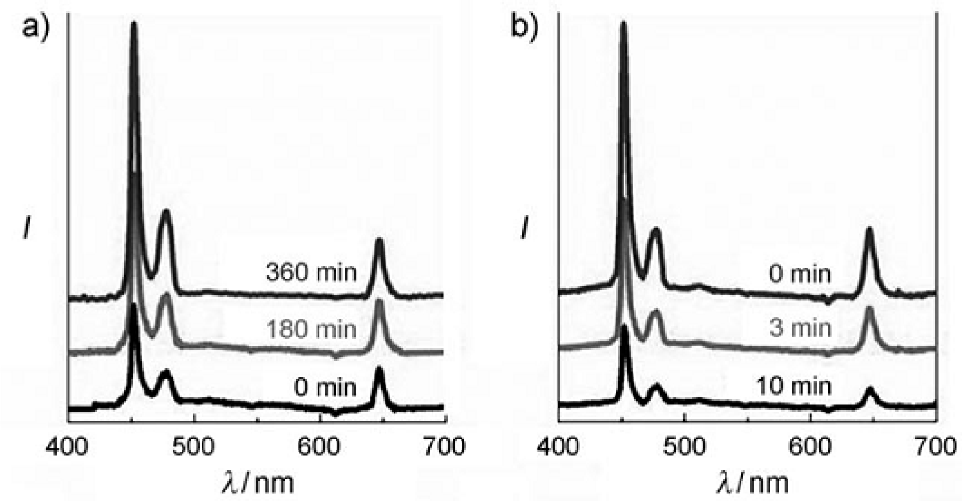

Figure 5.10. Upconversion emission spectra of $NaYF_4$: $Yb^{3+}$, $Tm^{3+}$ nanoparticles during (a) gold nanostructures attachment state 0-360 min. (b) gold shell growth state 0-10 min [Zhang, 2010].

The structural symmetry in ferroelectrics can be switchable, implying that reversible and dynamic tuning of PL emission by external electric field could be realized. To validate the hypothesis, we further study on the modification of PL with the application of ac electric field. It indicates that the specific emission of BTO:Yb/Er can not only be amplified, but also be electrically modulated. Figure 5.11 shows the kinetics of PL emission at the wavelength of 523 nm in BTO:Yb/Er thin film under a sinusoidal ac bias. It is found that the PL intensity of the BTO:Yb/Er film can be modulated with the same frequency as that of the sinusoidal ac electric voltage. Obviously, the modulation of upconversion PL can not be realized by conventional chemical and plasmonic methods. To the best of our knowledge, a reversible control of the upconversion by applying low voltages has not yet been reported. It could open up a new avenue for potential device applications, such as electric controlled upconvertors.

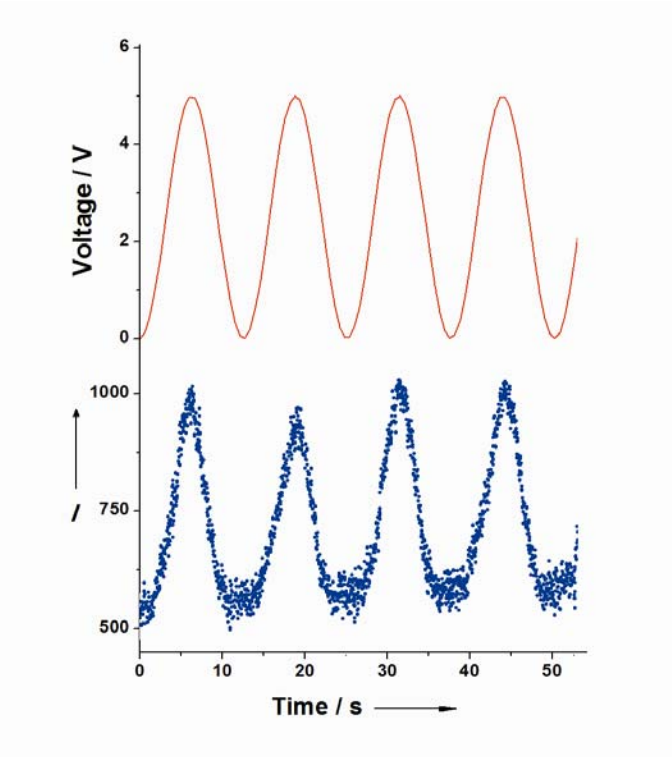

Figure 5.11. Sinusoidal ac electric voltage applied to the BTO:Yb/Er film (top), and PL emission at a wavelength of 523 nm as a function of time while the sinusoidal ac electric field is applied to the BTO:Yb/Er film (bottom).

## 5.3 Enhanced Upconversion in BTO:Yb/Er Thin Films Grown on Semiconductor Wafer

### 5.3.1 Experimental

$Yb^{3+}$/$Er^{3+}$ co-doped BTO (BTO:Yb/Er) target was prepared by conventional solid-state reaction method as shown in previous chapter. The BTO:Yb/Er films were grown on (100)-oriented Si wafer with a (111)-oriented Pt buffered layer by

PLD. The BTO:Yb/Er films were deposited with the substrate temperature of 680 °C, oxygen pressure of 20 Pa, and laser pulse energy density of 5 J/cm$^2$. The thickness of the films was 700 nm. After the deposition, the films were *in-situ* post-annealed at the growth temperature in 0.5 atm oxygen pressure for 15 min. A 200 nm thick ITO layer as top transparent electrode was deposited on the BTO:Yb/Er film at 250 °C under 2.5 Pa oxygen ambient by PLD.

The films were characterized by XRD using a Bruker D8 Discover X-ray diffractometer with Cu K$\alpha$ radiation. The surface morphology of the films was investigated by field-emission scanning electron microscopy (FE-SEM, JEOL-JSM 6335F). Raman spectra were measured using a Horiba Jobin Yvon HR800 Raman spectrometer with a 488 nm laser excitation source. The PL spectra were recorded using an Edinburgh FLS920 spectrophotometer under the excitation of a 980 nm diode laser. All measurements were carried out at room temperature.

### 5.3.2 Results and Discussion

The XRD patterns of the BTO:Yb/Er thin films on Pt-buffered Si substrate are shown in Figure 5.12. Pt is used as bottom electrode grown on Si (100) substrates with the (111) orientation. In the $\theta$-$2\theta$ scan, the BTO (111) peak at 38.8° on the Pt (111) at 39.9°, the Si (100) peak was at 69.1°. No other peaks were present for BTO:Yb/Er thin films. This shows that the BTO:Yb/Er film is basically highly oriented grown on Pt-buffered Si substrate. At room temperature, the lattice mismatch between Pt ($a$ = 3.92 Å) between BTO (tetragonal, $a$ = 3.92 Å, $c$ = 4.03 Å) is about 2.73%. Therefore, the small lattice mismatch is recognized as an important factor for highly oriented growth [Yang, 2010].

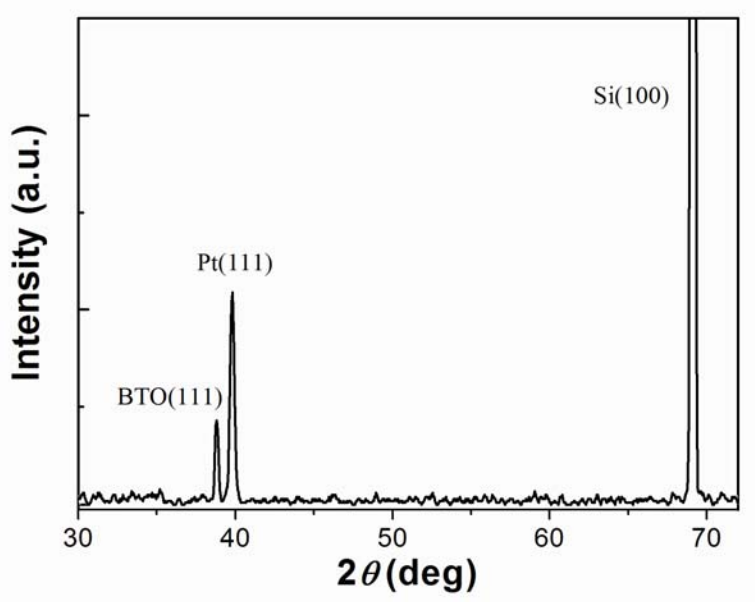

Figure 5.12. XRD patterns of BTO:Yb/Er thin film grown on Pt-buffered Si substrate.

Compared to XRD, Raman spectroscopy is more sensitive to impurity phase. Figure 5.13 gives the Raman scattering spectra of BTO:Yb/Er at room temperature. The Raman peaks located at ~ 305 cm$^{-1}$ and ~720 cm$^{-1}$ correspond to the E(TO$_2$) and A$_1$(LO$_3$) phonon modes, respectively, which are specific to the tetragonal phase of BTO [Yeung, 2004]. A weak peak is located at 270 cm$^{-1}$ corresponding to A$_1$(TO$_2$) phonon mode. The strong peak at 525 cm$^{-1}$ are attributed to A$_1$(TO$_3$) mode of either tetragonal or cubic phase of BTO. Raman spectra confirm that the BTO:Yb/Er on Pt-buffered Si substrate has good crystalline without other secondary phases. Raman result also indicates the presence of a tetragonal phase in the BTO:Yb/Er thin film that we have prepared.

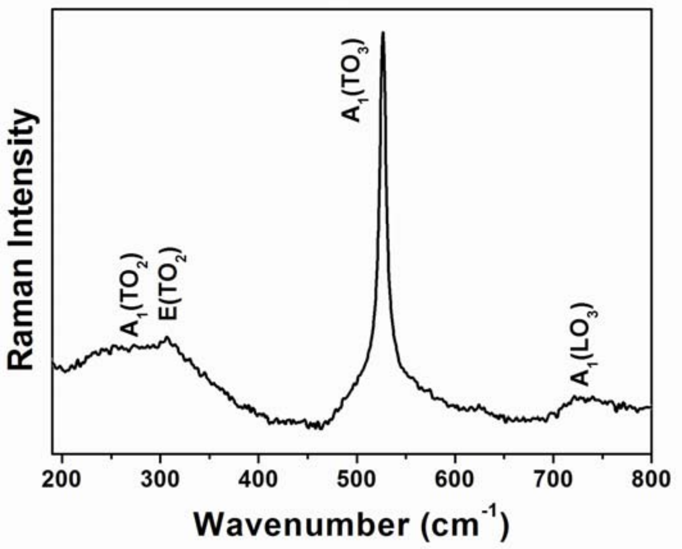

Figure 5.13. Raman spectra of BTO:Yb/Er thin film grown on Pt-buffered Si substrate.

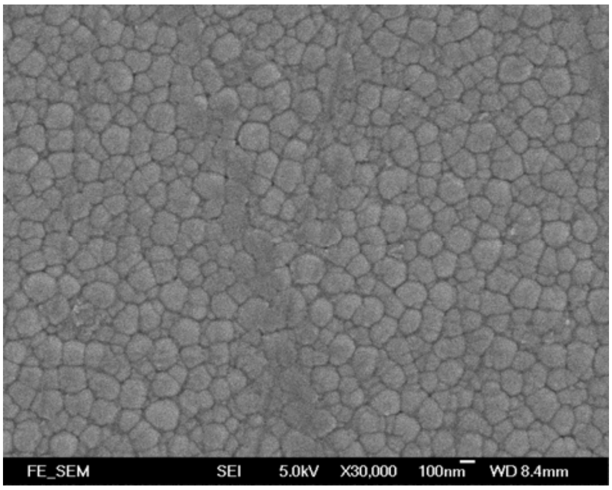

Figure 5.14. FE-SEM image of BTO:Yb/Er thin film grown on Pt-buffered Si substrate.

The FE-SEM images as shown in Figure 5.14 illustrate the surface morphology of the BTO:Yb/Er thin film grown on Pt-buffered Si substrate. The FE-SEM image indicates that the BTO:Yb/Er thin film was prepared, with a uniform ~150 nm grain texture.

Figure 5.15a shows the emission spectra of BTO:Yb/Er thin film under a bias voltage up to 14 V limited by the breakdown voltage. The typical upconversion emission under infrared excitation (~980 nm) consists of two strong green bands located at 526 and 553 nm are attributed to the $^2H_{11/2} \rightarrow {}^4I_{15/2}$ and $^4S_{3/2} \rightarrow {}^4I_{15/2}$ transitions of $Er^{3+}$ ions, and a red emission band at 660 nm corresponds to the $^4F_{9/2} \rightarrow {}^4I_{15/2}$ transition of $Er^{3+}$ ions, respectively. BTO:Yb/Er film was kept to be an insulator during PL measurement by monitoring leakage current. It can be seen that the upconversion PL is obviously enhanced along with increasing the dc bias voltage. Additionally, it is interesting to note that the enhancement factors are highly wavelength-dependent. The green emission increased about 40% in emission intensity, while an increase of only approximately 20% was observed at the red band (Figure 5.15b). The result suppresses a potential interference originated from piezoelectric effect. The emission from $^2H_{11/2}$ level is more intense than that from $^4S_{3/2}$ state is attributed to the thermal effect caused by the laser.

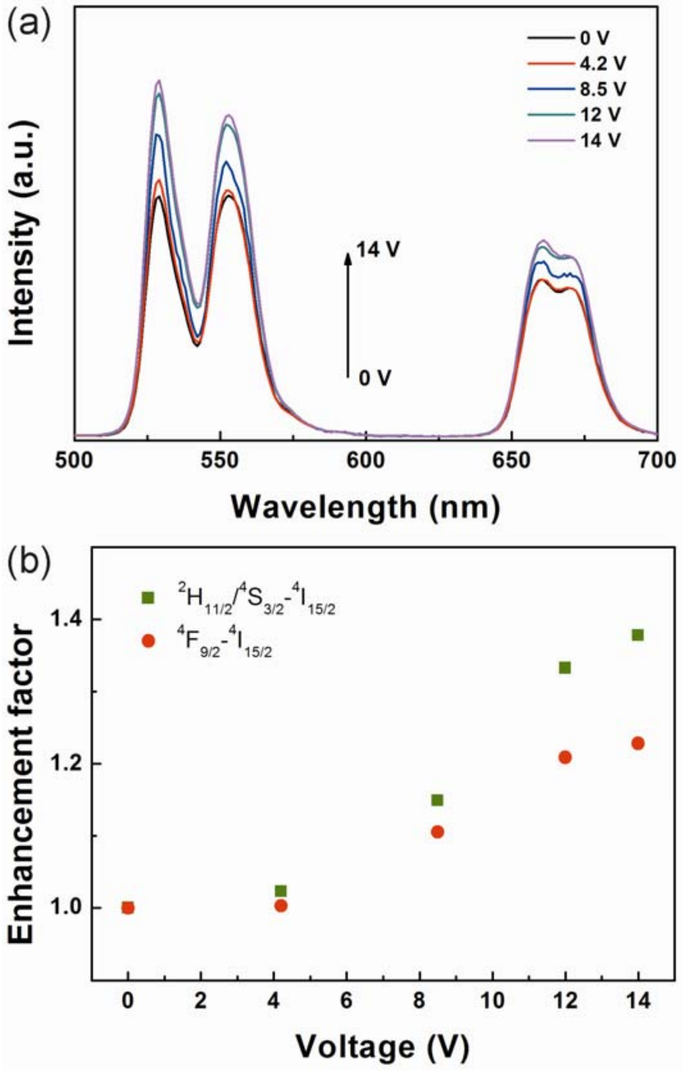

Figure 5.15. (a) The upconversion emission spectra of BTO:Yb/Er thin film grown on Pt-buffered Si substrate under dc bias voltage ranging from 0 to 14 V. (b) The enhancement factors for green and red emission bands as a function of the applied dc voltage. The thin film sample is excited by a 980 nm diode laser.

Previous studies have indicated that the luminescent properties of dopant rare-earth ions are strongly dependent on the crystal symmetry. The different crystal field caused by structure symmetry of the host materials would contribute to different perturbation terms for the dopant ions 4f transitions [Wang, 2009]. As the analysis we proposed above, an electric field applied on the BTO thin film has promotes the structure asymmetry of the BTO host. The 4f transitions arising from forced electric dipole are parity forbidden and become partially allowed when the dopant ions are situated at the asymmetry site, which allows mixing of the 4f states with higher electronic configuration. The lower symmetry around dopant ions typically contributes to higher transition probabilities of the dopant ions. Herein, we observed the enhanced upconversion PL in BTO:Yb/Er on Pt-buffered Si wafer. As to the enhancement factor for green band herein is smaller than that of epitaxial BTO:Yb/Er film on STO maybe boil down to two reasons. Due to the mismatch between Pt and BTO, we can not obtain the epitaxial BTO:Yb/Er thin film grown on Pt-buffered Si substrate. So, the poor quality of BTO film here may reduce the enhancement factor. XRD result shows that the BTO:Yb/Er film is oriented along (111) direction grown on Pt-buffered Si substrate. The electric field is applied along the (001) direction. The misalignment also contributes lower enhancement factor.

To understand the different influence of local symmetry on green and red bands can refer to the J-O theory. As we discussed, the main green emission band is associated with one of the hypersensitive transition of $Er^{3+}$ ions. It is well known that the hypersensitive transitions are dominated by $\Omega_2$, while $\Omega_2$ is very sensitive to the site symmetry around $Er^{3+}$ ions. So, different sensitivity to the change of site symmetry contributes to different enhancement factor in Figure 5.15b.

Dynamic switching of the upconversion PL with a given excitation source is highly demand for applications. Here, we realized electric-field-controllable tuning of PL. The unique structure of ferroelectric materials provides the opportunity to couple electric field to crystal symmetry. Figure 5.16 shows the kinetics response of PL emissions at 526 and 660 nm in BTO:Yb/Er thin film as a function of time while a 12 V bias voltage applied to the film was switched on and off. The PL intensities increase sharply when the electric field was switched on and then returned to their initial values upon the removal of the external electric field. This modification of upconversion PL can be realized with in situ and real-time way.

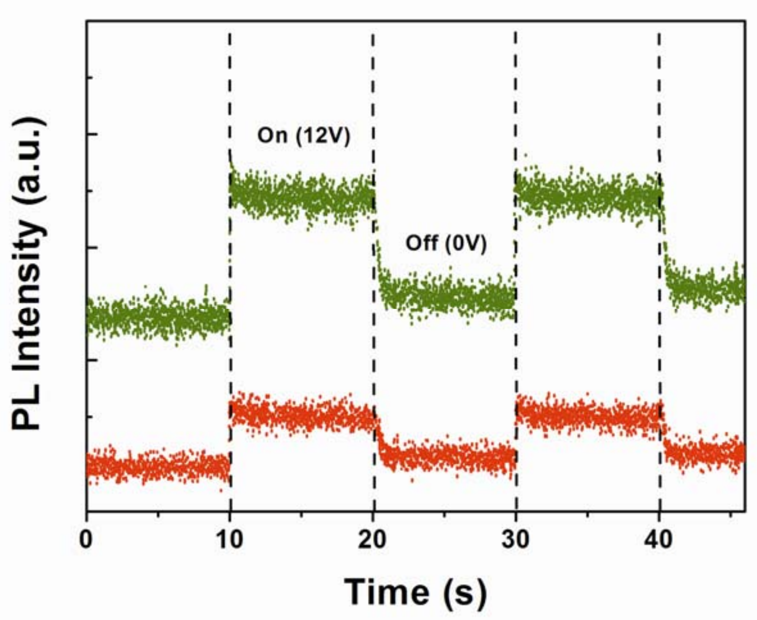

Figure 5.16. PL emissions at 526 nm (green) and 660 nm (red) of BTO:Yb/Er thin film grown on Pt-buffered Si substrate as a function of time while a 12 V bias voltage was switched on and off. The thin film sample is excited by a 980 nm diode laser.

## 5.4 Conclusion

In this chapter, electric-induced enhancement and modulation of upconversion PL in BTO:Yb/Er thin films grown on different substrates were realized. We have demonstrated that the enhancement and modulation of upconversion PL can be realized by applying low voltages to BTO:Yb/Er thin films in an *in-situ* and real-time manner. The emission intensity of main green band of epitaxial BTO:Yb/Er thin film under the bias voltage at 10 V is almost 2.7 times as that of the unbiased one. The approach for the modification of PL is in contrast to conventional chemical routes, such as changing the composition of host materials and/or doping ions. The observed phenomena can be ascribed to the increase in the radiative transition probabilities resulting from the lower symmetry of $Er^{3+}$ sites which arises when an external electric field is applied. These results will aid further investigations of luminescence and the widespread applications of upconversion materials because they provide an additional degree of freedom in the design of luminescent materials and devices.

# Chapter 6 Strain-Mediated Light Emission from ZnS:Mn/PMN-PT Structure

## 6.1 Introduction

The phenomena of electroluminescence (EL) have attracted an ever-increasing demand for applications throughout the illumination and display industries [Walters, 2005; Takashima, 2009; Wellenius, 2008; Hao, 2004; Shao, 2011]. In EL devices, the light generation in light−emitting diodes (LEDs) is mostly investigated for flat-panel display and lighting sources due to their high brightness, long life and low power consumption [Chung, 2010; Pimputkar, 2009; Vasilopoulou, 2007]. It is well-known that the LED is essentially a p-n junction diode typically made from semiconductors. The light emission is generated by the direct injection and subsequent recombination of electron-hole pairs in the forward-biased p-n junction [Holonyak, 1962]. The phenomenon of light emission from such electron-hole pair recombination as a result of minority carrier injection is regarded as injection EL. A little surprise for us is that very limited work on exploiting EL devices beyond the p-n junction structure has been reported in the last decades. In order to find a novel light source based on some mechanism differing from the p-n junction based LEDs, an important question in this area, both scientifically and technologically, is how to tailor the materials properties and therefore construct a new device structure.

Particularly, it should be very attractive if the light source could generate other signal to offer a novel multi-modal functional source.

Note or it should be noted that an emerging field so-called piezo-phototronics recently was proposed by Zhong-Lin Wang is of particular interest [Wang, 2010c]. Piezo-phototronics derive from the term “piezotronics”, which defines utilization of strain-induced piezoelectric potential to tune and gate the charge transport behaviors for fabricating new functional devices [Wang, 2006b; Wang, 2007]. Furthermore, the piezoelectric potential utilized in optoelectronic devices results in piezo-phototronics. The functionality of piezotronics and piezo-phototronics ranging from nanogenerators [Hu, 2010; Xu, 2010; Cha, 2010] and field effect transistors [Kwon, 2008] to photosensors [Yang, 2010] and piezoelectric diodes [Zhou, 2008; Yang, 2011] are ultimately based on the intricate coupling of piezoelectric, semiconducting and photonic characteristics. So far, the previous works on piezo-phototronics are limited to one-dimensional (1D) nanostructure. Hence, it is much needed to know whether this new concept is applicable to other device configuration or not, such as thin film structure. Compared with 1D nanostructures, the utilization of thin-film structure would be beneficial to increasing device reproducibility and reducing the fabrication cost because of the mature thin-film fabrication technologies. Additionally, thin-film structure facilitates the integration and patterning of device. Here, we report on the fabrication and characteristics of strain-induced piezoelectric potential stimulated luminescence from ZnS:Mn film grown on piezoelectric $Pb(Mg_{1/3}Nb_{2/3})O_3$-$x$$PbTiO_3$ (PMN-PT) substrate. PMN-PT was chosen as substrates due to its outstanding ferroelectric polarization and converse piezoelectric effects. PMN-PT single crystal has been extensively used to *in situ* investigate the strain-related characteristics of various samples [Zheng, 2007; Guo, 2011]. In addition, PMN-PT single crystal features large piezoelectric coefficients and extraordinary high electromechanical coupling factors, these merits translate into high performance of the ultrasound transducer fabricated with PMN-PT single crystal [Peng, 2010]. The simultaneous generation of light and ultrasound wave is firstly demonstrated using a single system in this work. We can tune the luminescence and ultrasound signal of the ZnS:Mn films via a converse piezoelectric effect in PMN-PT upon the application of an ac or dc applied electric-field. Currently, a variety of techniques such as high- frequency ultrasound imaging and fluorescence spectroscopy have been widely used for medical diagnosis. However, each of these techniques has intrinsic advantages and deficiencies. There is a trend to develop a combined approach capable of evaluating structural characteristics as well as biochemical properties, which may provide higher predictive and complementary information compared to a single approach, either by optical or ultrasound method [Sun, 2009]. Therefore, the novel dual-modal source combining light-emission and ultrasound generation on a single wafer here will be very helpful in developing the hybrid system for tissue diagnosis.

## 6.2 Experiment

ZnS:Mn thin films were grown on (001) cut PMN-PT single crystal substrate by pulsed laser deposition with a KrF excimer laser (wavelength 248 nm). The PMN-PT single crystal was cut into plates of dimensions of 5 mm × 3 mm × 0.5 mm. The pulse repetition frequency and energy density were 5 Hz and 2 J/cm$^2$, respectively. The substrate temperature and based pressure of the vacuum chamber were fixed at 500 $^{o}$C and $5\times10^{-3}$ Pa. After deposition, the ZnS:Mn films were slowly cooled down to room temperature. An ITO transparent conductive electrode was grown on the top of the film at 200 $^{o}$C under a 2.0 Pa oxygen pressure. The 200 nm thick Au electrode on the back of PMN-PT substrate was coating by a sputtering system at room temperature.

The XRD measurements were carried out using a four-circle Bruker D8 Discover X-ray diffractometer equipped with a four-bounce Ge (220) monochromator. TEM and SAED were performed on a JEOL 2010 electron microscope furnished with energy dispersive x-ray, operating at a voltage of 200 kV.

The polarization of the PMN-PT substrate was done using a Keithley 2410 Source-Meter with a high-voltage output. The samples were positively polarized in the thickness direction (i.e., the electric dipole moments in the PMN-PT substrate point toward the ZnS:Mn film). The AC signals applied on the sample were produced using a Keithley 3390 Arbitrary Waveform/Function generator connected with a voltage amplifier. The dielectric properties were carried out on a precision impedance analyzer 4294A (Agilent, USA) at room temperature. A conventional pulsed-echo response arrangement was adopted to measure the performance of the ZnS:Mn/PMN-PT structure as a transducer. The sample was connected to a Panametrics 5900PR pulser/receiver (Waltham, MA), and mounted in front of a thick stainless target with a proper distance in a water tank. An oscilloscope (HP Infinium, Agilent) was used to record the pulsed-echo signal. The luminescence measurements were recorded using an Edinburgh FLSP920 spectrophotometer. The photographs were obtained by an inverted microscope (IX-71, Olympus). For luminescence and imaging experiments, the samples were adhered on a glass plate for facilitating the operation. All measurements were carried out at room temperature. The experimental setup is shown in Figure 6.1.

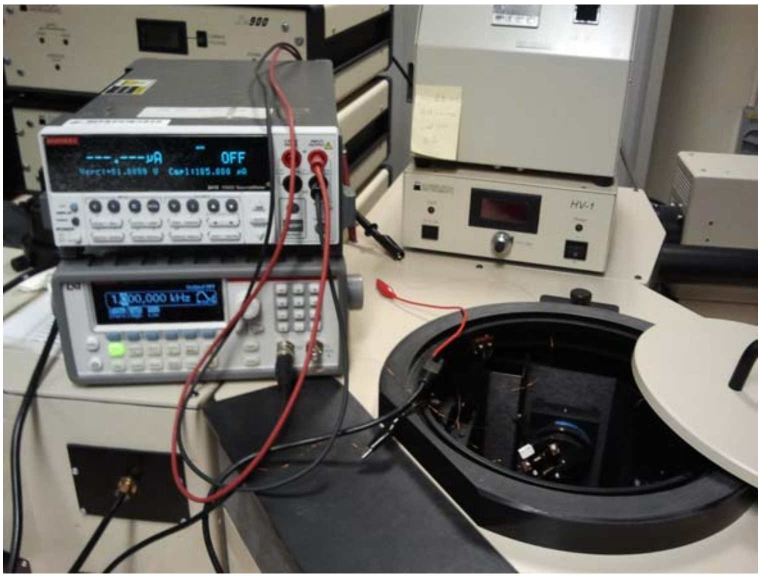

Figure 6.1. Experimental setup for strain-mediated light emission from ZnS:Mn/PMN-PT Structure.

## 6.3 Results and Discussion

The basic strategy for the fabrication of integrated source combining luminescent and ultrasonic characteristics is shown in Figure 6.2. ZnS:Mn selected here is a commonly used phosphor layer in alternating current thin-film electroluminescent (AC-TFEL) devices [Thomas, 1993; Wood, 2009]. The wurtzite-type $Mn^{2+}$ doped ZnS can also possess a non-central symmetric structure and inherently exhibit the piezoelectric characteristics. The piezoelectric potential has been proven to be capable of modifying the band structure significantly in the presence of strain. Analogously, the piezoelectric potential can be induced by the strain from a PMN-PT substrate as shown in Figure 6.2, which is regarded as the fuse to trigger the luminescent center $Mn^{2+}$. The commercial ferroelectric (001)-oriented PMN-PT single crystal (Hefei Kejing Material Technology CO., LTD.) was chosen as substrate due to its outstanding ferroelectric polarization and converse piezoelectric effects [Zhang, 2003].

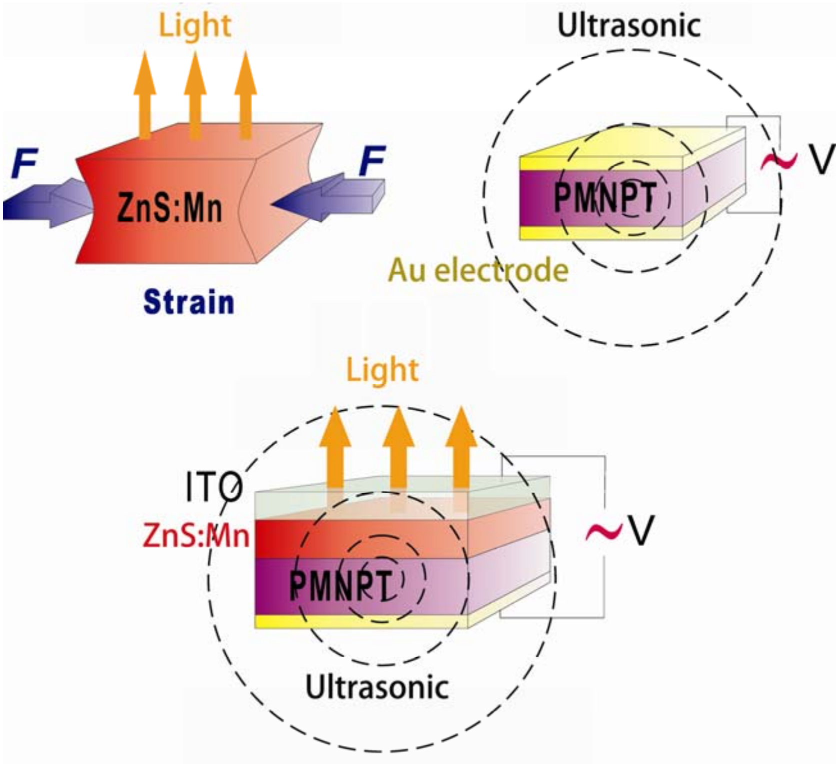

Figure 6.2. The setup used for measuring the luminescent and ultrasonic characteristics of ZnS:Mn film grown on PMN-PT substrate under an ac electric-field.

The ZnS:Mn thin film was grown on PMN-PT by pulsed laser deposition. The X-ray diffraction (XRD) pattern of the ZnS:Mn film on PMN-PT substrate is shown in Figure 6.3. Only (00*l*) diffraction peaks were observed in a wide angle range from $20^{o}$ to $70^{o}$, indicating the film with a good *c*-axis preferred orientation. The lattice constant *c* is measured to be 6.492 Å, which is larger than that in bulk ZnS, *c* = 6.257 Å, JCPDS#36-1450 (Joint Committee on Powder Diffraction Standards). The lattice expansion in the film may results from the existence of sulphur vacancies in the samples.

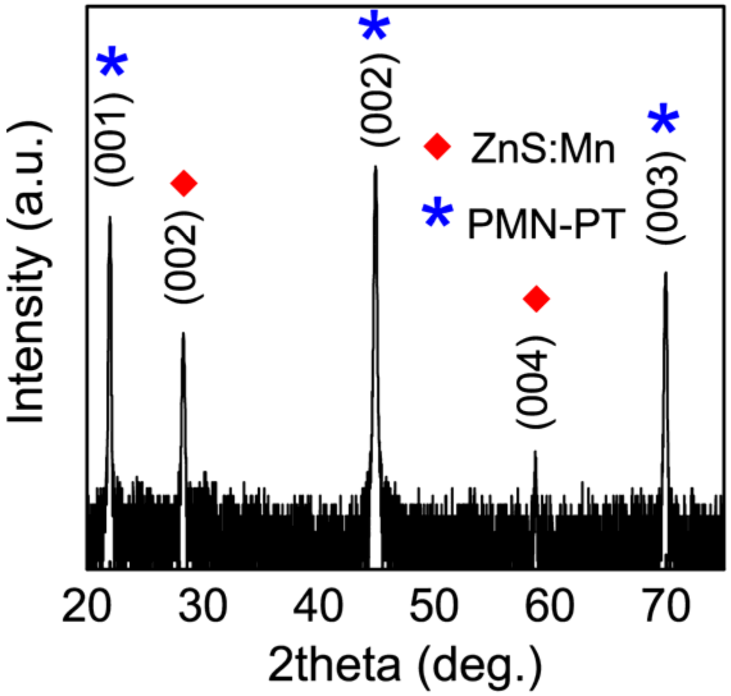

Figure 6.3. XRD $\theta$-$2\theta$ scan of the ZnS:Mn film grown on (001)-oriented PMN-PT single crystal substrate.

To further investigate the microstructure of the ZnS:Mn films on PMN-PT (001), cross-sectional transmission electron microscopy (TEM) studies have been carried out on the interface of the sample. Figure 6.4 is a low-magnification, bright field TEM image of the sample. A transparent electrode of indium tin oxide (ITO) was deposited on top, and emission light can pass through the ITO layer. The thickness of ITO electrode and ZnS:Mn film is about 300 and 600 nm, respectively. The ZnS:Mn film has a smooth surface, uniform thickness, and clearly defined interface with the (001) PMN-PT substrate. The crystallographically textured film is in the form of columnar crystallites with their long axes perpendicular to the substrate.

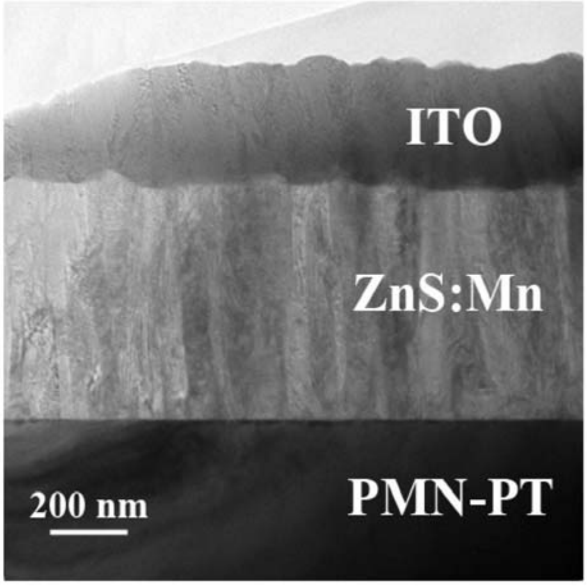

Figure 6.4. Low magnitude bright field TEM image for the interface structures of the ZnS:Mn film grown on PMN-PT substrate. ITO used as top electrode.

Figure 6.5a shows the high-resolution TEM image for the ZnS:Mn/PMN-PT interface of the sample. It is clearly seen that there are some dislocations formed at the interface, and a nanograin of ZnS:Mn formed in the film, confirming the textured crystallization of the film on (001) PMN-PT substrate. A selected area electron diffraction (SAED) pattern taken from both the ZnS:Mn film and PMN-PT substrate along the [010] direction of the ZnS:Mn film is shown in Figure 6.5b. The lattice constant *c* of ZnS:Mn measured from SAED is about 6.37 Å, which is close to the result from XRD. The broaden electron diffraction spots with satellites from ZnS:Mn film indicate the film has a highly preferred orientation and ZnS:Mn has a wurtzite (hexagonal) structure.

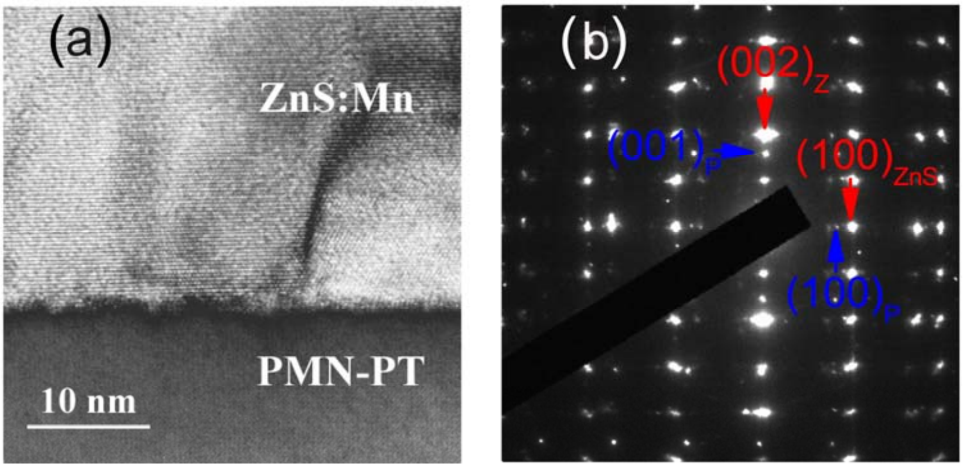

Figure 6.5. (a) High-resolution TEM image for the interface structures of the ZnS:Mn film grown on PMN-PT substrate. (b) SAED pattern.

We applied a positive poling voltage of +500 V across the ZnS:Mn/PMN-PT structure to make the PMN-PT substrate positively polarized. Figure 6.6 shows the normalized light emission spectra of ZnS:Mn film by electric-field operating at 500 Hz and 200 $V_{pp}$. For comparison, photoluminescence (PL) from the ZnS:Mn film is also presented in Figure 6.6. The dominant peak is found at ~588 nm in the electric-field induced emission spectrum of ZnS:Mn, which is similar to the PL spectrum of ZnS:Mn. This indicates that the electric-field induced luminescence also results from the $^4T_1 \rightarrow {}^6A_1$ transition of $Mn^{2+}$. We have investigated the mechanism of the luminescence in ZnS:Mn film on PMN-PT substrate.

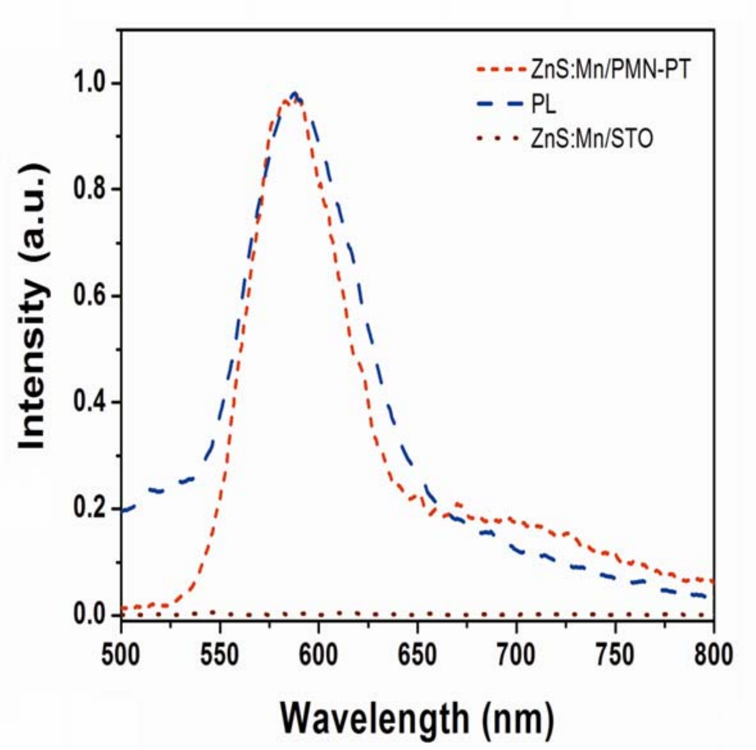

Figure 6.6. The luminescence spectra for structures with PMN-PT and STO insulating substrate operating at 200 $V_{pp}$ and 500 Hz are present by the red dash and brown dot, respectively. A photoluminescence of the sample excited by 320 nm is also demonstrated.

We have investigated the mechanism of the luminescence in ZnS:Mn film on PMN-PT substrate. We deposited ZnS:Mn films on piezoelectric PMN-PT single crystal substrates and *in situ* induced lattice strain on the PMN-PT substrate via its large converse piezoelectric effect. The converse piezoelectric effect (often referred to as inversed piezoelectric effect) describes the relationship between the strain and the applied electric field in piezoelectric materials. The converse piezoelectric effect can be described as the equation:

$$X_i = d_{ki} E_k \tag{6.1}$$

where $X_i$ is the strain tensor, $d_{ki}$ is the piezoelectric tensor, and $E_k$ is the electric field. Such that the equation will lead to the strain in response to an applied field. The polarization of the electrical domain of the measured sample determines the sign of the response. If the polarization is parallel and aligned with the applied electric field, the domains will experience locally expand. Conversely, if the initial polarization is anti-parallel to the applied electric field, the sample will locally shrink. The PMN-PT substrate has been positively polarized prior to the measurements of the luminescent properties of the ZnS:Mn film. When an ac electric field less than the coercive field is applied to the polarized PMN-PT substrate, the lattice of the PMN-PT substrate will expand or contract along the direction of the electric field. Our previous studies have shown that the lattice of the PMN-PT substrate can expand and contract along the *c* axis at the same frequency as that of applied electric field [Zheng, 2006]. The electric-field-induced lattice displacements originate from the converse piezoelectric effect of the PMN-PT substrate. Such a modulation in the lattice parameter *c* will cause changes in the in-plane lattice parameters *a* and *b* as a result of the Poisson effect [Timoshenko, 1987] as shown in Figure 6.7, which can subsequently impose in-plane strains in the ZnS:Mn film. XRD and TEM results indicate that the ZnS:Mn film is of good quality and firmly adheres to the underlying substrate. ZnS:Mn of wurtzite structure possesses non-central symmetric structure. Hence, the substrate-imposed strain can give rise to a piezoelectric potential. Previous researches show that the inner potential in semiconducting materials can modify the band structure for a p-n junction, and consequently influence the light emission performance. However, the structure of p-n junction is not applicable to ZnS:Mn/PMN-PT sample, as PMN-PT single crystal is an insulator with high resistance and permittivity. The inner-crystal potential can trigger the creation of an electron-hole pair, exciting an electron to escape from the valence band and reach the conduction band. Two excitation mechanisms for the $Mn^{2+}$ are possible from our observation. In some literature [Hoshiba, 1980], $Mn^{2+}$ ions were observed more likely hole attractive. Hence, the $Mn^{2+}$ may first trap a hole and subsequently recombine with the electron in the conduction band, resulting in $Mn^{2+}$ in an excited state. While the $Mn^{2+}$ returns from the excited state to ground state, an orange light is emitted [Suyver, 2001]

$$Mn^{2+} + h^{+}(VB) \rightarrow Mn^{3+}$$

$$Mn^{3+} + e^{-} \rightarrow (Mn^{2+})^{*}$$

$$(Mn^{2+})^{*} \rightarrow Mn^{2+} + h\nu$$

Alternatively, the electrons of the conduction band can directly couple with the hole to form an exciton. The exciton is then bound to $Mn^{2+}$. Subsequent recombination of the exciton promotes the $Mn^{2+}$ to the excited state and is followed by the light emission. It is evident that the strain-induced piezoelectric potential plays a crucial role in the observed luminescence of ZnS:Mn. Luminescence based on piezo-phototronic effect and conventional AC-TFEL suffer some similar physical processes, such as the impact excitation of the luminescent center and the de-excitation of the excited luminescent dopant ions. The essential difference between the two types of luminescence is the trigger fuse for these two physical phenomena.

Conventional AC-TFEL is generated from electrons across interface between the phosphor and insulator layer. The electrons are accelerated by external electric-field and excite the luminescent center or host lattice. While in our experiment, the piezoelectric potential originates from the substrate-imposed strain on the piezoelectric host which de-traps the electron in the valence band, and goes with the following processes.

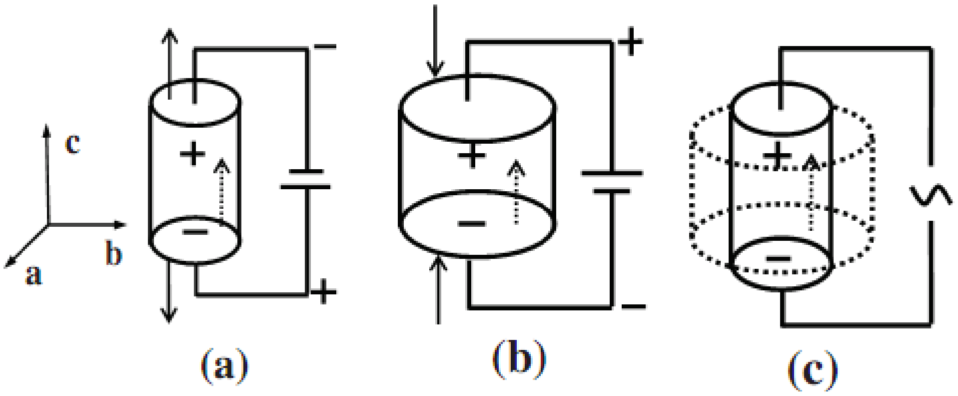

Figure 6.7. Schematic diagrams showing the electric-field-induced elongation, compression, and vibration of the lattice of PMN-PT substrate via the converse piezoelectric effect. The dotted arrows represent the direction of the polarization [Zheng, 2006].

To confirm the hypothesis, a non-piezoelectric insulator strontium titanate (STO) substitutes PMN-PT as substrate sandwiched between both ZnS:Mn and bottom Au electrode. It was found that no obvious luminescence was observed from this sample (Figure 6.6), as expected. It indicates that our observed luminescence indeed originates from the piezoelectric potential stimuli, differing from conventional AC-TFEL. Some researchers have reported that ceramics or nanoparticles can emit luminescence under mechanical stress, friction and strike [Wang, 2005b; Chandra, 2010]. This macroscopic mechanical stimuli induced luminescence is termed mechanoluminescence. Apparently, it is relatively difficult to control the generation of strain from mechanical stress, friction and strike. However, the utilization of piezoelectric PMN-PT substrate in this work provides an effective and precise approach to control over a range of strain state of the thin-films and therefore can realize strain-mediated luminescence. Furthermore, the electric-field-controlled luminescence from the ZnS:Mn/PMN-PT thin-film configuration has the potential in developing integrated devices.

Figure 6.8 shows the transient luminescence of the thin-film sample stimulated under a square electric-voltage. The observation confirms that the strain-induced luminescence is essentially a dynamic process when a time varying voltage is applied. Pulsed emissions were observed to response the transient voltages. The piezoelectric potential created by strain in the ZnS:Mn has a polarity, which may result in the different response of luminescence at the rising and falling edges.

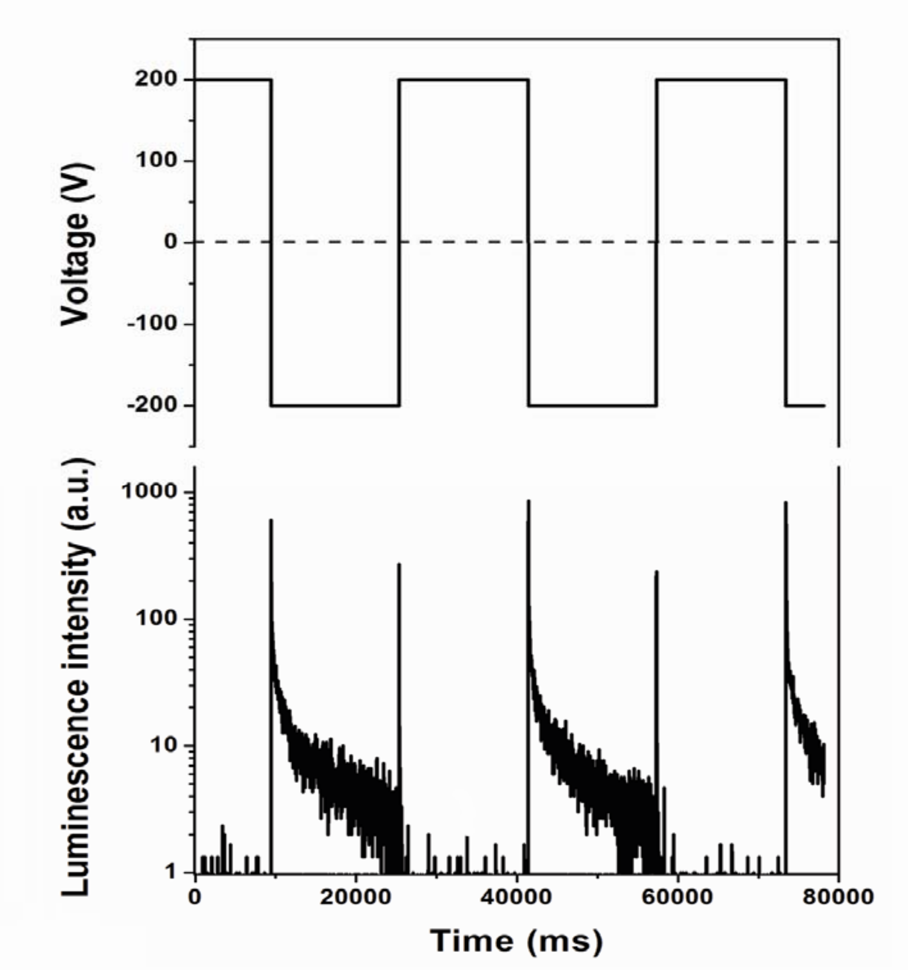

Figure 6.8. Square ac electric voltage applied to the ITO/ZnS:Mn/PMN-PT structure (top), and the luminescence at a wavelength 586 nm as a function of time while the square ac electric field is applied (bottom).

Figures 6.9a and 6.9b show the luminescent intensity as a function of applied voltage and frequency. So, we can realize the tuning of emission intensity of ZnS:Mn thin-film in an *in situ* and real-time manner by applying an ac electric field across the PMN-PT substrate, similar to our recent report regarding to electric-field-modulated PL.

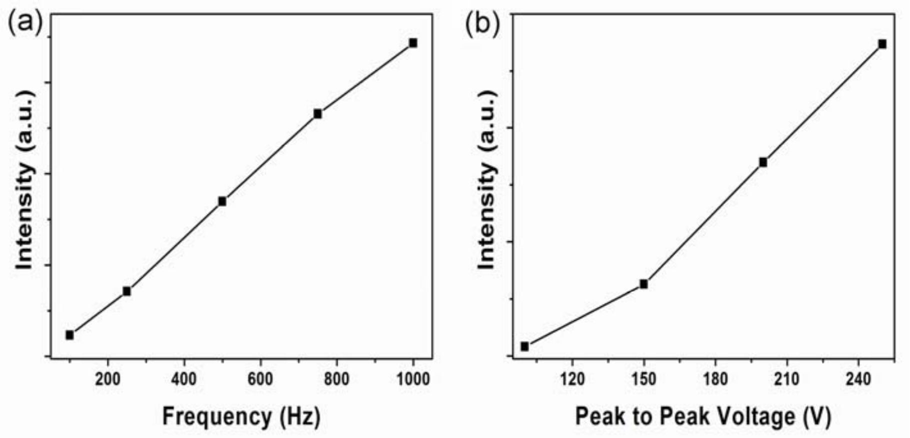

Figure 6.9. (a) The luminescence response as a function of frequency at 200 $V_{pp}$. (b) The luminescence response as a function of voltage at 500 Hz.

The photographs in Figure 6.10 illustrate the obvious luminescence from ZnS:Mn film (1 mm × 1 mm pixel) grown on PMN-PT substrate applied with different applied voltages at 500 Hz. An orange light emission can be observed by the naked eye.

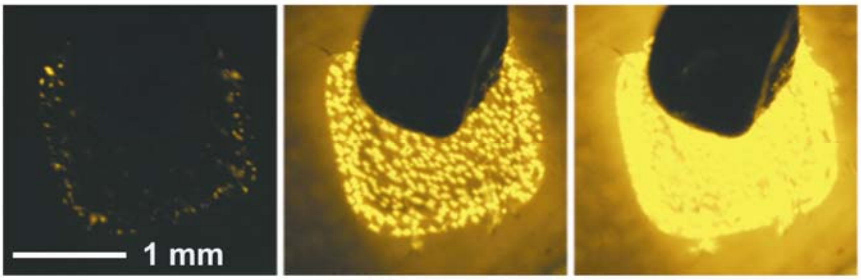

Figure 6.10. Light emission photographs of 1 mm × 1 mm ZnS:Mn film fabricated on PMN-PT substrate operating with peak to peak voltages of 50 V, 100 V, and 200 V, respectively, under the same applied frequency of 500 Hz (left to right).

Regardless of the vibration systems, resonance always results in a greater amplitude. Resonance is expected to be able to produce intense luminescence under relatively low voltages. So, further analysis was performed to characterize the luminescence of ZnS:Mn on PMN-PT under high frequency vibration stimuli. Figure 6.11 shows the luminescence as a function of frequency when sinusoidal voltage is applied on PMN-PT. The samples were adhered on a glass plate for facilitating the operation during the luminescence measurement. The intensity of luminescence shows strong dependence on the voltage frequency. The inset is the emission spectra of the ZnS:Mn film taken under an applied voltage of 10 $V_{pp}$ at 650 kHz. The spectral profile in terms of curve shape and peak position is almost same as the observed luminescence under low frequency stimuli. Strong frequency dependent luminescence from ZnS:Mn/PMN-PT system indicates that the resonance occurs at its nature frequency. When the PMN-PT substrate is excited by an applied voltage at its natural resonance frequencies, larger vibration amplitude occurs. Along with the fundamental plate mode resonance (~ 650 kHz) and the thickness mode resonance (~ 5.20 MHz), as well as their harmonics, there also appeared some minor resonances originated from the sample configuration (Figure 6.11). All these resonances of PMN-PT could lead to emission peaks from ZnS:Mn. Based on the observation on the frequency dependent luminescence, we suggest that PMN-PT working at a resonant frequency can greatly promote the emission. The frequency dependent results further rule out the probability of conventional AC-TFEL. In contrast to conventional AC-TFEL devices, the obtained luminescent device in this work can operate at high frequency up to MHz.

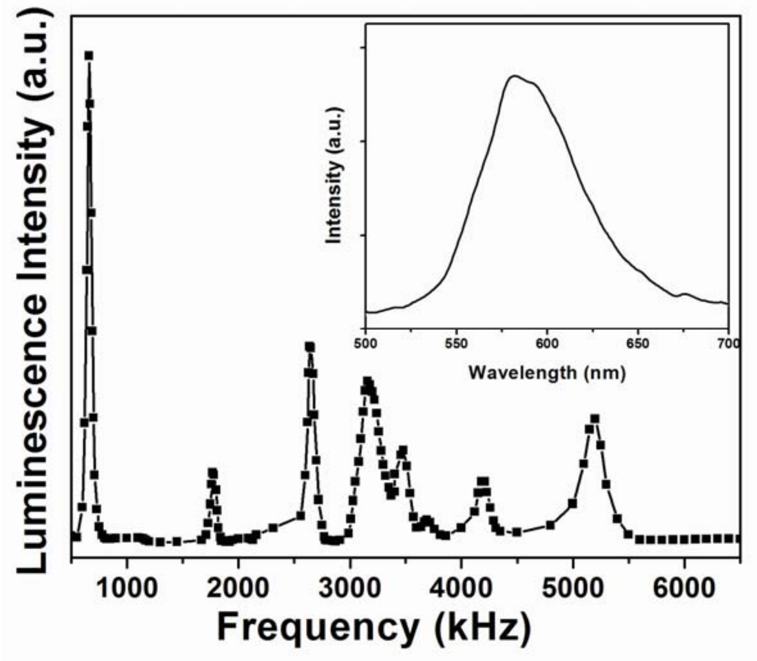

Figure 6.11. Frequency dependence of the luminescence intensity for ZnS:Mn film under the applied voltage 10 $V_{pp}$. Inset shows the luminescence spectra of ZnS:Mn operating at 650 kHz and 10 $V_{pp}$.

The above result provides a clue that it is possible to realize on-chip multi-mode sensor/source integrated thin-film phosphors with piezoelectric materials after the observation of light emission from ZnS:Mn film by external applied voltage via the converse piezoelectric effect. Many imaging technologies including optical imaging and ultrasonic imaging, are capable of providing various information on anatomical structure or composition. But each imaging modality has its own merits and application limitations. Great efforts have been focused on the development of multi-modal imaging system [Sun, 2009; Zhang, 2011b]. There have been reports on dual-modal diagnostic devices combining optical and ultrasonic imaging, i.e. a hybrid system combines an optical fiber and an ultrasonic transducer. It would be attractive if a single source combined with light and ultrasound generation could be produced. To validate the feasibility of the novel signal source, the ZnS:Mn/PMN-PT structure was poled along the thickness direction and the test signal was also applied along same direction. The performance of the transducer was tested using a pulse-echo response arrangement as shown in Figure 6.12.

Figure 6.12. Experimental setup for ultrasound measurement.

Figure 6.13a shows the impedance and phase spectra of the sample with PMN-PT thickness of 0.5 mm as a function of frequency in a frequency range from 0.5 MHz to 30 MHz. It can be seen that the plate mode resonance is found at ~750 kHz. The thickness mode resonance frequency ($f_r$) and the anti-resonance frequency ($f_a$)

can be observed at 5.25 MHz and 6.05 MHz, respectively. The thickness electromechanical coupling coefficient $k_t$ can be derived from [Zhou, 2011]

$$k_t^2 = \frac{\pi}{2}\frac{f_r}{f_a}\tan\left(\frac{\pi}{2}\frac{f_a - f_r}{f_a}\right) \tag{6.2}$$

$k_t$ is found to be 0.53. Figure 6.13b shows a pulse-echo waveform and frequency spectrum of the PMN-PT coated with ZnS:Mn film. The center frequency of the structure was found to be about 5.48 MHz, which falls into the range of ultrasonic frequency for medical diagnostic. The fractional bandwidth at -6 dB was measured to be around 16.6%. There is plenty room to improve the performance by optimizing the fabrication technology. At any rate, the results are indicative of the dual-functions, i.e. light source and ultrasound transducer in the device structure of ZnS:Mn thin films grown on PMN-PT.

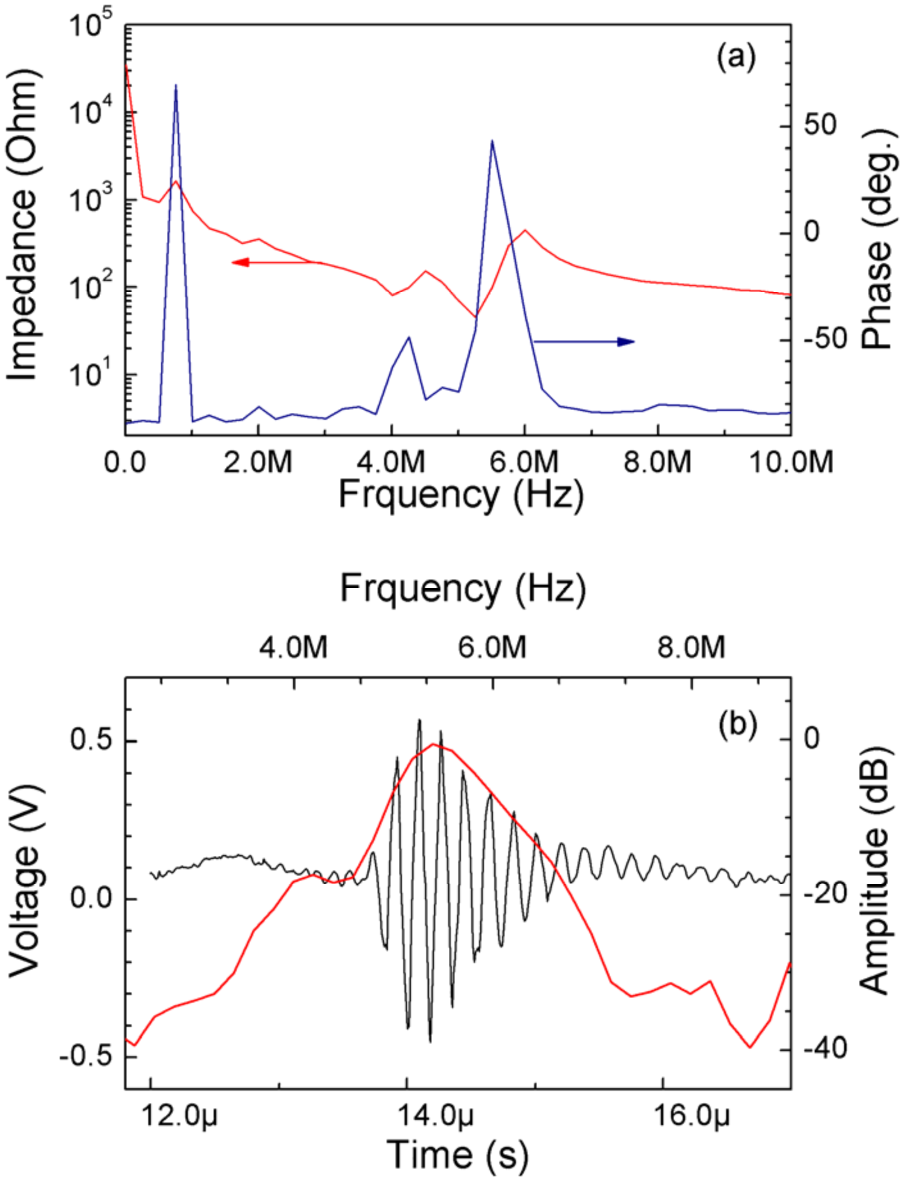

Figure 6.13. (a) The thickness mode impedance and phase spectra for the PMN-PT single crystal. (b) Pulse-echo waveform and frequency spectrum for PMN-PT coated with ZnS:Mn film.

## 6.4 Conclusion

In this chapter, we have demonstrated electric-field-controllable luminescence of ZnS:Mn grown on piezoelectric PMN-PT substrate. The light emission of the ZnS:Mn arises from the piezoelectric potential, resulting from the converse piezoelectric effect of PMN-PT substrate. Such a novel light source can be controlled by high-frequency electric-field up to MHz. Moreover, simultaneous generation of light and ultrasound wave is observed using a single ZnS:Mn/PMN-PT system. The observed phenomena can be used to develop a dual-modal source combing light and ultrasonic signal for a variety of applications.

# Chapter 7 Conclusions and Suggestions for Future Work

## 7.1 Conclusions

The present research focused on the investigation of optical properties and modulation of metal ions doped phosphors. The main conclusions can be summarized as follows:

1. With an increasing in $Er^{3+}$ doping concentration, Photoluminescence (PL) quenching of $Er^{3+}$-doped $BaTiO_3$ (BTO) is ascribed to the worse crystalline and cross-relaxation process, i.e. $^2H_{11/2}$ + $^4I_{15/2}$ → $^4I_{9/2}$ + $^4I_{13/2}$. The abnormal jump in PL intensity across the phase transition for A-site substitution $Er^{3+}$-doped BTO contributed to the crystal field changed induced by the phase transition. For the case of B-site substitution $Er^{3+}$-doped BTO, $^4S_{3/2}$ → $^4I_{15/2}$ emissions are strongly enhanced due to thermal quenching and lower symmetry induced by phase transition.

2. For $Yb^{3+}/Er^{3+}$ co-doped BTO, $Yb^{3+}/Er^{3+}/Tm^{3+}$ tri-doped BTO phosphors, $Yb^{3+}$ ions acting as a sensitizer had a great influence on the upconversion emission of phosphors. The emission intensity balances were changed

through control of the concentrations of doped ions. Meantime, the $^5D_0 \rightarrow {}^7F_n$ PL spectra of $Eu^{3+}$ were studied. The magnetic and electric dipole transitions of $Eu^{3+}$ may be used to detect the structural asymmetry.

3. We have demonstrated that the enhancement and modulation of upconversion PL can be realized by applying low voltages to BTO: Yb/Er thin films in an *in-situ* and real-time manner. The emission intensity of main green band of epitaxial BTO:Yb/Er thin film under the bias voltage at 10 V is almost 2.7 times as that of the unbiased one. The observed phenomena can be ascribed to the increase in the radiative transition probabilities resulting from the lower symmetry of $Er^{3+}$ sites which arises when an external electric field is applied.

4. The PL intensity of the BTO:Yb/Er can be modulated with ac electric field. It is found that the PL intensity of the BTO:Yb/Er thin film can be modulated with the same frequency as that of the applied electric field.

5. Strain-mediated light emission was generated from ZnS:Mn grown on piezoelectric PMN-PT substrate. The light emission of the ZnS:Mn arises from the piezoelectric potential, resulting from the converse piezoelectric effect of PMN-PT substrate. Such a novel light source can be controlled by high-frequency electric-field up to MHz.

6. Simultaneous generation of light and ultrasound wave is observed using a single ZnS:Mn/PMN-PT system. The center frequency of the structure was found to be about 5.48 MHz, which falls into the range of ultrasonic frequency. The observed phenomena can be used to develop a dual-modal source combing light and ultrasonic signal for a variety of applications.

## 7.2 Suggestions for Future Work

This thesis focuses on studying optical properties and pursuing the ability to tune the spectral properties of f metal ions doped phosphors. There is plenty room needing further research. The following are some suggestions for further research which may be regarded as an extension of the present work.

1. Temperature dependence of the PL in $Er^{3+}$-doped BTO has implied that the emission from substituted rare-earth ions may be used as a structural probe for the ferroelectric titanates. Compared with rare-earth, transition metals where the unfilled 3d shell is not as well screened due to only a single outer shell. Transition metals are, therefore, strongly coupled to the host lattice. In future work, it is necessary to investigate the relationship between the PL spectra of transition metal and the ferroelectric phase transition.

2. We have proposed a new approach for the modulation of upconversion emission through applying relatively low voltage to Yb/Er co-doped BTO

thin films in an *in-situ* and real-time manner. This result naturally leads us to consider whether our method is applicable to other rare-earth ions. Trivalent rare-earth ions, such as $Eu^{3+}$, $Tm^{3+}$, $Ho^{3+}$, and $Pr^{3+}$, are common activator ions. All of these ions possess hypersensitive transitions. So in future work, the investigation on the electric-induced modulation of the phosphors doped with other rare-earth ions will be conducted.

3. The ability to tune the color output of phosphors is of considerable interest for applications. Previous studies have shown the tri-doped ($Yb^{3+}$/$Er^{3+}$/$Tm^{3+}$) systems can emit tunable color output from blue to white by variation of the dopant concentrations. By reviewing references concerned and referring to the results of our research, it is promising to realize reversible-tuning the emission colors by applying low voltages to Yb/Er/Tm tri-doped BTO thin films.

4. We have demonstrated strain-mediated luminescence from ZnS:Mn grown on piezoelectric PMN-PT substrate controlled by electric-field. PMN-PT single crystal exhibits excellent piezoelectric activity and has a perovskite structure with lattice constants ($a = b = c = 0.402$ nm), which are close to those of BTO ($a = 0.399$ nm, $c = 0.403$ nm) and $CaTiO_3$ ($a = b = c = 0.380$ nm). High electrostrictive strain, mechanoluminescence, and electroluminescence have been observed in the $[(1-x)BaTiO_3-xCaTiO_3]$:Pr ($x=0.25-0.30$) (BCTO:Pr) ceramics. Compared with ZnS:Mn, BCTO:Pr has

a smaller lattice constant mismatch with PMN-PT substrate. So we can successfully grow epitaxial BCTO:Pr thin films on PMN-PT substrates, and larger strain state of these films can be reversibly controlled via the converse piezoelectric effect of the substrates.

5. Simultaneous generation of light and ultrasound wave has been observed in ZnS:Mn/PMN-PT system, offering a great potential in developing a dual-modal source combing light and ultrasonic wave for various applications such as hybrid system for medical imaging. However, there is plenty room to improve the performance by improving the fabrication technology. Such as adding the backing layer to eliminate the back-wall reflections and reduce the ring-down time of the transducer. In future, we will cooperate with other researchers to optimize the performance of the dual-modal source.

# References

Adachi, D., Haze, H., Shirahase, H., Toyama, T., and Okamoto, H., *J. Non-Cryst. Solids*, **35**, 1628, 2006.

Aebischer, A., Hostettler, M., Hauser, J., Kramer, K., Weber, T., Güdel, H. U., and Bürgi, H. B., *Angew. Chem. Int. Ed.* **45**, 2802, 2006.

Ahn, C. H., Rabe, K. M., and Triscone, J. M., *Science,* **303**, 488, 2004.

Alexe, M., Kästner, G., Hesse, D., and Gösele, U., *Appl. Phys. Lett.* **70**, 3416, 1997.

Auzel, F., *C. R. Acad. Sci. Paris.* **262**, 1016, 1966.

Auzel, F., *Chem. Rev.* **104**, 139, 2004.

Bai, X., Song, H., Pan, G., Lei, Y., Wang, T., Ren, X., Lu, S., Dong, B., Dai, Q., and Fan, L., *J. Phys. Chem. C* **111**, 13611, 2007.

Balakrishnaiah, R., Kim, D. W., Yi, S. S., Kim, K. D., Kim, S. H., Jang, K., Lee, H. S., and Jeong, J. H., *Thin Solid Films* **517**, 4138, 2009.

Barnes, N. P., Walsh, B. M., F. Amzajerdian, F., Reichle, D. J., Busch, G. E., and Carrion, W. A., *Opt. Mater. Express***,** **1**, 678, 2011.

Bartolo, B. D., and Forte, O., *Advanced in Spectroscopy for Lasers and Sensing***,** Springer, Netherlands, 2006.

Basurto, G., and Burshtein, J. Z., *Mol. Cryst. Liq. Cryst.* **31**, 211, 1975.

Binnig, G., Quate, C. F., and Gerber, C. H., *Phys. Rev. Lett.* **56**, 930, 1986.

Blasse, G., and Grabmaier, B. C., *Luminescent Materials*, Springer-Verlag, Berlin, 1994.

Blasse, G., and Bril, A., *J. Chem. Phys.* **50**, 2974, 1969.

Bloembergen, N., *Phys .Rev. Lett.* **2**, 84, 1959.

Boyer, J. C., Cuccia, L. A., and Capobianco, J. A., *Nano. Lett.* **7**, 847, 2007.

Broer, L. F. J., Gorter, C. J., and Hoogschagen, J., *Physica* **11**, 231, 1945.

Buscaglia, M. T., Buscaglia, V., Viviani, M., Nanni, P., and Hanuskova, M., *J. Eur. Ceram. Soc.* **20**, 1997, 2000.

Buscaglia, M. T., Viviani, M., Buscaglia, V., Bottino, C., and Nanni, P., *J. Am. Ceram. Soc.* **85**, 1569, 2002.

Camargo, A. S. S., Botero, E. R., Andreeta, E. R. M., Garcia, D., and Eiras, J. A., *Appl. Phys. Lett.* **86**, 241112, 2005.

Carnall, W. T., Fields, P. R., and Rajnak, K., *J. Chem. Phys.* **49**, 4424, 1968.

Carnall, W. T., Goodman, G. L., Rajnak, K., and Rana, R. S., *J. Chem. Phys.* **90**, 3443, 1989.

Cha, S. N., Seo, J. S., Kim, S. M., Kim, H. J., Park, Y. J., Kim, S. W., and Kim, J. M., *Adv. Mater.* **22**, 4726, 2010.

Chandra, B. P., Xu, C. N., Yamada, H., and Zheng, X. G., *J. Lumin.* **130**, 442, 2010.

Chatterjee, D. K., Rufaihah, A. J., and Zhang, Y., *Biomaterials*, **29**, 937, 2008.

Chatterjee, D. K., Gnanasammandhan, M. K., and Zhang, Y., *Small*, **6**, 2781, 2010.

Chen, G., Haire, R. G., and Peterson, J. R., *Appl. Spectrosc.* **46**, 273, 1992.

Chen, G. Y., Somesfalean, G., Liu, Y., Zhang, Z. G., Sun, Q., and Wang, F. P., *Phys .Rev. B* **75**, 195204, 2007.

Chivian, J. S., Case, W. E., and Eden, D. D., *Appl. Phys. Lett.* **35**, 124, 1979.

Choi, T., Lee, S., Choi, Y. J., Kiryukhin, V., and Cheong, S. W., *Science,* **324**, 63, 2009.

Chrisey, D. B., and Hubler, G. K., *Pulsed Laser Deposition of Thin Films*, John Wiley & Sons, New York, 1994.

Chung, K., Lee, C. H., and Yi, G. C., *Science,* **330**, 655, 2010.

Cotton, F. A., Wilkinson, G., *Advanced Inorganic Chemistry*, John Wiley & Sons, New York, 1988.

Damjanovic, D., *Rep. Prog. Phys.* **61**, 1267, 1998.

Daniels, J. E., Jo, W., Rödel, J., and Jones, J. L., *Appl. Phys. Lett.* **95**, 032904, 2009.

Destriau, G., *J. Chim. Phys.* **33**, 620, 1936.

Dierolf, V., Sandmann, C., Kim, S., Gopalan, V., and Polgar, K., *J. Appl. Phys.* **93**, 2295, 2003.

Dobal, P. S., and Katiyar, R. S., *J. Raman Spectrosc.* **33**, 405, 2002.

Doering, R., and Yoshio, N., *Handbook of semiconductor manufacturing technology*, CRC Press, 2008.

Dunbar, T. D., Warren, W. L., Tuttle, B. A., Randall, C. A., and Tsur, Y., *J. Phys. Chem. B* **108**, 908, 2004.

Feofilov, S. P., Kaplyanskii, A. A., Kulinkin, A. B., Zakharchenya, R. L., *Phys. Stat. Sol.***4**, 705, 2007.

Fluckiger, U., Arend, H., and Oswald, H. R., *J. Am. Ceram. Soc.* **56**, 575, 1977.

Ganeev, R. A., Suzuki, M., Baba, M., Ichihara, M., and Kuroda, H., *J. Opt. Soc. Am. B* **25**, 325, 2008.

Gao, F., Wu, G. H., Zhou, H., and Bao, D. H., *J. Appl. Phys.* **106**, 126104, 2009.

Garcia, V., Bibes, M., Bocher, L., Valencia, S., Kronast, F., Crassous, A., Moya, X., Enouzvedrenne, S., Gloter, A., Imhoff, D., Deranlot, C., Mathur, N. D., Fusil, S., Bouzehouane, K., and Barthelemy, A., *Science,* **327**, 1106, 2010.

Güdel, H. U., *Topics in Current Chemistry*, Springer, New York, 2001.

Guo, E. J., Gao, J., and Lu, H. B., *Appl. Phys. Lett.* **98**, 081903, 2011.

Guo, H., Dong, N., Yin, M., Zhang, W. P., Lou, L. R., and Xia, S. D., *J. Alloys Compd.* **415**, 280, 2006.

Haase, M., and Schäfer, H., *Angew. Chem. Int. Ed.* **50**, 5808, 2011.

Hakala, R. W., *J. Chem. Educ.* **29**, 581, 1952.

Hänninen, P., and Härmä, H., *Lanthanide Luminescenc: Photophysical, Analyitical and Biological Aspects*, Springer, Berlin, 2011.

Hao, J. H., Studenikin, S. A., and Cocivera, M., *J. Appl. Phys.* **90**, 5064, 2001.

Hao, J. H., Lou, Z. D., Renaud, I., and Cocivera, M., *Thin Solid Films* **467**, 182, 2004.

Hao, J. H., Gao, J., Wang, Z., and Yu, D. P., *Appl. Phys. Lett.* **87**, 131908, 2005.

Hartree, D. R., *The Calculation of Atomic Structures*, John Wiley & Sons, New York, 1957.

Heer, S., Lehmann, O., Haase, M., and Güdel, H. U., *Angew. Chem. Int. Ed.* **42**, 3179, 2003.

Heer, S., Kömpe, k., Güdel, H. U., and Haase, M., *Adv. Mater.* **16**, 2102, 2004.

Holonyak, N., and Bevacqua, S. F., *Appl. Phys. Lett.* **1**, 82, 1962.

Hoshiba, T., and Kawai, H., *Jpn, J. Appl. Phys.* **19**, 267, 1980.

Hu, Y. F., Zhang, Y., Xu, C., Zhu, G., and Wang, Z. L., *Nano Lett.* **10**, 5025, 2010.

Huang, J. M., Yang, Y., Xue, S. H., Yang, B., Liu, S. Y., and Shen, J. C., *Appl. Phys. Lett.* **70**, 118866, 1997.

Huang, T. C., and Hsieh, W. F., *J. Fluoresc.* **19**, 511, 2009.

Humphreys, C. J., *MRS Bulletin* **33**, 459, 2008.

Hwang, J. H., and Han, Y. H., *Jpn. J. Appl. Phys.* **40**, 676, 2001.

Igonuchi, T., Takeda, M., Kanatani, Y., Nakata, Y., and Yoshida, M., *SID '74 Digest*, 1974.

Ihanus, J., Lankinen, M. P., Kemell, M., Ritala, M., and Leskelä, M., *J. Appl. Phys.* **98**, 113526, 2005.

Ishii, M., Komuro, S., Morikawa, T., and Aoyagi, Y., *J. Appl. Phys.* **89**, 3679, 2001.

Jezowski, A., Mucha, J., Pazik, R., and Strek, W., *Appl. Phys. Lett.* **90**, 114104, 2007.

Jiang, C. G., Fang, L., Shen, M. R., Zheng, F. G., and Wu, X. L., *Appl. Phys. Lett.* **94**, 071110, 2009.

Joshi, P. C., and Desu, S. B., *Thin Solid Films* **300**, 289, 1997.

Judd, B. R., *Phys .Rev.* **127**, 750, 1962.

Kondo, M., Maruyama, K., and Kurihara, K., *FUJITSU Sci. Tech. J.* **38**, 46, 2002.

Kotera, Y., *J. Jpn. Soc. Color. Mater.* **58**, 80, 1985.

Kramer, B., *Advances in Solid State Physics*, Springer, Berlin, 2003.

Kramer, K. W, Biner, D., Frei, G., Güdel, H. U., Hehlen, M. P., and Luthi, S. R., *Chem. Mater.* **16**, 1244, 2004.

Krupka, D. C., and Mahoney, D. M., *J. Appl. Phys.* **43**, 2314, 1972.

Krupke, W. F., *Phys .Rev.* **145**, 325, 1966.

Kuo, S. K., and Hsieh, W. F., *J. Vac. Sci. Technol. A* **23**, 768, 2005.

Kwon, S. S., Hong, W. K., Jo, G., Maeng, J., Kim, T. W., Song, S., and Lee, T., *Adv. Mater.* **20**, 4557, 2008.

Lim, S. F., Riehn, R., Ryu, W. S., Khanarian, N., Tung, C. K., Tank, D., and Austin, R. H., *Nano. Lett.* **6**, 169, 2006.

Liu, G. K., and Jacquier, B., *Spectroscopic Properties of Rare Earths in Optical Materials*, Springer, Berlin, 2005.

Liu, Y. X., Pisarski, W. A., Zeng, S. J., Xu, C. F., and Yang, Q. B., *Opt. Express*, **17**, 9089, 2009.

Lu, H. Y., and Chu, S. Y., *J. Cryst. Growth* **265**, 476, 2004.

Mai, H. X., Zhang, Y. W., Sun, L. D., and Yan, C. H., *J. Phys. Chem. C* **111**, 13730, 2007.

Makishima, S., Hasegawa, K., and Shionoya, S., *J. Phys. Chem. Solids* **23**, 749, 1962.

Makishima, S., Yamamoto, H., Tomotsu, T., and Shionoya, S., *J. Phys. Soc. Jpn.* **20**, 2147, 1965.

Mitic, V. V., Nikolic, Z. S., Pavlovic, V. B., Paunovic, V., Miljkovic, M., Jordovic, B., and Zivkovic, L., *J. Am. Ceram. Soc.* **93**, 132, 2010.

Mito, S., Suzuki, C., Kanatani, Y., and Ise, M., *Digest of 1974 SID International Symposium*, 1974.

Na, E., Choi, S. C., and Paik, U., *J. Ceram. Process. Res.* **4**, 181, 2003.

Nakamura, S., Mukai, T., and Senph, M., *Appl. Phys. Lett.* **64**, 1687, 1994.

Noginov, M. A., and Loutts, G. B., *J. Opt. Soc. Am. B* **16**, 3, 1999.

Ofelt, G. S., *J. Chem. Phys.* **37**, 511, 1962.

Oliveira, A. S., De Araujo, M. T., Gouveia-Neto, A. S., Medeiros Neto, J. A., Sombra, A. S. B., and Messaddeq, Y., *Appl. Phys. Lett.* **72**, 753, 1998.

Ouyang, X., Kitai, A. H., and Xiao, T., *J. Appl. Phys.* **79**, 3229, 1996.

Pan, Y. X., and Liu, G. K., *Opt. Lett.* **33**, 1816, 2008.

Patra, A., Friend, C. S., Kapoor, R., and Prasad, P. N., *Chem. Mater.* **15**, 3650, 2003.

Peng, A. H., Xie, E. Q., Jia, C. W., Jiang, R., and Lin, H. F., *Mater. Lett.* **59**, 3866, 2005.

Peng, J., Lau, S. T., Chao, C., Dai, J. Y., Chan, H. L. W., Luo, H. S., Zhu, B. P., Zhou, Q. F., and Shung, K. K., *Appl. Phys. A* **98**, 233, 2010.

Pimputkar, S., Speck, J. S., Denbaars, S. P., and Nakamura, S., *Nat. Photon.* **3**, 180, 2009.

Polman, A., *Physica B* **300**, 78, 2001.

Raman, C. V., and Krishnan, K. S., *Nature*, **121**, 501, 1928.

Russ, M. J., and Kennedy, D. I., *J. Electrochem. Soc.* **114**, 1066, 1967.

Sawyer, C. B., and Tower, C. H., *Phys .Rev.* **35**, 269, 1930.

Schietinger, S., Aichele, T., Wang, H. Q., Nann, T., and Benson, O., *Nano Lett.* **10**, 134, 2010.

Schlaghechen, J., Gottmann, J., Kreutz, E. W., and Poprawe, R., *Appl. Phys. A* **79**, 1255, 2004.

Strukov, B. A., and Levanyuk, A. P., *Ferroelectric Phenomena in Crystals: Physical Foundations*, Springer, Berlin, 1998.

Shanker, V., Tanaka, S., Shiiki, M., Geguchi, H., Kobayashi, H., and Sasakura, H., *Appl. Phys. Lett.* **45**, 960, 1984.

Shao, M., Yan, L., Pan, H. P., Ivanov, I., and Hu, B., *Adv. Mater.* **23**, 2216, 2011.

Shinar, J., *Organic Light-emitting Devices: A Survey*, AIP Press/Springer, New York, 2004.

Stolichnov, I., Riester, S. W. E., Trodahl, H. J., Setter, N., Rushforth, A. W., Edmonds, K. W., Campion, P. R., Foxon, C. T., Gallagher, B. L., and Jungwirth, T., *Nat. Mater.* **7**, 464, 2008.

Streicher, K., Plant, T. K., and Wager, J. F., *J. Appl. Phys.* **78**, 2101, 1995.

Sun, Y., Liu, H., Wang, X., Kong, X., and Zhang, H., *Chem. Mater.***18**, 2726, 2006.

Sun, Y., Park, J., Stephens, D. N., Jo, J. A., Sun, L., Cannata, J. M., Saroufeem, R. M. G., Shung, K. K., and Marcu, L., *Rev. Sci. Instrum.* **80**, 065104, 2009.

Suyver, J. F., Wuister, S. F., Kelly, J. J.,and Meijerink, A., *Nano Lett.* **1**, 429, 2001.

Takada, K., Chang, E., and Smyth, D. M., *Adv. Ceram.* **19**, 147, 1987.

Takashima, H., Shimada, K., Miura, N., Katsumata, T., Inaguma, Y., Ueda, K., and Itoh, M., *Adv. Mater.* **21**, 3699, 2009.

Takeda, M., Kanatani, Y., Inoguchi, H., and Okano, K., *Proc. SPIE 386 Advances in Display Technology III*, 1983.

Tanabe, S., Ohyagi, T., Soga, N., and Hanada, T., *Phys .Rev. B* **46**, 3305, 1992.

Tazaki, R., Fu, D., Itoh, M., Daimon, M., and Koshihara, S., *J. Phys, Condens. Matter* **21**, 215903, 2009.

Tenne, D. A., Soukiassian, A., Xi, X. X., Choosuwan, H., Guo, R., and Bhalla, A. S., *Phys. Rev. B* **70**, 174302, 2004.

Thomas, C. B., and Cranton, W. M., *Appl. Phys. Lett.* **63**, 3119, 1993.

Timoshenko, S. P., and Goodier, J. N., *Theory of elasticity*, MacGraw-Hill, New York, 1987.

Tinte, S., and Stachiotti, M. G., *Phys .Rev. B* **64**, 235403, 2001.

Toki, H., Sato, Y., Tamura, K., Kataoka, F., and Itoh, S., *Proc. 3rd Int. Display Workshops*, 1996.

Trupke, T., Green, M. A., and Würfel, P., *J. Appl. Phys.* **92**, 4117, 2002.

Tsur, Y., Hitomi, A., Scrymgeour, I., and Randall, C. A., *Jpn. J. Appl. Phys.* **40**, 255, 2001.

Valiente, R., Wenger, O. S., and Güdel, H. U., *J. Chem. Phys.* **116**, 5196, 2002.

Vasilopoulou, M., Georgiadou, D., Pistolis, G., and Argitis, P., *Adv. Funct. Mater.* **17**, 3477, 2007.

Vecht, A., Smith, D. W., Chadha, S. S., Gibbons, C. S., Koh, J., and Morton, D., *J. Vac. Sci. Technol. B* **12**, 781, 1994.

Vetrone, F., Naccache, R., Zamarrón, A., Fuente, A., Rodriguez, F. S., Maestro, L. M., Rodriguez, E. M., Jague, D., Solė, J. G., and Capobianco, J. A., *ACS Nano* **4**, 3254, 2010.

Vij, D. R., *Handbook of Electroluminescent Materials*, IOP, Bristol, 2004.

Vlasenko, N. A., and Popkov, Z., *Opt. speckrosk.* **8**, 39, 1960.

Vleck, J. H. V., *J. Phys. Chem.* **41**, 67, 1937.

Walters, R. J., Bourianoff, G. I., and Atwater, H. A., *Nat. Mater.* **4**, 143, 2005.

Wang, F., and Liu, X. G., *J. Am. Chem. Soc.* **130**, 5642, 2008a.

Wang, F., and Liu, X. G., *Chem. Soc. Rev.* **38**, 976, 2009.

Wang, F., Han, Y., Lim, C.S., Lu, Y. H., Wang, J., Xu, J., Chen, H. Y., Zhang, C., Hong, M. H., and Liu, X. G., *Nature*, **463**, 1061, 2010 (a).

Wang, L., and Tan, W. H., *Nano Lett.* **6**, 84, 2006a.

Wang, X., Xu, C. N., Yamada, H., Nishikubo, K., and Zheng, X. G., *Adv. Mater.* **17**, 1254, 2005b.

Wang, X. S., Xu, C. N., and Yamada, H., *Jpn. J. Appl. Phys.* **44**, 912, 2005a.

Wang, Z. L., and Song, J. H., *Science,* **312**, 242, 2006b.

Wang, Z. L., *Adv. Mater.* **19**, 889, 2007.

Wang, Z. L., Chan, H. L. W., Li, H. L., and Hao, J. H., *Appl. Phys. Lett.* **93**, 141106, 2008b.

Wang, Z. L., Hao, J. H., and Chan, H. L. W., *J. Mater. Chem.* **20**, 3178, 2010b.

Wang, Z. L., *Nano Today* **5**, 540, 2010c.

Wang, Z. L., Hao, J. H., Chan, H. L. W., Law, G. L., Wong, W. T., Wong, K. L., Murphy, M. B., Su, T., Zhang, Z. H., and Zeng, S. Q., *Nanoscale*, **3**, 2175, 2011.

Warusawithana, M. P., Cen, C., Sleasman, C. R., Woicik, J. C., Li, Y. L., Kourkoutis, L. F., Klug, J. A., Li, H., Ryan, P., Wang, L. P., Bedzyk, M., Muller, D. A., Chen, L. Q., Levy, J., and Schlom, D. G., *Science,* **324**, 367, 2009.

Weber, M. J., and Schaufele, R. F., *J. Chim. Phys.* **43**, 1702, 1965.

Weber, M. J., *Phys .Rev.* **157**, 262, 1967.

Wellenius, P., Suresh, A., and Muth, J. F., *Appl. Phys. Lett.* **92**, 021111, 2008.

Wen, C. H., Chu, S. Y., Juang, Y. D., and Wen, C. K., *J. Cryst. Growth* **280**, 179, 2005a.

Wen, C. H., Chu, S. Y., and Wen, C. K., *Integr. Ferroelectr.* **69**, 267, 2005b.

Wermuth, M., Schmitz, A., and Güdel, H. U., *Phys .Rev. B* **63**, 245118, 2001.

Wiedemann, G., *Ann. Phys. Chem.* **34**, 446, 1888.

Wong, H. T., Chan, H. L. W., and Hao, J. H., *Opt. Express***,** **18**, 6123, 2010.

Wood, W., Halpert, J. E., Panzer, M. J., Bawendi, M. G., and Bulovic, V., *Nano Lett.* **9**, 2367, 2009.

Wu, S. M., Cybart, S. A., Yu, P., Rossell, M. D., Zhang, J. X., and Ramesh, R., *Nat. Mater.* **9**, 756, 2010.

Wu, X. X., Feng, W. L., Fang, W., and Zheng, W. C., *Physica Status Solid* **245**, 756, 2008.

Xu, S., Qin, Y., Xu, C., Wei, Y. G., Yang, R., and Wang, Z. L., *Nat. Nanotechnol.* **5**, 366, 2010.

Yang, J., Zhang, C. M., Peng, C., Li, C. X., Wang, L. L., Chai, R. T., and Lin, J., *Chem. Eur. J.* **15**, 4649, 2009.

Yang, Q., Guo, X., Wang, W. H., Zhang, Y., Xu, S., Lien, D. H., and Wang, Z. L., *ACS Nano* **4**, 6285, 2010.

Yang, Q., Wang, W. H., Xu, S., and Wang, Z. L., *Nano Lett.* **11**, 4012, 2011.

Yang, S. Y., Seidel, J., Byrner, S. J., Shafer, P., Yang, C. H., Rossell, M. D., Yu, P., Chu, Y. H., Scott, J. F., Ager, J. W., Martin, L. W., and Ramesh, R., *Nat. Nanotechnol.* **5**, 143, 2010.

Yang, Y. D., Wang, Z. G., Li, J. F., and Viehland, D., *J. Nanomater.* **vol. 2010**, article ID 756319, 2010. doi:10.1155/2010/756319

Yen, W. M., Shionoya, S., and Yamamoto, H., *Phosphor Handbook*, Taylor & Francis, London, 2007.

Yeung, K. M., Mak, C. L., Wong, K. H., and Pang, G. K. H., *Jpn. J. Appl. Phys.* **43**, 6292, 2004.

Yi, G., and Chow, G., *Chem. Mater.* **19**, 341, 2007.

You, Y. C., Park, N., Jung, K. H., Park, H. L., Kim, K. C., Mho, S. I., and Kim, T. W., *J. Mater. Sci. Lett.* **13**, 1682, 1994.

Zhang, C. M., Ma, P. A., Li, C. X., Li, G. G., Huang, S. S., Yang, D. M., Shang, M. M., Kang, X. J., and Lin, J., *J. Mater. Chem.* **21**, 717, 2011a.

Zhang, G., Liu, Y. L., Yuan, Q. H., Zong, C. H., Liu, J. H., and Lu, L .H, *Nanoscale* **3**, 4365, 2011b

Zhang, H., Li, Y. J., Ivanov, I. A., Qu, Y. Q., Huang, Y., and Duan, X. F., *Angew. Chem. Int. Ed.* **49**, 2865, 2010.

Zhang, H., Li, Y. J., Lin, Y. C., Huang, Y., and Duan, X. F., *Nanoscale* **3**, 963, 2011c.

Zhang, H. X., Kam. C. H., Zhou, Y., Han X. Q., and Chan, Y. C., *Appl. Phys. Lett.* **77**, 609, 2000.

Zhang, P. Z., Shen, M. R., Fang, L., Zheng, F. G., Wu, X. L., Shen, J. C., and Chen, H. T., *Appl. Phys. Lett.* **92**, 222908, 2008.

Zhang, R., Jiang B., and Cao, W. W., *Appl. Phys. Lett.* **82**, 787, 2003.

Zheng, R. K., Wang, Y., Wang, J., Wong, K. S., Chan, H. L. W., Choy, C. L., and Luo, H. S., *Phys. Rev. B* **74**, 094427, 2006.

Zheng, R. K., Wang, Y., Chan, H. L. W., Choy, C. L., and Luo, H. S., *Appl. Phys. Lett.* **90**, 152904, 2007.

Zhou, D., Cheung, K .F., Chen, Y., Lau, S. T., Zhou, Q. F., Shung, K. K., Luo, H. S., Dai, J. Y., and Chan, H. L. W., *IEEE Trans. Ultrason. Ferroelectr. Freq. Control* **58**, 477, 2011.

Zhou, J., Fei, P., Gu, Y. D., Mai, W. J., Gao, Y. F., Yang.R. S., Bao, G., and Wang, Z. L., *Nano Lett.* **8**, 3973, 2008.

Zhou, S. F., Hao, J. H., and Qiu, J. R., *J. Am. Ceram. Soc.* **94**, 2902, 2011.

Zhou, Z., Komori, T., Ayukawa, T., Yukawa, H., Morinaga, M., Koizumi, A., and Takeda, Y., *Appl. Phys. Lett.* **87**, 091109, 2005.

Zijlmans, H. J. M. A. A., Bonnet, J., Burton, J., Kardos, K., Vail, T., Niedbala, R. S., and Tanke, H. J., *Anal. Biochem.* **267**, 30, 1999.